BORON DOPED ULTRANANOCRYSTALLINE DIAMOND POWDER: ALTERNATIVE SUPPORT MATERIAL FOR PEMFCS

By

Ayten Ay

A DISSERTATION

Submitted to
Michigan State University
in partial fulfillment of the requirements
for the degree of

DOCTOR OF PHILOSOPHY

Chemistry

2011

ABSTRACT

BORON DOPED ULTRANANOCRYSTALLINE DIAMOND POWDER: ALTERNATIVE SUPPORT MATERIAL FOR PEMFCS

By

Ayten Ay

Recent studies have showed that the corrosion of carbon support in fuel cells can greatly affect the cell performance and durability. On this basis, novel corrosion resistant materials have attracted much interest as electrocatalyst support.

The challenges are to develop supports with high surface area (100m²/g), good electrical conductivity (~1S/cm), chemical and thermal stability up to 200°C, morphological and microstructural stability at high potentials (e.g., ~1 V vs. the reversible hydrogen electrode (RHE)) and not too expensive.

Ultrananocrystalline diamond (UNCD) powder is an advanced carbon material that has high surface area (200-600 m²/g), superb mechanical strength, chemical and thermal stability, and corrosion resistance. However, electrical conductivity is a technical challenge that must be overcome before electrically conducting diamond can become a viable electrocatalyst support material.

In this dissertation, we suggested the way to overcome conductivity problem for UNCD powders. The preparation of higher specific surface area (50 and 170 m²/g) and electrically conducting (1 S/cm) diamond powders prepared by coating 500 nm, 100 nm and 3-6 nm diam. particles with a layer of boron-doped nanocrystalline diamond is reported. The physical, chemical, and electrochemical properties of boron doped UNCD (B-UNCD) powder with respect to sp²-bonded carbons were studied using electrochemical methods, SEM, HRTEM, Raman

spectroscopy, and XRD. Electrical conductivity measurements and Raman spectroscopy confirmed the successful deposition of a boron-doped UNCD overlayer. All powders exhibited electrochemical responses for that were comparable to typical responses seen for high-quality, boron-doped nanocrystalline diamond thin-film electrodes.

The deposition of Pt electrocatalyst particles on the conductive diamond powder surfaces were second part of the work in this dissertation. The particle size, dispersion and electrochemical activity of Pt/B-UNCD-diamond powders were characterized. The catalytic activity of conductive diamond powder supported Pt particles towards oxygen reduction reaction (ORR) was investigated. To calculate the kinetic parameters (Tafel slope, exchange current density, mass activity and specific activity) RDE was prepared and cyclic voltammetry and linear sweep voltammetry were performed.

In the last part of the dissertation, the performance of membrane electrode assemblies (MEA) prepared by using the metal decorated B-UNCD powders were discussed. A 200 h life test in a single cell test assembly was carried out and open circuit potential and catalyst active area were monitored as a function of time. SEM images were obtained to characterize the MEAs before and after accelerated degradation test and results compared with Vulcan XC-72 powder supported MEAs. Excellent stability of the B-UNCD powder supported catalysts over the Vulcan XC-72 commercial support was observed. These results prove the potential of B-UNCD powder as a support to replace carbon black.

ACKNOWLEDGEMENT

I would like to thank my advisor Prof. Greg M. Swain for his support throughout my graduate research. Without his support, this research has not been successfully accomplished. Thank you very much Greg for being a wonderful example for me as a person and as an advisor. I also like to thank Prof. Greg Baker, Gary Blanchard and Keith Premislow for accepting to be my committee members and providing valuable comments on my research. I would also like to thank Dr. David Arnosti. I consider myself very lucky person to meet you and your family.

In addition, I would like to thank all members of Swain group, specially Matt Swope, Dr. Isao Sasaki and Dr. Doo Young Kim Many thanks go to all other students for their friendship and help. I have been fortunate to have a wonderful group of friends at Michigan State.

I would like to say thank you to my parents. I would not be where I am today without their encouragement, their love, and their support. Thank you for always being there for me.

And finally, Ahmet, your support and enthusiasm were invaluable. You helped me to start PhD and encouraged me to keep working even on weekends and at nights. I was complaining at these times but thanks so much. I truly could not have done this without you.

Ayten Ay

TABLE OF CONTENTS

List of Tables	viii
List of Figures	ix
Key to Symbols and Abbreviations	xiv
<u>CHAPTER 1</u> -RESEARCH CHALLENGES FOR POLYMER ELECTR	
MEMBRANE FUEL CELLS (PEMFCs)	1
1.1. Background.	
1.2. Proten exchange membrane Fuel cells (PEMFCs)	
1.3. Reactions in PEMFCs.	
1.3.1. Anode Reaction (Hydrogen Oxidation)	
1.3.2. Cathode Reaction (Oxygen Reduction)	
1.4. Support Materials for PEMFC catalysts	
1.5. Carbon Corrosion in PEMFCs.	
1.6. Alternative Support Materials.	
1.6.1. Carbon nanotubes (CNT)	
1.6.2. Oxides	
1.6.3. Carbon/graphite nanofibers.	
1.6.4. Ultrananocrystalline diamond (UNCD) powder	
1.7. Research Goals and Objectives.	
1.8. Dissertation Outline.	
1.9. References.	27
CHARTER A EVREDIMENTAL METHODS	22
CHAPTER 2 – EXPERIMENTAL METHODS	
2.1. Boron doped-Ultrananocrystalline Diamond (B-UNCD) Layer Overcoating	
2.2. Material Characterization.	
2.2.1. Scanning Electron Microscopy (SEM)	
2.2.2. Transmission Electron Microscopy (TEM)	
2.2.3. X-Ray Diffraction Spectroscopy (XRD)	
2.2.5. Electrical Resistance	
2.2.6. Specific surface area measurements.	
2.2.7. Electrochemical Characterization	
2.2.8. Polarization Studies	
2.2.9. Electrode Preparation and Experimental Setup.	
2.2.9.1.Film Electrodes.	
2.2.9.1.14ffff Electrodes	
2.3. Reagents 2.4. Chapter-Specific Experimental Methods	
2.4.1. Fourier Transform Infrared (FTIR) (Chapter 5)	
2.4.1. Fourier Hansform Infrared (FTR) (Chapter 5)	
2.4.2. Differential Fulsed Voltammenty (DFV) (Chapter 3)	
2.4.4. Rotating Disk electrode preparation (Chapter 6)	
2.7.7. Rotating Disk electrone preparation (Chapter o)	43

2.4.5.	Atomic absorption spectroscopy (Chapter 6)	44
	X-ray photoelectron spectroscopy (Chapter 6)	
	nbrane Electrode Assembly (MEA) preparation	
	Test Conditions for Carbon Support Stability	
	Morphological characterization	
	erences	
	<u>3</u> – THE PHYSICOCHEMISTRY AND ELECTRO	
	ES OF DIAMOND POWDERS COATED WITH BOR	
	NOCRYSTALLINE DIAMOND	
	duction	
	nanism of Ultrananocrystalline Diamond Growth	
	lts	
	Diamond powder morphology and microstructure	
	Specific surface area and electrical conductivity measurements	
	Background cyclic voltammetric current density-potential curves	
	Cyclic voltammetric response for different redox systems	
3.3.5.	Morphological and microstructural stability testing	71
	ussion	
3.5. Conc	elusion	79
3.6. Refei	rences	81
ULTRANAN	FUNCTIONAL GROUPS FORMED ON BOR NOCRISTILLINE DIAMOND (UNCD) COATED POWDERS	86
	duction	
	lts	
	Morphology and Microstructure	
	Electrical conductivity measurements.	
	Background cyclic voltammetric current density–potential curves	
	Differential Pulse Voltammetric analysis.	
	Fourier Transform Infrared Spectroscopy (FTIR) Characterization	
	ussion	
	elusion	
4.5. Refei	rences	113
	<u>5</u> – THE CORROSION RESISTANCE AND ELECTROACTIV	
	HIGH SURFACE AREA CONDUCTIVE DIAMOND POV	
	EDUCTION	
	luction	
5.2 Result	ts and Discussion.	
5.2.1	Physical and chemical characterization.	
5.2.2	Effect of surface chemistry on Pt deposition	
5.2.3	Electrochemical Characterization.	
5.2.4	Oxygen Reduction Reaction	120
	Corrosion Test	130

5.3 Discussion.	142
5.4 Conclusions.	144
5.5 References.	146
<u>CHAPTER 6</u> – ELECTROCHEMICAL PERFORMANCE AND DURABILI UNCD-DIAMOND POWDERS AN ELECTROCATALYST SUPPORT MATE	
PEMFCs	150
6.1. Introduction	150
6.2. Results	153
6.2.1. Optimum Nafion content in PEMFC electrodes	153
6.2.2. Durability	
6.2.3. Morphology of MEA before and after polarization test	161
6.3. Discussion	161
6.4. Conclusion	166
6.5. References	167
<u>CHAPTER 7</u> – CONCLUSION AND FUTURE RESEARCH DIRECTIONS	171
7.1. Conclusion	
7.2. Future research directions	173
7.2.1. Preparation of B-UNCD-Diamond Powder	173
7.2.2. Pt/B-UNCD-diamond Powder for Oxygen Reduction Reaction	174
7.2.3. B-UNCD-Diamond Support for PEMFC	175
7.2.4. Application of B-UNCD-Diamond Powder in Energy Devices	176
7.2.4.1. Hydrogen Storage	
7.2.4.2. Lithium Batteries	177
7.2.4.3 Supercapacitors	177

LIST OF TABLES

Table 1.1.	Approximate cost for some carbon materials currently used as or being considered for use as an electrocatalyst support	20
Table 2.1.	Accelerated degradation testing protocols for fuel cell materials	48
Table 3.1.	Electrical conductivity and specific surface area of the uncoated, B-UNCD coated diamond, and sp ² -bonded carbon powders before and after acid washing.	61
Table 3.2.	Cyclic voltammetric peak potential separation (ΔE_p) and peak current ratio ($i_p^{\rm forward}/i_p^{\rm reverse}$) for various redox analysis at 500 nm and 100 nm doped diamond powder, and glassy carbon powder electrodes.	61
Table 4.1.	Summary of main IR frequencies of Glassy Carbon and B-UNCD coated Glassy carbon	100
Table 4.2.	Summary of main IR frequencies of B-UNCD coated diamond powder	101
Table 5.1.	Comparison of Pt nanoparticles properties on different support materials.	125
Table 5.2.	Comparison of the kinetics parameters for ORR at the Pt/B-UNCD diamond with the literature data reported for single crystal, polycrystalline, and carbon supported Pt at room temperature	132
Table 5.3.	Comparison of Pt nanoparticles properties on different support materials before and after anodic polarization at 1.4V vs. SHE	134

LIST OF FIGURES

Figure 1.1A.	Diagram of a PEMFC membrane electrode assembly (MEA) 3		
Figure 1.1B.	An expanded view of the "triple region" in MEA		
Figure 1.2.	An exploded view of PEMFC components		
Figure 1.3.	Microstructures of (A) graphite, and (B) carbon black		
Figure 1.4.	SEM of fresh (a) and tested MEAs after 80 cycles (b); magnification 1500×		
Figure 1.5.	TEM image of Pt deposited carbon black particles (A) before and (B) after polarization at 853 mV vs. SHE	11	
Figure 1.6.	TEM images of the Pt filled nitrogen containing carbon nanotubes	14	
Figure 1.7.	Typical high-resolution SEM image of detonation nanodiamond powder	16	
Figure 2.1.	Illustration of the core-shell concept for coating diamond powders with a layer of boron-doped ultrananocrystalline diamond	34	
Figure 2.2.	Schematic diagram of the apparatus used to measure i-V curves for the powder samples		
Figure 2.3.	Diagram of the pipette electrode used for testing the electrochemical properties of the conducting powder	38	
Figure 2.4.	Potential wave form for differential pulse voltammetry	42	
Figure 2.5A.	Ink preparation from platinized diamond powder, Nafion binder and isopropyl alcohol. (B) MEA preparation procedure from ink drop casting and hot press.	46	
Figure 2.5B.	MEA preparation procedure from ink drop casting and hot	46	
Figure 3.1.	1		
Figure 3.2.	SEM images of 500 and 100 nm diam. diamond powder (A) and (C) before, and (B) and (D) after deposition of a boron-doped UNCD for 2 h	59	

Figure 3.3.	Visible Raman spectra of 100 nm diam diamond powder before and after coating with a layer of boron-doped nanocrystalline diamond	
Figure 3.4.	Background cyclic voltammetric i-E curves for acid-washed 500 and 100 nm diam. B-UNCD-coated powders recorded using the pipette electrode.	
Figure 3.5.	Cyclic voltammetric i-E curves for 1 mM Fe(CN) $_6^{3-/4-}$ in 1 M KCl at (A) 500 nm and (C) 100 nm diam. B-UNCD-coated diamond powder electrodes. Cyclic voltammetric i-E curves for 1 mM IrCl $_6^{2-/3-}$ in 1 M KCl at (B) 500 nm diam. B-UNCD-coated diamond powder and (D) 100 nm B-UNCD-coated diamond powder electrodes. The curves were recorded using the pipette electrode, and the currents are normalized to the geometric area of the electrode, $0.002 \mathrm{cm}^2$.	68
Figure 3.5	Cyclic voltammetric i-E curves at GC powder electrodes for (E) for	
Continue.	1 mM Fe(CN) $_6^{3-/4-}$ in 1 M KCl and (F) for 1 mM IrCl $_6^{2-/3-}$ in 1 M KCl. Cyclic voltammetric i-E curves for 1 mM Fe $_6^{3+/2+}$ in 1 M	
	HClO ₄ at (G) 500 nm diam. B-UNCD-coated diamond powder and (H) GC powder electrodes. The curves were recorded using the pipette electrode, and the currents are normalized to the geometric area of the electrode, 0.002 cm ²	69
Figure 3.6.	Continuous amperometric i-t curves for 500 and 100 nm diam. B-UNCD-coated diamond powders recorded at 1.4 V vs. Ag/AgCl in 0.5 M $_{2}SO_{4}$ for 1 h at 80 $^{\circ}C$. A comparison curve for GC powder is also shown.	74
Figure 3.7.	Cyclic voltammograms for 500 nm, 100 nm B-UNCD-caoted diamond powder and glassy carbon before and after anodic polarization in 0.5M H ₂ SO ₄ for 1 h.	75
Figure 3.8.	SEM images of GC powder before and after 1-h polarization at 1.4 V vs. Ag/AgCl in 0.5 M H ₂ SO ₄ for at 80 °C. Images are also shown of 500 nm B-UNCD-coated diamond powder before and after the same anodic polarization.	80
Figure 4.1.	SEM and TEM images of GC, B-UNCD-coated glassy carbon, acid washed 3-6 nm Diamond and B-UNCD-diamond powder	89
Figure 4.2.	Raman spectra of acid washed 3-6 nm diamond, B-UNCD-diamond, B-UNCD-GC and GC powder	90

Figure 4.3.	Cyclic Voltammetric i-E curves for GC, B-UNCD-GC and B-UNCD-diamond powder in 0.5 M H ₂ SO ₄ at 50 mV/sec before and after anodic polarization at 1.4 V for 1h at room temperature	94
Figure 4.4.	Differential Pulse voltammetric i-E curves for GC, B-UNCD-GC and B-UNCD-diamond in 0.5M H ₂ SO ₄	96
Figure 4.5.	Differential Pulse voltammetric i-E curves for Microcrystalline, Nanocrystalline and Ultra-nanocrystalline diamond thin film electrodes in $0.5M\ H_2SO_4$ before and after polarization at $1.4V\ vs.\ Ag/AgCl$ for $1\ h.$	97
Figure 4.6.	Electrochemically active surface oxide species on GC, B-UNCD-GC and B-UNCD-diamond powder before and after anodic treatment at different potentials in 0.5 M H ₂ SO ₄ for 1 h at room temperature.	99
Figure 4.7.	FT-IR spectra of GC, B-UNCD-GC and B-UNCD-diamond powder before and after anodic polarization at 1.4 V vs. Ag/AgCl for 1 h in 0.5 M H ₂ SO ₄	102
Figure 5.1.	Schematic representation of the effect of carbon corrosion on agglomeration and loss of Pt particles and ohmic resistance in the membrane electrode assembly (MEA) during PEMFC operation	
Figure 5.2A.	Bright field TEM images of Pt-coated 100 nm diam. B-UNCD-diamond powder.	141
Figure 5.2B.	Bright field HRTEM images of Pt-coated 100 nm diam. B-UNCD-diamond powder	121
Figure 5.2C.	A histogram of the Pt particle size distribution on the 100 nm diamond powder. The data set includes measurements of 100 Pt particles.	121
Figure 5.2D.	HRTEM image of a Pt nanoparticle attached to the 100 nm diamond powder	121
Figure 5.3.	TEM and HRTEM images of Pt coated 3-6 nm diam. Boron-doped ultrananocrystalline diamond powder	123
Figure 5.4.	XRD pattern for 20 wt. % Pt-loaded B-UNCD-diamond powder. The diamond particles coated were 3-6 nm diam	123

Figure 5.5A.	A representative bright-field HRTEM image of H-terminated Pt/B-UNCD-diamond powder	
Figure 5.5B.	A dark field STEM image of H-terminated Pt/B-UNCD-diamond powder	126
Figure 5.5C.	EELS spectrum of H-terminated 100 nm Pt/B-UNCD-Diamond powder. The spectrum from is overlaid with a EELS spectrum from a mixed phase sp ² /100 nm diam. diamond powder	10.5
	a mixed phase sp / 100 nm diam. diamond powder	126
Figure 5.6.	Cyclic voltammetric <i>i-E</i> curves in 0.1 M HClO ₄ for a Pt/B-UNCD-diamond powder	128
Figure 5.7A.	Oxygen reduction current densities on 20% Pt/B-UNCD-diamond powder (3-6nm) supported on a glassy-carbon disk electrode	133
Figure 5.7B.	Koutechy-Levich plots for the oxygen reduction reaction. Data taken from the LSV results shown in (A). Rotation rate of 500-3000 rpm	
	were used and the measurements made in 0.1 M HClO ₄ at room temperature	133
Figure 5.8.	Tafel plots for the oxygen reduction reaction in 0.1 M HClO ₄ for Pt/Vulcan and 3-6 nm Pt/B-UNCD-diamond powder. Data taken from the polarization curves at a 500 rpm rotation rate	134
Figure 5.9.	Cyclic voltammetric $i\text{-}E$ curves for Pt/B-UNCD-diamond powder (100 nm) and 20 wt. % Pt/Vulcan in 0.5 M H ₂ SO ₄ before (solid line) and after (dashed line) anodic polarization at 1.4 V vs. RHE at 80 $^{\circ}$ C	137
Figure 5.10.	Chronoamperometric curve for 20 wt % Pt/Vulcan XC-72, Vulcan XC-72, 20 wt % Pt/B-UNCD-diamond, and B-UNCD, measured at 1.4V vs. RHE 80 °C in N ₂ purged 0.5M H ₂ SO ₄	138
Figure 5.11.	Oxygen reduction current densities on 20 wt. % Pt/B-UNCD-diamond powder (100 nm) and 20 wt. % Pt/Vulcan XC-72 before and after anodic polarization at 1.4 V vs. RHE	141
Figure 5.12.	TEM micrographs of 100 nm 20 wt % Pt/B-UNCD-diamond after anodic polarization for 1 h at 1.4 V in 0.5 M H ₂ SO ₄ at 80 $^{\rm o}$ C	141

Figure 6.1A.	Cyclic voltammetric <i>i-E</i> curves for Pt/B-UNCD-diamond MEAs at	
	room temperature with 0.5 mg Pt/cm ² in the catalyst layer. Scan rate=5 mV/sec	155
Figure 6.1B.	Electrochemically active surface area (ECSA) of Pt/B-UNCD-diamond MEAs versus various Nafion content in the catalyst layer. The anode served as both the counter and reference electrode in the cyclic voltammetry measurements. The anode is essentially at the potential of the RHE.	155
Figure 6.2.	Cyclic voltammetric <i>i-E</i> curves for (A) Pt/B-UNCD-diamond and (B) Pt/Vulcan MEAs before and after a 200-h accelerated degradation test at room temperature. Scan rate 5 mV/sec. Scale bars show 1 mA/cm ² for each voltammogram	156
	snow i in veni Toi cach voltaminogram	130
Figure 6.3.	Comparison of the ECSA for Pt/Vulcan and Pt/B-UNCD-diamond MEAs during a 200-h degradation test at room temperature	157
Figure 6.4.	Open circuit voltage (OCV) of the cell as a function of time during the MEA accelerated degradation test. The cell was operated at room temperature using an H_2/O_2 flow rates of $2/9$	158
Figure 6.5.	Current-voltage plots for Pt/B-UNCD-diamond and Pt/Vulcan MEAs before and after a 200-h degradation test. The current was normalized to the geometric area of the electrode	158
Figure 6.6.	SEM cross-section images of Pt/B-UNCD-diamond and Pt/Vulcan MEAs before and after a 200-h degradation test. (A) B-UNCD-diamond before, (B) B-UNCD-diamond after, (C) Vulcan before, (D) Vulcan after. (E) Vulcan-before (electrode surface), (F) Vulcan-after (larger area)	160
Figure 6.7.	SEM images of graphite nanoplatelets formed on some powder surfaces during B-UNCD growth. In addition to B-UNCD, this carbon forms during the overcoating process	165

KEY TO SYMBOLS AND ABBREVIATIONS

δ Bending mode in IR spectra

 δ_{as} Asymetric vibration mode in IR spectra

 $\Delta E_{\rm p}$ Peak potential separation

 δ_s Symetric vibration mode in IR spectra

v Vibration mode in IR Spectra

v_{as} Asymetric vibration mode in IR spectra

 $v_{\rm S}$ Symetric vibration mode in IR spectra

ρ Specific resistivity

AAS Atomic Absorption Spectroscopy

Ads Adsorption

Ag/AgCl Silver/Silver chloride reference electrode

b contact radius

BDD Boron-Doped Diamond

BET Brunauer–Emmett–Teller

B-UNCD Boron-doped ultrananocrystalline diamond

CCM Catalyst-coated membrane

CNF Carbon/graphite nanofibers

CNT Carbon nanotubes

CV Cyclic voltammetry

DOE Department of Energy

DPV Differential Pulse Voltammetry

ECSA Electrochemically Active Surface Area

EDS Energy-dispersive X-ray spectroscopy

EELS Electron energy loss spectroscopy

E₀ Standard potential

FeSO₄ Ferric sulfate

FTIR Fourier Transform Infrared spectroscopy.

FWHM Full width at half maximum

GC Glassy carbon

GDL Gas diffusion layer
GNF Graphite nanofiber

H₂O₂ Hydrogen Peroxide

H₂SO₄ Sulfuric Acid

HClO₄ Perchloric acid

HRTEM High-resolution transmission electron microscopy

I_m Mass activity

I₀ Exchange current density

IPA Isopropyl alcohol

i_s Specific activity

IUPAC International Union of Pure and Applied Chemistry

K₂IrCl₆ Potassium hexachloroiridate

K₄Fe(CN)₆ Potassium ferrocyanide

KCl Potassium chloride

LSV Linear sweep voltammetry

MEA Membrane electrode assembly

MWCNT Multiwall carbon nanotubes

NaOH Sodium hydroxide

OCP Open Circuit Potential

PACVD Plasma-assisted chemical vapor deposition

PEMFC Polymer electrolyte membrane fuel cells

PTFE Polytetrafluoroethylene

R_c Contact resistance

RDE Rotating disk electrodes

RHE Reference Hydrogen Electrode

SCE Standard Calomel Electrode

SEM Scanning electron microscopy
SHE Standard hydrogen electrode
SWCNT Single-wall carbon nanotubes

TEM Transmission electron microscopy

UNCD Ultrananocrystalline diamond

XPS X-ray photoelectron spectroscopy

XRD X-ray diffraction

Chapter 1

Introduction

1.1 Background

Polymer electrolyte membrane fuel cells (PEMFCs) symbolize an environmentally friendly technology and are attracting considerable interest for producing electricity by direct electrochemical conversion of hydrogen and oxygen into water.

Fuel cell developers have produced PEMFCs for many years, however, there are three major challenges have left to widespread fuel cell use: cost, performance and lifetime. Studies of automotive PEMFC performance degradation have shown that voltage losses of >50 μ V/h occur during operation, while target losses of less than 10 μ V/h are needed for a 5,000 h operating lifetime [1, 2]. Four major degradation modes are observed in PEMFCs which are 1) The membrane (Nafion) degradation, 2) electrocatalyst dissolution and migration, 3) degradation of stack materials and 4) corrosion of support material (carbon).

The electrodes consist of nanometer-sized electrocatalyst particles, such as Pt, dispersed over a high-surface-area (~100 m²/g), sp²-bonded carbon powder support. Carbon black (Vulcan XC- 72) and activated carbon are mainly used as catalysts support in PEMFCs. These materials all contain sp²-bonded carbon and high ratio of edge plan density. In the presence of oxygen, carbon support oxidation occurs which leads to corrosion of the support material.

The carbon support and the interaction of the electrocatalyst with it have received the least attention from researchers in terms of material development, even though it is recently recognized that carbon support degradation can be a significant contributor to performance loss [3].

Electrochemical corrosion of carbon materials as catalyst supports of PEMFCs will cause electrical isolation of the catalyst particles as they are separated from the support or lead to aggregation of catalyst particles, both of which result in a decrease in the electrochemical active surface area of the catalyst and an increase in the hydrophilicity of the surface, which can, in turn, result in a decrease in gas permeability as the pores become more likely to be filled with liquid water films that can hinder gas transport [4-6].

On this basis, an important issue of the research in the field of the fuel cells is addressed on the development of new carbon and non-carbon supports material, which has high corrosion resistance.

The research presented in this dissertation was conducted to address development of high surface area conductive ultrananocrystalline diamond (UNCD) powder as an alternative electrocatalyst support material. Its synthesis, characterization, metal decoration and application in a PEMFC were described. This chapter presents background information and provides a context for the current work, including a description of PEMFC operating principles and electrode materials, specific criteria for electrocatalyst supports in PEMFCs, a description of carbon corrosion in PEMFC, and other alternative support materials. The details of a proposed dimensionally stable UNCD electrocatalyst support, including material properties, preliminary research, and other approaches for conductive diamond powder preparation are then presented. Next, the specific research questions addressed in each chapter are given, followed by an outline of the dissertation.

1.2 Polymer Electrolyte Membrane Fuel Cell (PEMFC)

A PEMFC is an electrochemical device that combines hydrogen and oxygen to produce electricity, with water and heat as the reaction products [7]. Since the conversion of the fuel to

electrical energy takes place via an electrochemical process, not a combustion one, it is a clean, quiet and highly efficient process.

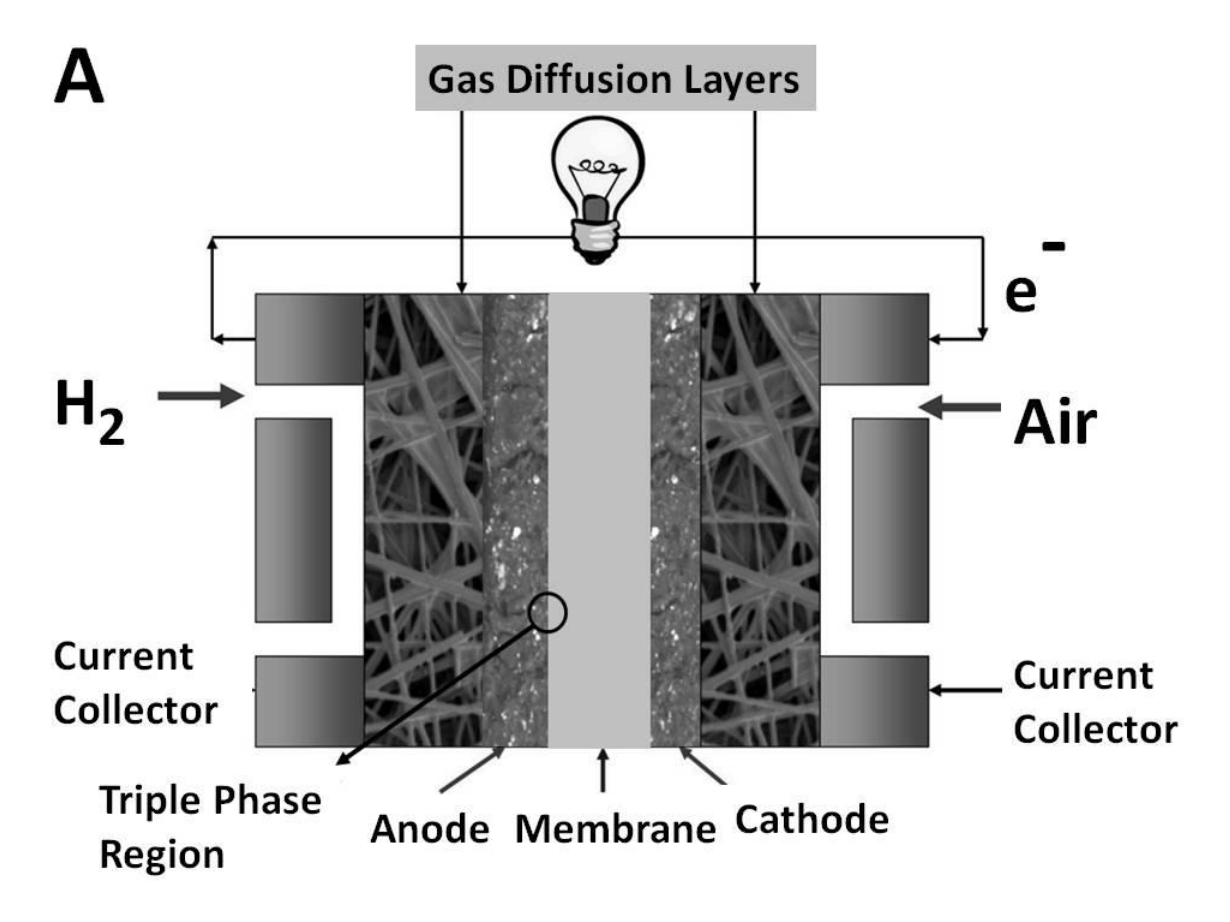


Figure 1.1A Diagram of a membrane electrode assembly (MEA) for a PEMFC.

The typical structure of a membrane electrode assembly (MEA) and a single cell in a fuel cell stack are shown in Figures 1.1 and 1.2 [8]. The MEA, the key component of the fuel cell, is positioned between a pair of current collectors or flow field plates. It consists of an anode and cathode separated by proton exchange membrane (PEM). Nafion (~ 100 µm thick) is a typical commercially employed. The electrodes consist of nanometer-sized electrocatalyst particles, such as Pt, dispersed over a high-surface-area (~100 m²/g), sp²-bonded carbon powder support. Finely dispersed electrocatalyst particles on a stable and conductive support increase the number

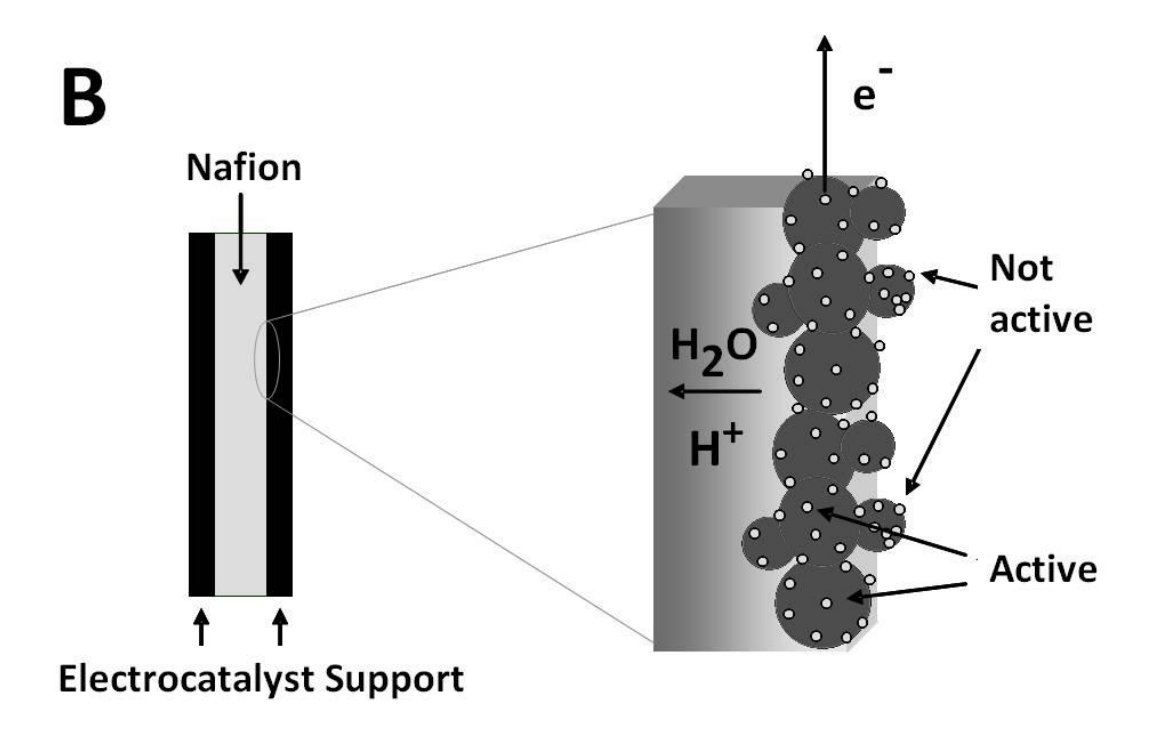


Figure 1.1B An expended view of the triple phase interface.

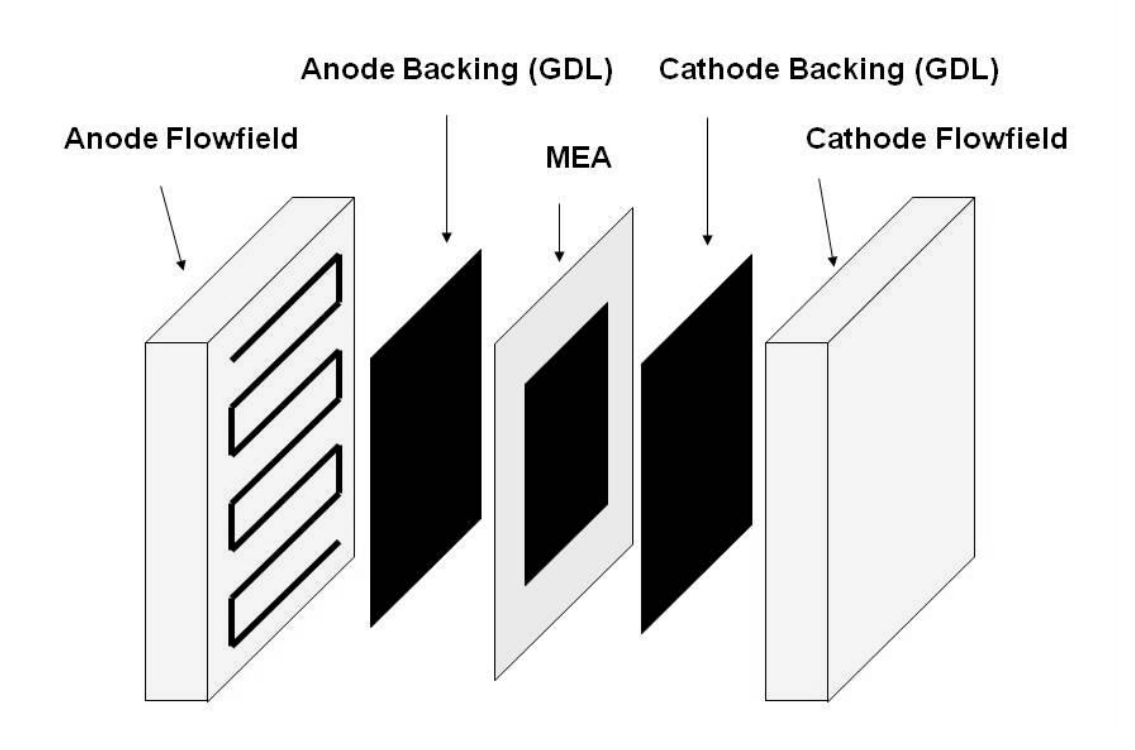


Figure 1.2 An expended view of a single PEMFC (modified from reference [8]).

of electrocatalytically-active sites available for the fuel cell reactions. This reduces the loading requirements (~ 0.1 mg/cm²) for expensive metal catalysts [9, 10]. High-surface-area graphitic carbons offer good chemical stability and mechanical strength as electrocatalyst supports material. However, graphitization improves the stability and corrosion resistance but decreases the specific surface area. It also reduces the number of active sites for electrocatalyst attachment. For this reason, high-surface-area carbon blacks, such as Vulcan XC-72, are typically used as the electrocatalyst support.

Protons and electrons are generated by hydrogen oxidation at the anode and oxygen reduction at the cathode respectively. The protons diffuse from the anode to cathode trough the polymer membrane where they react to form water at the cathode, Both electrodes consist of carbon-supported, Pt-based electrocatalysts bonded with Nafion ionomer and/or polytetrafluoroethylene (PTFE) on a gas diffusion layer (GDL). The GDL has to be highly porous to ensure easy transit of the gases to the triple phase interface where the carbon-supported Pt catalyst is in contact with ionomer. The triple phase region is the important region where the electrochemical reactions occur. Only

those electrocatalyst particles that are in direct contact with the support material and with the polymer membrane will be active for the hydrogen oxidation or the oxygen reduction reactions at the anode and cathode, respectively.

1.3 Reactions in PEMFCs

1.3.1 Anode Reaction (Hydrogen Oxidation)

In the presence of Pt-based catalysts hydrogen chemisorbs on the catalyst surface dissociating to two hydrogen atoms as follows:

$$2Pt_{(s)} + H_2 \rightarrow Pt-H_{ads} + Pt-H_{ads}$$
 [1.1]

$$Pt-H_{ads} \rightarrow Pt_{(s)} + H^{+} + e^{-}$$
 [1.2]

The net reaction is:

$$H_2 \to 2H^+ + 2e^ E^0 = 0.000V$$
 [1.3]

where E^{O} is the standard reduction potential. This reaction is very fast with nearly no activation energy required when Pt is used as a catalyst.

1.3.2 Cathode Reaction (Oxygen Reduction)

The oxygen reduction reaction at the cathode proceeds either a 4-electron or 2-electron pathway, as shown in the following equations [11].

1) Direct four-electron reduction in an acidic electrolyte

$$Pt-O_2 + 4H^+ + 4e^- \rightarrow 2H_2O$$
 $E^0 = 1.229V$ [1.4]

2) Indirect two-electron reduction in an acid electrolyte

$$O_2 + 2H^+ + 2e^- \rightarrow H_2O_2$$
 $E^0 = 0.695V$ [1.5]

followed by either

$$HOO^{-} + 3H^{+} + 2e^{-} \rightarrow 2H_{2}O$$
 [1.6]

or

$$2HOOH \rightarrow 2H_2O + O_2 \tag{1.7}$$

The 4-electron pathway is preferred due to its high charge efficiency and no involvement of peroxide species, which can oxidatively damage the membrane.

The thermodynamic cell voltage of a PEMFC is 1.23 V. However, the observed experimental potential is rather low due to sluggish kinetics of the cathodic reactions.

The slow kinetics and expensive noble-metal-based catalysts that are used are driving forces for finding ways to improve the catalytic activity. A high level of activity can be achieved by increasing temperature and increasing the reactive surface area by using finely dispersed catalyst, i.e., catalyst with a high specific surface area supported on a high surface-area, electrically conducting material. The temperatures that can be used for for PEMFCs are somewhat limited due to the decreased conductivity that results when Nafion gets dehydrated. In other words, proton conductivity in the Nafion membrane depends on the hydration of the membrane.

1.4 Support Materials for PEMFC Catalysts

The activity of a catalyst (Pt or Pt alloy) increases as the surface area of the catalyst increases. Catalyst particles should be reduced to nanometer size in order to increase the active surface area. For this reason, catalysts are often supported on a high surface area (> 100 m²/g) support material. In addition to a high surface area, an electrocatalyst support must also have sufficient electrical conductivity (>0.5S/cm) so that the support can act as a conduct for electron flow. Moreover, chemical stability in aqueous environments, thermal stability up to 200°C, and morphological and microstructural stability at high potentials (e.g. >1 V vs. the reversible hydrogen electrode (RHE)) and current densities are essential [12].

The stability of the catalyst support in the fuel cell environment is critical for high performance and long life-time. Change in the morphology of the catalyst layer from the initial state will result in a loss of electrocatalyst activity, increased ohmic resistance, and reduced operational efficiency [13-16]. Catalyst supports typically must have excellent stability for 40,000–60,000 h for stationary applications [17].

There are a number of viable support metarials including various carbon materials such as graphite, carbon black and activated carbon. These materials all contain sp²-bonded carbon, but differ significantly from one another in terms of the particle size, porosity, and microstructure. The graphite structure (Figure 1.3) consists of layers of carbon atoms arranged in fused hexagonal rings with an interlayer spacing of 3.354 Å. The parameters of importance are the coherence lengths of the graphite crystallites along a-axis (L_a) parallel and c-axis (L_c) perpendicular to the layer planes. Carbon blacks are considered amorphous carbons consisting of randomly oriented small graphitic crystallites with values for L_a and L_c in the range of 15 to 25 Å, respectively. By controlling the manufacturing conditions, carbon blacks can be produced with particle sizes varying from less than 50 Å to greater than 3000 Å, leading to a surface areas ranging from 1000 down to 10 m²/g [6].

During the last years, new carbon materials, such as fullerenes, carbon nanotubes, nanohorns and nanocoils have been tested as supports. The goal is to improve the

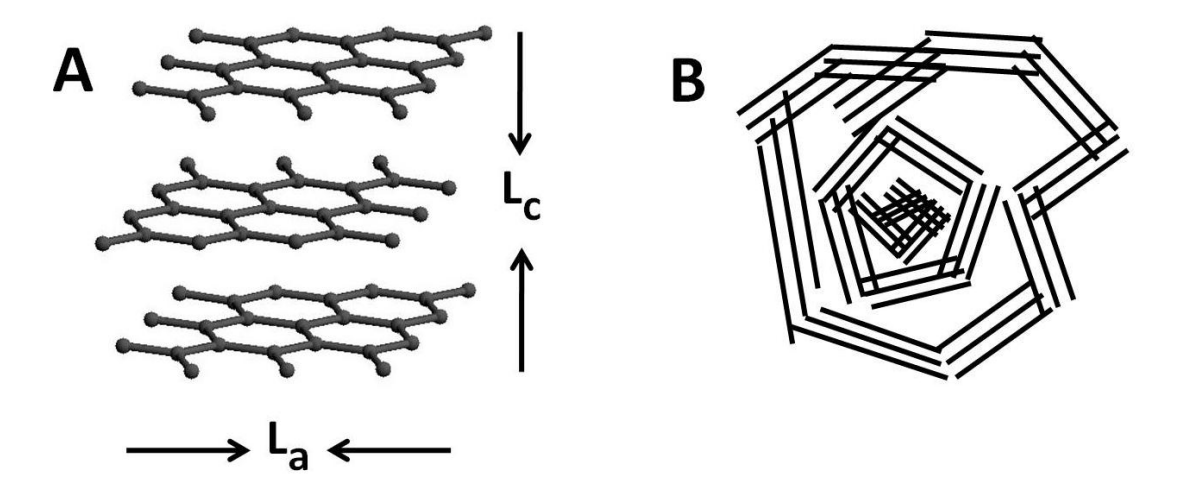


Figure 1.3 Microstructures of (A) graphite, and (B) carbon black. (Adapted from [7])

electrochemical activity and stability of the catalysts. Compared to carbon blacks, these new carbon materials are different in terms of their electronic properties, surface chemistry and morphology. The application of activated carbons, carbon blacks, graphites and graphitized materials as supports have been reviewed by Auer et al. [18]. Antolini [19]. The interested reader is referred to these three reviews.

1.5 Carbon Corrosion in PEMFCs

In the past few years, several articles have been devoted to the study of carbon oxidative corrosion in PEMFCs [35, 36]. Roen et al.[20] detected CO₂ in the cathode exhaust gas during potential cycling. Mathias et al.[21] reported the dependence of carbon corrosion current on the potential, material, temperature, and time.

Corrosion of carbon occurs by three pathways; 1) oxidation of carbon during normal operation, 2) local fuel starvation, and 3) fuel/air boundary (partial coverage of hydrogen). In the first, the carbon corrosion reaction occurs according to the following [37]:

$$C + 2H_2O \rightarrow CO_2 + 4H^+ + 4e^-$$
 $E^{\circ} = 0.207 \text{ V}$ (1.8)

At typical fuel cell operation voltage (0.6-1.0 V), this reaction is thermodynamically possible at the cathode. However, the reaction kinetics are slow because of the lower temperatures of PEM fuel cells. Nevertheless, even if the reaction happens slowly, it can affect the long-term durability.

The second pathway, carbon corrosion PEMFC occurs due to fuel starvation. Fuel cells arranged in a stack configuration can experience different flows of hydrogen and oxygen, but they will be forced to carry the same current as their neighboring cells, as they are connected in series. Due to hydrogen starvation negative cell voltages have been noted, as the anode is elevated to positive potentials and the carbon is consumed instead of the absent hydrogen [22,

23]. Fuel starvation in fuel cells was proposed in a paper by Reiser et al. [24] as a 'local starvation'. It was suggested that transient conditions can cause local potentials on the cathode significantly higher than 1 V and, thereby, cause corrosion of the carbon supports which results in permanent loss of electrochemically active area. The mechanism suggests that in the regions of the cell where hydrogen is present on the anode, the fuel cell behaves normally. In the regions of the cell where there is no hydrogen present, there is no proton or electron source at lower potentials, so the electrodes must shift to significantly higher potentials to maintain the potential difference imposed by the active part of the cell while still conserving current. Thus, a reverse current is established, and current is driven from the positive electrode to the negative electrode in the fuel-starved region. The only reactions that can sustain this current in the fuel-starved region are oxygen evolution and carbon corrosion on the positive electrode, and oxygen reduction from crossover on the negative electrode.

In the third pathway, carbon corrosion occurs due to air/hydrogen boundary at anode in starting and stopping the fuel cell. During start up and shut down unequal distribution of the hydrogen and oxygen must exist, at least for a short time. Under conditions of a prolonged shutdown, hydrogen crossover from the anode to the cathode will eventually empty out the anode chamber and result in an air-filled flow channel. In this case, the starting flow of fuel will induce a transient condition in which fuel exists at the inlet but the exit is still fuel-starved. It has been modeled and reveals that an unprotected start can induce local potentials on the cathode in excess of 1.8 V relative to a hydrogen reference electrode [25]. At this high potential the carbon catalyst-support in the cathode was severely corroded. An example of this corrosion was reported by Elter [26] is shown in Figure 1.4A and 1.4B. Scanning electron spectroscopy was used to measure the thickness of the catalyst layers, and the results are compared to the fresh MEA

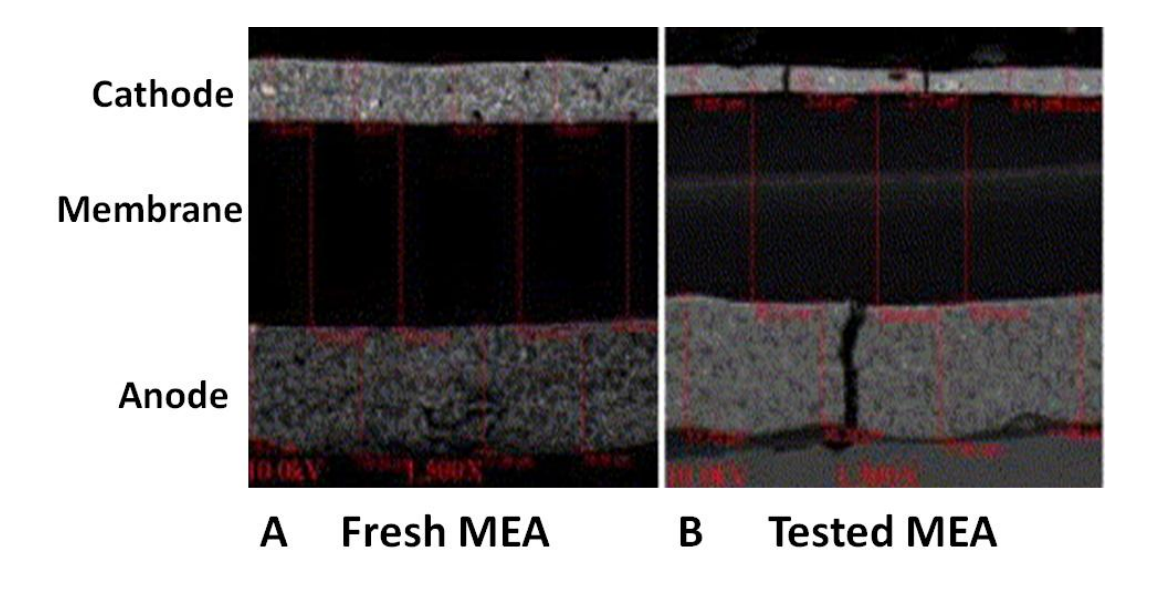


Figure 1.4 SEM of fresh (a) and tested MEAs after 80 cycles (b); magnification 1500× [4].

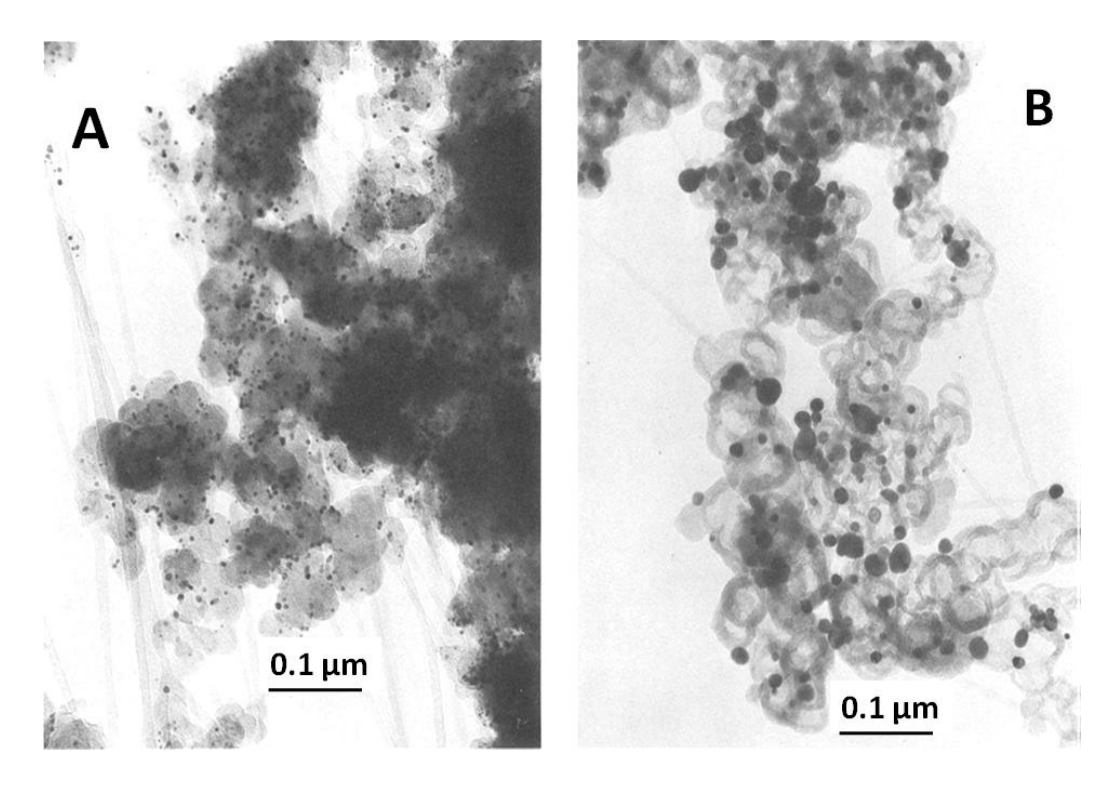


Figure 1.5 TEM image of Pt deposited carbon black particles (A) before and (B) after polarization at 853 mV vs. SHE [18]

shown in Figure 1.4A, the cathode catalyst layer thickness was reduced to about 1/3 of its original value after exposing 80 corrosion cycles, while the anode thickness did not show much change (Fig. 1.4B).

As carbon corrodes, changes in catalyst layer morphology occur. Changes in the shapes of carbon black particles have been observed by TEM shown in Figure 1.5A and 1.5B [24]. After an operation at 853 mV, the cores of primary particles of carbon black, which are less crystallized than the outer shells, corroded preferentially and became hollow. This phenomenon is important but may not be common for PEMFC case, because the electrolyte might not penetrate into the microstructure as thoroughly in PEM as it does in a liquid-electrolyte cell. It is therefore possible that the inner region of the carbon particles does not corrode in PEMFCs. As the support material corrodes, the Pt particles detach from the surface and agglomeration occurs. This leads to an increase in Pt particle size and decrease in active Pt surface area.

The degree of corrosion has been evaluated by measuring the oxidation current, [27,28,31-34,36] weight loss, [31, 32] and CO₂ generation. [27, 28] Changes of the shape of cyclic voltammograms measured in aqueous acid solution have also used to measure the changes of the surface functional groups [29, 30, 35]. These studies show that conventional carbon supports for Pt are unlikely to meet automotive durability targets and alternative support materials are required.

1.6 Alternative Support Materials

An extensive number of works have been generated on the development of carbon supports, ranging from the traditional blacks to various forms, treatments, surface modifications, and preparation protocols.

In this section, novel alternatives to carbon supports within the context of the durability issue are reviewed.

1.6.1 Carbon nanotubes (CNT)

The tubular structure of carbon nanotubes makes them unique among carbons. They may be an alternate support material due to the high surface area, excellent electronic conductivity, and high chemical stability. Conventional carbon nanotubes are made of seamless cylinders of hexagonal carbon networks and are synthesized as single-wall (SWCNT) or multiwall nanotubes (MWCNT). Typically, surface areas of SWCNT range from 400 to 900 m^2/g , whereas, for MWCNT, values range from 200 to 400 m^2/g [38–45].

The orientation of the graphene sheets and pretreatments can affect the surface chemistry and can promote the interaction with catalysts [46]. Without surface modification, most of CNTs lack sufficient binding sites for anchoring precursor metal ions or metal nanoparticles. This leads to poor dispersion and aggregation of metal nanoparticles, especially under high loading conditions. Figure 1.6 shows the TEM image of N-CNT supported Pt nanoparticles. TEM pictures reveal that the Pt particles have been homogeneously dispersed on the nanotubes and particle sizes were found to be around 3 nm.

When CNTs used as the anode and/or cathode in low-temperature fuel cells, Pt and Pt-M catalysts supported on the nanotubes exhibit higher catalytic activity than the same catalysts supported on carbon blacks [47-57]. The higher activity of CNT supported metal with respect to CB supported metal was ascribed to different factors, such as the crystalline nature of CNTs [58, 59], graphitic layer interspaces and architecture of the carbon nanotubes.

While a performance advantage is claimed for a nanotube supported catalyst compared to another support, nanotube durability and stability are rarely mentioned. However, Wang et al.

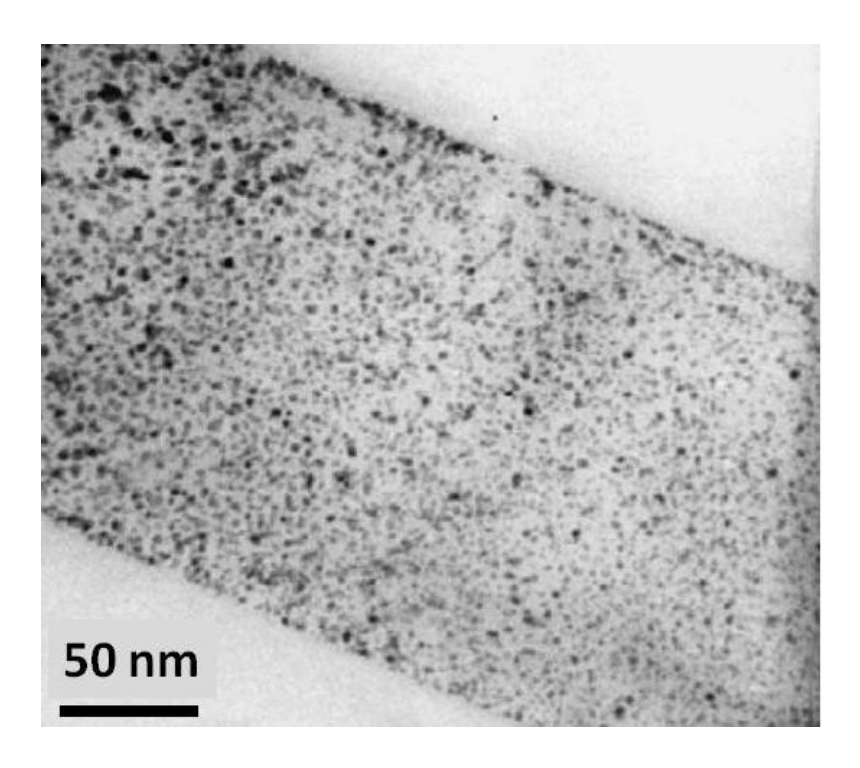


Figure 1.6 TEM images of the Pt filled nitrogen containing carbon nanotubes [33].

show that MWNTs experience less oxidation at 0.9 V and less Pt surface area loss than XC-72 in durability testing [60].

The research may not be sufficient to provide the information for commercialization CNTs as a catalyst support material in fuel cells, especially for the high cost of such materials. Further tests, particularly in a single fuel cell, have to be performed to confirm the good long-term performance of the CNTs as a support for fuel cell catalysts.

1.6.2 Oxides

Various metal oxides have low electronic conductivities at low temperatures due to mixed valence stoichiometries that introduce charge carriers into the structure. A mixed valence TiOx material has been used as a support for Pt; however, inferior performance was observed compared to graphite. The inferor performance was due to weak support interactions, [61] Ioroi

et al. compared Pt-loaded Ti_4O_7 supports with XC-72 carbon in fuel cell testing [62]. They found that the Ti_4O_7 support is more stable than XC-72 when polarized over 0.9 V, but the maximum current density were not as high, due to larger Pt particle sizes on the oxide compared to the carbon. The difficulties with Pt particle size compared to carbon may be due to the lower oxide support surface areas (162 m²/g) [63]. The stability of the Ti_4O_7 needs further investigation in fuel cell conditions.

1.6.3 Carbon/graphite nanofibers (GNF)

Graphite nanofibers (GNFs) are catalytically grown by decomposition of carbon-containing gases over certain metal surfaces [64]. Park et al. [65, 66] obtained three types of GNFs by chemical vapour deposition method, i.e. ribbon-like, herringbone-like and platelet-like. The surface areas of these GNFs were 85, 45 and 120 m²/g, respectively. The diameter and length of the GNF were 100–150 nm and 5–50 mm, respectively.

Carbon fibers fibrous character offers an advantage for electrode layer packing due to their low resistance to flow of liquid and gases through a bundle of fibers. Therefore, they can be used as an alternative support material in fuel cell. In the structure of GNF, the edge plane regions are exposed [67] unlike CNTs where the basal plane is exposed, Due to exposed edge plane regions, there are lots of reactive groups for metal anchoring and GNFs can be modified with metal catalyst without any pre-treatment.

CNF-supported catalysts were prepared for use in fuel cells and their metal dispersion and catalytic activity was compared with that of other carbon supports [68-71]. Gangeri et al. [69] deposited Pt by incipient wetness impregnation on CNFs. Tests in PEMFC indicated that the cells with Pt/CNF as anode material better performed than those with Pt/Vulcan. Generally, it is

difficult to obtain high-loaded and well dispersed metal catalysts on CNFs due to small surface area. Knupp et al. [72] investigated the electrochemically active surface area of Pt supported on CNT and GNF. They found that GNF-supported catalyst gave comparable ECSA to CNT supported catalyst.

GNF might be an attractive candidate for future works in catalyst support area however; its stability in the fuel cell environment has not been tested yet. Due to high exposed edge plane structure, oxidation and corrosion of this material might be easier compare to CNT.

1.6.4 Ultrananocrystalline diamond (UNCD) powder

Ultrananocrystalline diamond (UNCD) also called ultrafine-dispersed diamonds (UDDs), is new kind of diamond formed of 3–6 nm crystallites made by detonation techniques and possesses unique properties and used for different applications. UNCD particles, which were discovered in the 1960s in the former USSR, applications include use in nanocomposites, selective adsorbents, colloidal suspensions, refrigerating fluids, microabrasives and many others.

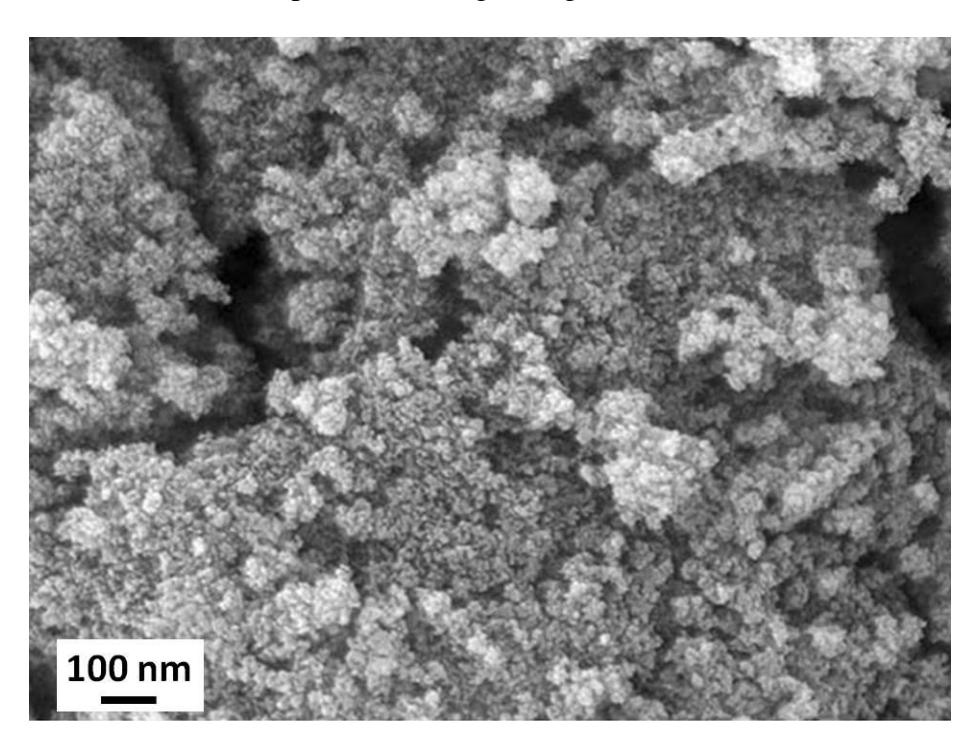


Figure 1.7 Typical high-resolution SEM image of detonation nanodiamond powder

Among these alternative materials, UNCD diamond possesses properties suited for an electrocatalyst support for fuel cells. It has high surface area (260 m²/g), superior morphological stability and corrosion resistance, compared to conventional sp² carbon support materials [73, 74]. It is chemically inert allowing for its use at elevated temperatures in oxidizing or reducing media without loss of properties. However, it is an electrically insulator and electrical conductivity is a barrier to use these materials as a support material for fuel cells.

Regarding to overcome of this conductivity barrier, several groups had been worked on the formation of conductive diamond powder preparation. Spătaru et al. [75] prepared conductive diamond powder in 150 μ diam. by mechanically crushing, free-standing BDD polycrystalline films obtained by chemical vapor deposition. In this approach, the Si support was removed with concentrated HF solution, and the remaining film was subjected to mechanical crushing. The limitation of this approach is surface area of the diamond powders due to large diamond powder size.

Another study for development of conductive diamond powder is formation of graphite shell over the diamond powder by high temperature [76, 77]. In this approach high surface area conductive diamond power can be achieved. However; the stability of catalyst coated graphite will be a problem during fuel cell operation. As the graphite layer corrodes the resistivity in the electrode layer would be increase.

High specific surface area forms of diamond can be also used as an electrically insulating diamond powders as catalyst supports for gas-phase chemical reactions [23-27]. These powders are electrically insulator. Any conductivity that exists in most of these powders can be attributed to nondiamond sp² carbon impurity present on the powder surface. Because of this, the electrical

conductivity becomes highly dependent on any disruption of this surface impurity phase, such as by electrochemical, chemical, or thermal oxidation. These surface phases are no more stable than bulk-phase sp² carbon materials.

Previously, our group reported on the preparation of BDD powder by coating insulating diamond powder (8–12 μ m diameter, 2m²/g) with a thin boron-doped layer using microwave plasma-assisted chemical vapor deposition to overcome electrical conductivity barrier to use diamond powders as a viable electrocatalyst support material. In this core-shell approach, the electrical conductivity is controlled by the doped-diamond layer (carrier concentration and mobility) rather than by some adventitious nondiamond sp² carbon impurity phase. The specific surface area and electrical conductivity of the doped diamond powder were 2 m²/g and 0.6 S/cm [78] which were below the targeted values.

Other work from our group has demonstrated that metal catalyst/diamond composite electrodes can be formed and show good electrocatalytic activity and excellent dimensional stability [79-82]. Electrodeposition was preferred for thin film diamond electrodes and electrodeposition of Pt occurs preferentially at boron rich areas. However, in these works the Pt particles were quite large or they were entrapped by secondary growth of diamond layer, [79-81] Very high stabilities were attained in corrosion tests, but the utilization of the Pt for fuel cell applications is low.

In this dissertation, high surface area (> 100 m²/g) conductive diamond powder was prepared as an alternative electrocatalyst support material for PEMFC application by overcoating 3-6 nm diameter diamond powder with a layer of boron-doped ultrananocrystalline diamond (B-UNCD). Determination of the basic electrochemical properties, verification of the material's

corrosion resistance and establishment of a protocol for depositing and stabilizing highly dispersed electrocatalyst particles on the diamond support were part of this effort.

Diamond powder is available from several commercial sources. The word "diamond" conjures up the idea of "high cost". This is simply not the case. Opposing to popular belief, diamond powders are not expensive. For example, most diamond powders are sold in large volumes worldwide for \$2-5/g. Table 1.1 compares the cost and surface area of different diamond powders, sp² carbon powders, and carbon nanotubes. Carbon blacks are less expensive than diamond powders, which are both less costly than carbon nanotubes. Vulcan powder is the least expensive and has the highest surface area ~ 220 m²/g. For comparison, graphite powder has a specific surface area of ca. 2 m²/g. It is important to note that while slightly more expensive than currently used carbons, diamond powders are not prohibitively expensive. This is a common misperception about diamond. Carbon nanotubes are much more expensive than diamond powders, and yet vary rarely is the material criticized for being too expensive. In our opinion, the perception of diamond as being "high cost" must be supplanted before diamond can become accepted as a possible new support material.

Although carbon blacks are the lowest cost starting material, a realistic cost assessment to produce the anode/cathode must include the metal catalyst. The Pt catalyst increases Vulcan to ca. \$50/g at a 20 wt % loading. Prices for diamond powders and carbon blacks are both $\leq 1\%$ compared to the metal catalyst. However, carbon blacks currently used as the catalyst support undergo microstructural degradation and corrosion leading to decreased performance and eventual loss of the expensive catalyst [12-16]. One can see that preserving the metal catalyst by using a corrosion resistant support, such as conductive diamond powder, produces cost and performance benefits by extending fuel cell lifetimes. The superior corrosion resistance of

Table 1.1 Approximate cost for some carbon materials currently used as or being considered for use as an electrocatalyst support.

Carbon Material	<u>Supplier</u>	Cost	<u>Surface</u>
		per gram	Area (m ² /g)
Vulcan XC-72R	Fuelcellstore.com	\$0.07	235
Vulcan/Pt 20 w %	Electrochem Inc.	\$50	
Graphite powder	Accumet Materials Co.	\$0.11	3
Diamond powder, 8-12 um	Diamond Innovations	\$3	1
Diamond powder, 0-2 um	Diamond Innovations	\$3	18
Diamond Powder, 0-0.1 um	Diamond Innovations	\$3	24
Diamond Powder, 500 nm	Tomei Corp.	\$5	8
Diamond Powder, 100 nm	Tomei Corp. \$17	\$17	52
Detonation Diamond Powder, 5 nm	NanoBlox	\$2	260
Carbon Nanotube AP-SWNT	Carbon solutions	\$50	260 ^a
Carbon nanotube	Carbolex	\$60	185 ^b

a [83], b [84]

conductive diamond, as compared other sp² carbon materials, is well documented [78]. We estimate the additional cost to produce conductive diamond powder from the seed diamond at only \$2-3/g depending on reactor type and deposition conditions.

The entire class of diamond powders referred to as detonation nanodiamond and have specific surface areas from 100 to 1000 m $^2/g$ We have been successfully preparing powders of

increased surface area up to about 170 m²/g. The measured specific surface area of each nonporous diamond powder is listed in Table 1.1 The surface area after overlayer formation is slightly lower than the starting material. This is caused by diamond layer growth over multiple, rather than individual, powder particles. This issue is discussed in the next chapter.

1.7 Research Goals and Objectives

Morphological and microstructural degradation of carbon electrocatalyst supports leads to reduced fuel cell efficiency, reduced electrode lifetime, and eventually, complete electrode failure. The research presented in this dissertation was focused on developing an alternative corrosion resistive, high surface area electrocatalyst support material for PEMFCS. We believe that boron doped ultrananocrystalline diamond (B-UNCD) powder possesses properties ideally suited for an electrocatalyst support for fuel cells. The diamond powder possesses high surface area, superior morphological stability and corrosion resistance. B-UNCD powder is chemically inert allowing for its use at elevated temperatures in oxidizing or reducing environments without loss of properties.

For the first time the performance of the membrane electrode assembly prepared using a high surface area (>100 m²/g), electrically conducting (>0.6 S/cm) diamond electrocatalyst support. There is still much to be learned in terms of MEA preparation and test conditions to obtain the best performance from the diamond powder supported fuel cells. For the first approach, the following research questions are addressed in the following chapters of this dissertation.

<u>Chapter 3:</u> The Physicochemistry and Electrochemical Properties of Diamond Powder Coated with Boron-Doped Ultrananocrystalline Diamond (B-UNCD)

1) Can a high-surface-area advanced electrocatalyst support material be made based on

electrically conducting diamond by B-UNCD layer over coating?

- High surface area (260 m²/g) insulator diamond powders were coated with a thin layer of boron doped diamond layer by microwave plasma-assisted chemical vapor deposition (PACVD) under ultrananocrystalline growth conditions.
- 2) What are the physical, chemical, and electrochemical properties and stability of B-UNCD diamond powder with respect to sp²-bonded carbons?
 - The B-UNCD diamond powders were studied using BET, cyclic voltammetry, SEM, and Raman spectroscopy.
 - Electrochemical responses of the B-UNCD powders were investigated by cyclic voltammetry via pipette electrode with three different redox systems to probe electron transfer reactivity on boron doped diamond powder.
 - The stability and electrochemical oxidation properties of these high surface area conductive sp³-bonded materials were compared to sp²-bonded carbon, under a controlled potential and temperature conditions.

<u>Chapter 4:</u> Characterization of Redox Active Surface of Carbon-Oxygen Functional Groups Formed on Boron Doped Ultrananocrystalline Diamond Coated Powders

- 1) What are the surface properties of B-UNCD layer coated diamond powders compare to sp² bonded carbon paper? What is the effect of anodic polarization for the oxide formation on B-UNCD powders?
 - The surface oxides properties of glassy carbon (GC) powder and 3-6 nm diamond powder were determined before and after overcoating by boron doped ultrananocrystalline diamond (B-UNCD) layer with Raman spectroscopy, cyclic

voltammetry, differential pulse voltammetry (DPV) and Fourier Transform Infrared (FTIR) spectroscopy.

<u>Chapter 5:</u> The Corrosion Resistance and Electroactivity of Pt-Loaded High Surface Area Conductive Diamond Powder For Oxygen Reduction

- 1) What is the interaction between electroctalayst Pt particles and B-UNCD diamond powder? How does Pt nanoparticle distributed on B-UNCD diamond powder surface and what is Pt particle size?
 - HRTEM images were obtain to study the Pt particle size and Pt distribution on B-UNCD-diamond powder. Statistical calculations performed to find the average particle size.
 - EELS, XRD, EDS spectra were obtain to understand the interaction of Pt-B-UNCD-diamond powder interaction.
- 2) What is the electrochemical activity of B-UNCD-diamond supported Pt electrocatalyst particles toward ORR compare to commercial Pt/Vulcan electrocatalyst? Are they stable on diamond powder surface? Does Pt particles influence diamond powder stability?
 - The kinetic parameters (Tafel slope, exchange current density, mass activity and specific activity) rotating disk electrodes (RDE) was prepared and cyclic voltammetry and linear sweep voltammetry were performed.
 - Amperometric i-t Curves were obtained to compare the oxidation current for B-UNCD diamond powder and Vulcan with and without Platinum to see the effect of Pt electrocatalyst on stability. HRTEM images were collected to analyze Pt particle distribution and any morphological change before and after anodic polarization.

<u>Chapter 6:</u> Performance of a Membrane Electrode Assembly Using a Diamond Powder Electrocatalyst Support

- 1) What is performance of the MEA prepared by B-UNCD-diamond powder support compare to Vulcan support MEA? Under accelerated degradation test conditions (200 hr cycling) is B-UNCD diamond electrocatalyst support stable or do it undergo microstructural degradation and corrosion?
 - The performance of membrane electrode assemblies (MEA) prepared by using the metal decorated B-UNCD powders were discussed. A 200 h life test in a single cell test assembly was carried out and open circuit potential and catalyst active area were monitored as a function of time. SEM images were obtained to characterize the MEAs before and after accelerated degradation test and results compared with Vulcan XC-72 powder supported MEAs.

1.8 Dissertation Outline

In this dissertation, the preparation of higher specific surface area (>100 m²/g) and electrically conducting (1 S/cm) diamond powders prepared by coating 500 nm, 100 nm and 3-6 nm diam. diamond particles with a layer of boron-doped nanocrystalline diamond is reported. In Chapter 2, the experimental parameters of the work in this dissertation including materials, instrumentation, and methods are presented. The fabrication and evaluation of the physicochemical, the morphological and microstructural properties and stability of B-UNCD-diamond powders is presented Chapter 3. In Chapter 4 surface chemistry of B-UNCD diamond powder was characterize and surface oxidation was studied by electrochemical anodic polarization. The Pt impregnation and electrochemical activity and of Pt/B-UNCD-diamond powder towards ORR is described in Chapter 5. The stability and corrosion resistance of this

new material is compared to commercial carbon support material. Chapter 6 presents the performance of membrane electrode assemblies (MEA) prepared by using the metal decorated B-UNCD powders. A 200 h life test in a single cell test assembly was carried out and open circuit potential and catalyst active area were monitored as a function of time. SEM images were obtained to characterize the MEAs before and after life test and results compared with Vulcan XC-72 powder supported MEAs. Finally, future directions for this research are proposed in Chapter 7.

References

- 1. Report of the Basic Energy Sciences Workshop on Hydrogen Production, Storage, and Use, Argonne National Laboratory: Argonne, IL, 2003.
- 2. M. Watanabe, H. Uchida and M. Emori. J. Electrochem. Soc. 145, p. 1137, 1998.
- 3. M. F. Mathias, R. Makharia, H. A. Gasteiger, et al., "Two Fuel Cell Cars in Every Garage", Interface 14, 24, 2005.
- 4. Roen, L. M.; Paik, C. H.; Jarvi, T. D. Electrochem. Solid-State Lett., 7, A19, 2004.
- 5. Yu, P. T.; Gu, W.; Makharia, R.; Wagner, F. T.; Gasteiger, H. A.ECS Trans., 3, 797, 2007.
- 6. Kinoshita, K. Carbon: Electrochemical and Physicochemical Properties; Wiley: New York, 1988.
- 7. M. Winter and R.J. Brodd, "What Are Batteries, Fuel Cells, and Supercapacitors?", Chern. Rev., 104, p 4245-4270, 2004.
- 8. www.scientific-computing.com
- 9. Appleby, A. J. Corrosion (Houston), 43, 398-408, 1987.
- 10. Auer, E.; Freund, A.; Pietsch, J.; Tacke, T. Appl. Catal. A., 173, 259-271, 1998.
- 11. Antolini, E. J. Appl. Electrochem., 34, 563-576, 2004.
- 12. M. W. Reed and R. J. Brodd, Carbon, 3, 241, 1965.
- 13. L. M. Roen, C. H. Paik, and T. D. Jarvi, Electrochem. Solid-State Lett., 7, A19, 2004.
- 14. C. H. Paik, T. D. Jarvi, and W. E. O'Grady, Electrochem. Solid-State Lett., 7, A82, 2004.
- 15. E. Antolini, J. Mater. Sci., 38, 2995, 2003.
- 16. A. J. Appleby, Corrosion (Houston), 43, 398, 1987.
- 17. U.S. DOE, http://www1.eere.energy.gov/hydrogenandfuelcells/mypp/, 2007.
- 18. E. Auer, A. Freund, J. Pietsch, T. Tacke, Appl. Catal. A 173, 259, 1998.
- 19. E. Antolini, Applied Catalysis B: Environmental 88, 1–24, 2009.
- 20. Roen, L. M.; Paik, C. H.; Jarvi, T. D. Electrochem. Solid-State Lett., 7, A19, 2004.

- 21. Mathias, M. F.; Makharia, R.; Gasteiger, H. A.; Conley, J. J.; Fuller, T. J.; Gittleman, C. J.; Kocha, S. S.; Miller, D. P.; Mittelsteadt, C. K.; Xie, T.; Yan, S. G.; Yu, P. T. Interface, 14, 24, 2005.
- 22. Taniguchi, A.; Akita, T.; Yasuda, K.; Miyazaki, M. J. Power Sources, 130, 42, 2004.
- 23. Knights, S. D.; Colbow, K. M.; St-Pierre, J.; Wilkinson, D. P. J. Power Sources, 127, 127, 2004.
- 24. Reiser, C. A.; Bregoli, L.; Patterson, T. W.; Yi, J. S.; Yang, J. D.; Perry, M. L.; Jarvi, T. D. Electrochem. Solid-State Lett., 8, A273, 2005.
- 25. Meyers, J. P.; Darling, R. M. J. Electrochem. Soc., 153, A1432, 2006.
- 26. Hao Tang, Zhigang Qi *, Manikandan Ramani, John F. Elter Journal of Power Sources Volume 158, Issue 2, Pages 1306-1312, 2006.
- 27. Binder, H.; Kohling, A.; Richter, K.; Sandstede, G. Electrochim. Acta, 9, 255, 1964.
- 28. Kinoshita, K.; Bett, J. Carbon, 11, 237, 1973.
- 29. Kinoshita, K.; Bett, J. A. S. Carbon, 11, 403, 1973.
- 30. McBreen, J.; Olender, H.; Srinivasan, S.; Kordesch, K. V. J. Appl. Electrochem., 11, 787, 1981.
- 31. Stonehart, P. Carbon, 22, 423, 1984.
- 32. Antonucci, P. L.; Romeo, F.; Minutoli, M.; Alderucci, E.; Giordano, N. Carbon, 26, 197, 1988.
- 33. Passalacqua, E.; Antonucci, P. L.; Vivaldi, M.; Patti, A.; Antonucci, V.; Giordano, N.; Kinoshita, K. Electrochim. Acta, 37, 2725, 1992.
- 34. Pyun, S.-I.; Lee, E.-J.; Kim, T.-Y.; Lee, S.-J.; Ryu, Y.-G.; C.-S., K. Carbon, 32, 155, 1994.
- 35. Pyun, S.-I.; Ryu, Y.-G.; Choi, S.-H. Carbon, 32, 161, 1994.
- 36. Kiho, M.; Matsunaga, K.; Morikawa, S.; Kato, O. Electrochemistry, 69, 580, 2001.
- 37. Gruver, G. A. J. Electrochem. Soc., 125, 1719, 1978.
- 38. G. Che, B.B. Lakshmi, E.R. Fisher, C.R. Martin, Nature 393, 346. 1998.
- 39. B. Rajesh, V. Karthik, S. Karthikeyan, K.R. Thampi, J.M. Bonard, B. Viswanathan, Fuel 81, 2177, 2002.

- 40. Z.L. Liu, X.H. Lin, J.Y. Lee, W.D. Zhang, M. Han, L.M. Gan, Langmuir 18, 4054, 2002.
- 41. S.L. Knupp, W. Li, O. Paschos, T.M. Murray, J. Snyder, P. Haldar, Carbon 46, 1276, 2008.
- 42. T. Matsumoto, T. Komatsu, H. Nakano, K. Arai, Y. Nagashima, E. Yoo, T. Yamazaki, M. Kijima, H. Shimizu, Y. Takasawa, J. Nakamura, Catal. Today 90, 277, 2004.
- 43. C. Kim, Y.J. Kim, Y.A. Kim, T. Yanagisawa, K.C. Park, M. Endo, M.S. Dresselhaus, J. Appl. Phys. 96, 5903, 2004.
- 44. Y. Xing, J. Phys. Chem. B 108, 19255, 2004.
- 45. C. Wang, M. Waje, X. Wang, J.M. Tang, C.R. Haddon, Y. Yan, Nano Lett. 4, 345, 2004.
- 46. Lee, K.; Zhang, J. J.; Wang, H. J.; Wilkinson, D. P. J. Appl. Electrochem., 36, 507, 2006.
- 47. T. Maiyalagan, B. Viswanathan, U.V. Varadaraju, Electrochem. Commun. 7, 905, 2005.
- 48. E. Yoo, T. Okada, T. Kizuka, J. Nakamura, J. Power Sources 180, 221, 2008.
- 49. K. Ke, K. Waki, J. Electrochem. Soc. 154, A207, 2007.
- 50. W. Li, C. Liang, J. Qiu, W. Zhou, H. Han, Z. Wei, G. Sun, Q. Xin, Carbon 40, 791, 2002.
- 51. X. Wang, M. Waje, Y. Yan, Electrochem. Solid State Lett. 8, A42 2005.
- 52. J.J. Wang, G.P. Yin, J. Zhang, Z.B. Wang, Y.Z. Gao, Electrochim. Acta 52, 7042, 2007.
- 53. D.J. Guo, L. Zhao, X.P. Qiu, L.Q. Chen, W.T. Zhu, J. Power Sources 177, 334, 2008.
- 54. H.T. Zheng, Y. Li, S. Chen, P.K. Shen, J. Power Sources 163, 371, 2006.
- 55. S. Liao, K. Holmes, H. Tsaprailis, V.I. Birss, J. Am. Chem. Soc. 128, 3504, 2006.
- 56. A. Kongkanand, S. Kuwubata, G. Girishkumar, P. Kamat, Langmuir 22, 2392, 2006.
- 57. O. Paschos, S.L. Knupp, P. Choi, J. Snyder, S.J. Buelte, N. Merchant, Z. Qi, P. Haldar, Electrochem Solid State Lett. 10, B147, 2007.
- 58. W.H. Zhang, J.L. Shi, L.Z. Wang, D.S. Yan, Chem. Mater. 12, 1408, 2000.
- 59. Z.L. Liu, X.H. Lin, J.Y. Lee, W.D. Zhang, M. Han, L.M. Gan, Langmuir 18, 4054, 2002.
- 60. F.B. Su, J.H. Zeng, X.Y. Bao, Y.S. Yu, J.Y. Lee, X.S. Zhao, Chem. Mater. 17, 3960, 2005.

- 61. Dieckmann, G. R.; Langer, S. H. Electrochim. Acta, 44, 437, 1998.
- 62. Ioroi, T.; Siroma, Z.; Fujiwara, N.; Yamazaki, S.; Yasuda, K. Electrochem. Commun., 7, 183, 2005.
- 63. Journal of Colloid and Interface Science Volume 304, Issue 1, Pages 166-171, 2006.
- 64. N.M. Rodriguez, A. Chambers, R.T.K. Baker, Langmuir 11, 3862, 1995.
- 65. C. Park, R.T.K. Baker, J. Phys. Chem. B 102, 5168, 1998.
- 66. C. Park, R.T.K. Baker, J. Phys. Chem. B 103, 2453, 1999.
- 67. C.A. Bessel, K. Laubernds, N.M. Rodriguez, R.T.K. Baker, J. Phys. Chem. B 105, 1115, 2001.
- 68. B.O. Boskovic, V. Stolojan, R.U.A. Khan, S. Haq, S.R.P. Silva, Nat.Mater. 1, 165, 2002.
- 69. M. Gangeri, G. Centi, A. La Malfa, S. Perathoner, R. Vieira, C. Pham-Huu, M.J.Ledoux, Catal. Today 102/103, 50, 2005.
- 70. F. Yuan, H. Ryu, Nanotechnology 15, S596, 2004.
- 71. N.M. Rodriguez, M.S. Kim, R.T.K. Baker, J. Phys. Chem. 98, 13108, 1994.
- 72. S.L. Knupp, W. Li, O. Paschos, T.M. Murray, J. Snyder, P. Haldar, Carbon 46, 1276, 2008.
- 73. J. Xu, M.C. Granger, Q. Chen, T.E. Lister, J.W. Strojek, G.M. Swain, Anal. Chem. 69, 591 1997.
- 74. Q. Chen, M.C. Granger, T.E. Lister, G.M. Swain, J. Electrochem. Soc. 144, 3806, 1997.
- 75. N. Spataru, X. Zhang, T. Spataru, D. Tryk, A. Fujishima, J. Electrochem. Soc. 155, B264, 2008.
- 76. Yury Gogotsi, Sascha Welz, Daniel A. Ersoy, Michael J. McNallan Nature 411, 283-287, 2001
- 77. Sascha Welz, Yury Gogotsi, Michael J. McNallan, J. Appl. Phys. 93, 4207, 2003
- 78. A. E. Fischer and G. M. Swain, J. Electrochem. Soc., 152, B369, 2005.
- 79. J. Wang and G. M. Swain, Electrochem. Solid-State Lett., 3, 286, 2000.
- 80. J. Wang, G. M. Swain, T. Tachibana, and K. Kobashi, J. New Mater. Electrochem Syst., 3, 75, 2000.

- 81. J. Wang and G. M. Swain, Electrochem. Solid-State Lett., 5, E4, 2002.
- 82. Bennett, J. A.; Show, Y.; Wang, S. H.; Swain, G. M. J. Electrochem. Soc., 152, E184, 2005.
- 83. Anson Ma,1 Jun Lu,1 Shihe Yang,2,3 and Ka Ming Ng1 Journal of Cluster Science, Vol. 17, No. 4, 2006.
- 84. R. A. H. Niessen,a,z J. de Jonge,b and P. H. L. Notten Journal of The Electrochemical Society, 153 (8) A1484-A1491, 2006.

Chapter 2

Experimental Methods

2.1 Boron doped-Ultrananocrystalline Diamond (B-UNCD) layer overcoating

The boron-doped ultrananocrystalline diamond overlayer was grown on insulating diamond powder (*Nanostructured and Amorphous Materials*, Houston, TX, 3-6nm diam., Tomei Diamond Co., Cedar Park, TX 100 and 500 nm diam.) by microwave plasma-assisted CVD (1.5 kW ASTeX, Inc., Lowell, MA). A reactor consists of a quartz bell jar (10 cm in diameter and 17 cm in height). A plasma discharge in the reactor by focusing the microwave energy just above a molybdenum substrate stage is formed. A 1500 W, 2.45GHz power supply is used to supply the microwave energy. The substrate temperature was estimated using an infrared pyrometer. The chamber pressure was maintained by a throttle exhaust valve in serves with a rotary pump that was operated continuously during diamond growth.

The concept of overcoating electrically insulating diamond powder with a conductive layer of B-UNCD is illustrated in Figure 2.1. The diamond powders were prepared for deposition by sequential cleaning in warm (60 °C) aqua regia (30 min) and warm 30 % hydrogen peroxide (30 min) to remove nondiamond sp²-bonded carbon and metallic impurities. The clean powder was then copiously rinsed with ultrapure water, isopropyl alcohol (IPA), and acetone by ultrasonication. Each liquid was carefully decanted and afterward the powder was dried at 80 °C overnight in air. The diamond deposition was performed by spreading approximately 30 mg of the powder thinly over a silicon wafer that was placed in the reactor. The deposition conditions for the B-UNCD overlayer were as follow: (i) a source gas mixture of CH₄/H₂+Ar (94% Ar) consisting of 1.0% CH₄/H₂ and 10 ppm B₂H₆, (ii) a microwave power of 800 W, and (iii) a

pressure of 140 Torr. The deposition temperature was estimated with an optical pyrometer to be $750\,^{\circ}$ C. The powders were coated twice, and the growth period for each was 2 h. After the first growth, the sample was mixed and re-spread over the silicon wafer in order to try and maximize the diamond coverage over the powder surface. A post-growth annealing and cool-down procedure was employed at the end of each deposition period to minimize the formation of adventitious sp² carbon impurity and to ensure maximum hydrogen surface termination. This procedure involved stopping the CH₄ and B₂H₆ gas flows, leaving the sample exposed to an H₂/Ar plasma for 10 min. The microwave power and pressure were then slowly reduced over 20min period to 100 W and 50 Torr. The plasma was then extinguished and the sample cooled to room temperature under an H₂/Ar flow for 10 min. Post-growth, the powders were cleaned chemically, as described above, with an additional hydrofluoric and nitric acid exposure to remove any silicon impurity [2]. Any sp² carbon phase was oxidized by exposed to a 30 w % H₂O₂ solution for 30 min. The clean and oxidized B-UNCD powder was then copiously rinsed with ultrapure water, IPA, and acetone and dried at 80 °C overnight in air.

This deposition approach is less than ideal because the powder particles are only partially coated with diamond and because there is particle aggregation that occurs due to diamond deposition over multiple neighboring particles. Additionally, the variable height of the powder particles in the plasma leads to temperature variations during film growth, which results in differences in overlayer coverage thickness and microstructural quality. Particles that experience higher temperatures tend to have more nondiamond carbon impurity content.

Glassy carbon powder (Sigradur G, HTW GmBH, Germany, 4 μ m diam. and 2m²/g.) was used as received without any cleaning or seeding. An overlayer of B-UNCD

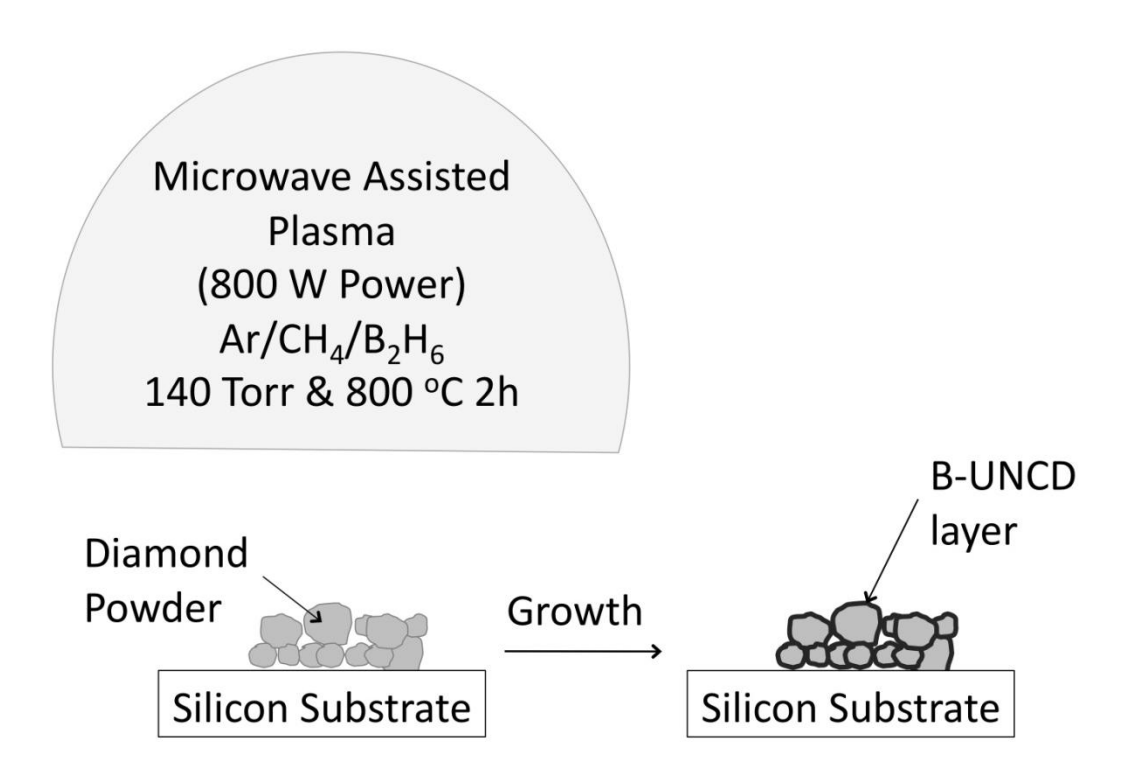


Figure 2.1 Illustration of the core-shell concept for coating diamond powders with a layer of boron-doped ultrananocrystalline diamond. [15]

was grown using the following conditions: (i) a source gas ratio of 1% CH_4 , 7% H_2 and 92% Ar. 10 ppm (1 x 10^{-3} %) of B_2H_6 , (ii) a microwave power of 800 W, and (iii) a system pressure of 140 Torr. The sample was coated twice, and the growth period for each was 2 h. After each growth, the same post-growth annealing and cool-down procedure in atomic hydrogen was applied, as explained above. These powders were used as-grown without any chemical treatment after coating.

2.2 Material Characterization

A number of analytical methods were used to characterize the diamond properties, including, X-ray diffraction (crystallinity), visible Raman spectroscopy (microstructure), scanning electron microscopy and transmission electron microscopy (morphology), BET measurements (specific surface area), and current-voltage curves (electrical conductivity).

2.2.1 Scanning Electron Microscopy (SEM)

The sample morphology was probed by field-emission scanning electron microscopy (JSM-6400F, JEOL, Ltd., Tokyo, Japan) using a 20 kV accelerating voltage and a working distance of 15 mm. Some of the less conducting diamond powders were sputter coated with Au to improve the image quality by reducing surface charging.

2.2.2 Transmission Electron Microscopy (TEM)

For the transmission electron microscopy measurement, ~0.5 mg of the diamond powder was ultrasonically mixed with 10 mL IPA and few drops were casted on to a lacey carbon coated-copper grid (size 200 mesh). Images were obtained using a JEOL JEM-2200FS electron microscope operating at an accelerating voltage of 200 kV.

2.2.3 X-Ray Diffraction Spectroscopy (XRD)

The diamond powder crystallinity was studied by XRD. Diffraction patterns were obtained by scanning 20 from 20 to 100 on a Rikagu Rotaflex RTP300 RC instrument. X-rays were produced at 1.540 Å from a Cu anode.

2.2.4 Raman Spectroscopy

Raman spectra were recorded in a backscattered collection geometry using a 100 mW argon ion laser (Melles Griot CW) at 514.5 nm, an Olympus BH-2 microscope assembly, and a

Spex 1250 spectrograph with a 600 grooves/mm holographic grating. The detector was a Symphony 2000 x 800 charge-coupled device (Horiba Jobin-Yvon) with a pixel size of 15 μ m. All spectra were recorded at room temperature using an incident power density of approximately 1.4 kW/cm² (10 mW at the sample and 30 μ m diam spot size) and a 45 s integration time. The spectrometer was calibrated using the first-order phonon peak for cubic diamond (a high-pressure, high temperature-grown single-crystal sample) at 1332.6 cm⁻¹.

2.2.5 Electrical Resistance

The electrical resistance of the boron-doped diamond powder was determined by placing a fixed quantity (ca. 30 mg) of powder inside a vertical glass tube (area 0.11 cm^2). Two copper plates contacted the powder on both sides of the tube. One of these plates was small enough in diameter to fit inside the glass tube and was pressed against the powder using a 240 g weight. A schematic diagram of the apparatus used to measure i-V curves is shown in Figure 2.2. Contact-to-contact resistance was measured using an ohmmeter. Current–voltage curves were also generated by applying ± 6 , ± 10 , and ± 20 mA currents and recording the corresponding voltage drop. The conductivity (S/cm) was calculated from the measured resistance, R (Ω), and dividing by the powder thickness, 1 (cm).

2.2.6 Specific surface area measurements

The powder surface area was determined by the BET method. Nitrogen adsorption isotherms were recorded at -196 °C using a Micromeritics Tristar 3000 sorptometer following standard protocols. Approximately 300 mg powder sample was out gassed at 90 °C and 10^{-6} Torr for a minimum of 12 h prior to analysis. The sample, in vacuum, was exposed to different

amounts of N_2 gas and the chamber pressure was measured. The greater the coverage of adsorbed gas, the lower the system pressure is. An adsorption isotherm was generated by plotting 1/v [(P_0/P) – 1] vs. P/P_0 (BET plot). P and P_0 are the equilibrium and the saturation pressures of nitrogen at the isotherm temperature, and v is the volume of gas adsorbed. Surface areas were calculated from the linear part of the BET plot according to International Union of Pure and Applied Chemistry (IUPAC) recommendations [3].

2.2.7 Electrochemical Characterization

Electrochemical measurements are important to record as they provide insight on the physicochemical properties of conductive diamond powders. The working potential window, the background current and various voltammetric features are all diagnosis of the surface microstructure and chemistry, electronic properties, and electric double-layer structure.

Cyclic voltammetry was used to 1) probe the electrochemical properties of the B-UNCD and glassy carbon powders, 2) evaluate the microstructural stability of B-UNCD-diamond and B-UNCD-glassy carbon powders, and 3) study the electrochemical properties of Pt nanoparticles deposited on the B-UNCD-diamond powders.

All of the electrochemical measurements were performed using a CHI650a computerized potentiostat (CH Instruments Inc., Austin, TX) with a graphite rod counter electrode and a Ag/AgCl reference electrode (4 M KCl, $E^{\circ\prime}$ = -65 mV vs. SCE). All measurements were made at room temperature (25 ± 1 °C), unless otherwise noted, and all solutions were deoxygenated with N₂ for at least 20 min prior to a measurement and blanketed with the gas during the measurement. Details of the electrode preparation procedures and the electrochemical cells used for each electrode morphology are provided below.

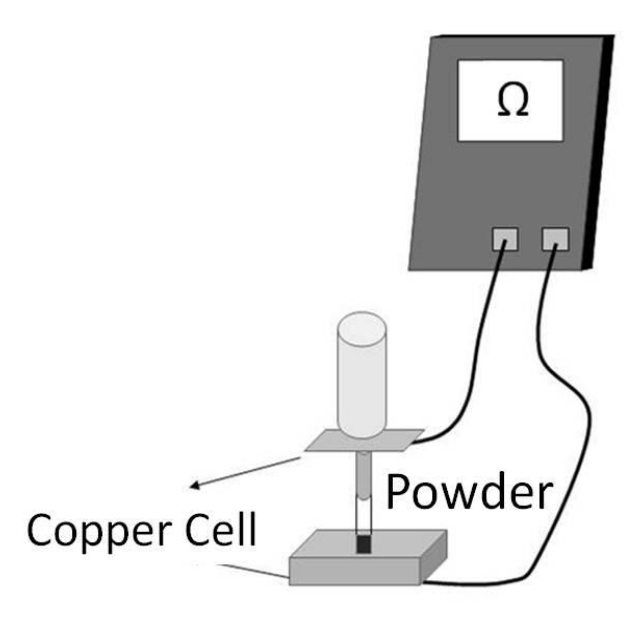


Figure 2.2 Schematic diagram of the apparatus used to measure i-V curves for the powder samples.

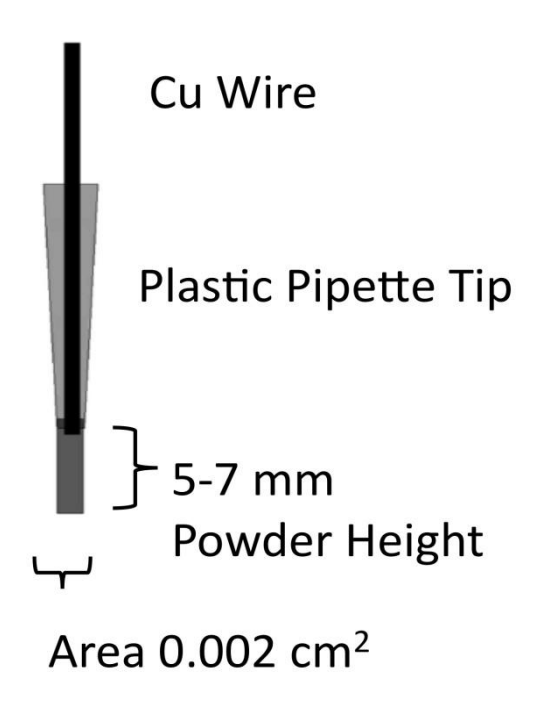


Figure 2.3 Diagram of the pipette electrode used for testing the electrochemical properties of the conducting powder. (Adapted from [15])

2.2.8 Polarization Studies

B-UNCD-diamond powder and platinized diamond powders were subjected to applied potentials from 1.0 to 1.6 V vs. Ag/AgCl at 25 and 80 $^{\circ}$ C in 0.5 M H₂SO₄ for 1 h periods. The measurements were performed in the continuous amperometric mode with the current being recorded as a function of time. The single compartment glass electrochemical cell was heated by hot water circulation. The solution temperature was measured before and after the polarization and remained constant (\pm 5 $^{\circ}$ C). The recorded current-time profiles were integrated to determine the charge passed at a given potential. For a faradaic process, the charge passed is related to the number of moles electrolyzed according to Equation 2.1:

$$Q = nFN [2.1]$$

where Q is the integrated charge (Coulombs), n is the number of electrons involved per reaction, F is the Faraday constant, and N is the number of moles electrolyzed.

2.2.9 Electrode Preparation and Experimental Setup

2.2.9.1 Film Electrodes

The diamond thin-film on Si (~0.2 cm² area) or glassy carbon electrodes were sealed against the bottom of a single-compartment electrochemical cell with a Viton[®] o-ring [5]. The backside of the Si substrate was scratched, cleaned, and coated with graphite in order to ensure good ohmic contact with a metal current collector plate. All electrodes were used after a 20 min soak in distilled isopropyl alcohol [6].

2.2.9.2 Carbon Powder Electrodes

Electrochemical characterization is not straightforward when the electrode material is a powder. Generally, some method for anchoring the particles is necessary. For example, composite electrodes can be prepared using a polymer binder or other chemical, like paraffin oil [13]. Polymeric binders tend to reduce the particle–particle contact, thereby increasing the electrode resistance. Furthermore, the mixing, pressing, and heating steps needed for the electrode preparation are laborious and time consuming. The pipette electrode architecture used in this work enables electrochemical characterization of the doped diamond powders without the need for a binder. Electrochemical characterization was performed with electrodes prepared by packing the powder into a plastic pipette tip (#104 BioDot, Scientific Inc., Burton, MI) [7]. The procedure involved first melting the narrow end of the tube closed. Then, 5–10 mg of either boron-doped diamond or GC powder (Sigradur G, HTW GmBH, Germany) was packed into the tube with a 1 mm diam. copper metal rod. This metal rod also served as the current collector (see Fig. 2.3). The powders were packed to a height of 6–7 mm with the Cu wire embedded in the top of the powder. The Cu wire was pressed into the powder layer to form good ohmic contact. The closed end of the tip was then carefully cut open to expose the powder with a geometric area of ~0.002 cm². All currents are normalized to this geometric area.

2.3 Reagents

All chemicals were analytical-grade quality, or better, and were used without additional purification. Solutions (1 mM) of potassium ferrocyanide (Aldrich), potassium hexachloroiridate (Aldrich), and ferric sulfate (Matheson Coleman and Bell) were prepared fresh daily. The supporting electrolytes were 1 M KCl (Fisher Scientific), 0.5 M H₂SO₄ (99.999%, Aldrich), and 0.1 M HClO₄ (99.999%, Aldrich). The solutions used for the electrochemical studies for surface

oxide characterization (Chapter 4) were 0.5 M H_2SO_4 (pH 0.1) (Fisher Scientific) and 0.1 M NaOH (pH 14) (Aldrich). All redox analyte solutions were prepared daily using ultrapure water (>18 $M\Omega$ -cm) from an E-pure water purification system (Barnstead) in glassware that was cleaned by a three-step process: ethanol/KOH bath, alconox/ultrapure water solution, and an ultrapure water rinse.

2.4 Chapter-Specific Experimental Methods

2.4.1 Fourier Transform Infrared (FTIR) (Chapter 4)

FTIR microscopy was performed to investigate effects of anodic polarization on surface oxide functional groups formed on the B-UNCD-coated and uncoated powders. Spectra were collected using a Mattson Galaxy FTIR spectrometer in the transmission mode. The powders were milled with 150 mg of potassium bromide (Aldrich) at a 1/150 mass ratio to form a very fine powder. 100 mg of this powder was taken and compressed into a thin pellet.

2.4.2 Differential Pulsed Voltammetry (DPV) (Chapter 4)

Differential pulse voltammetry (DPV) was used to determine whether different surface functional groups present on the diamond and glassy carbon powders are electrochemically active [4]. In DPV measurements, the potential wave form consists of small pulses (of constant amplitude) superimposed upon a staircase wave form (Figure 2.4). The current is measured before each potential change, and the current difference is plotted as a function of potential. By sampling the current just before the potential is changed, the effect of the charging current can be decreased. Therefore, this technique can be used to identify quantities of surface reactants which are too small to be found with cyclic voltammetry alone.

On a base potential (0 V), small amplitude of fixed potential pulse (10mV) is applied during pulse width (50msec). Each potential pulse is superimposed on a slowly changing base

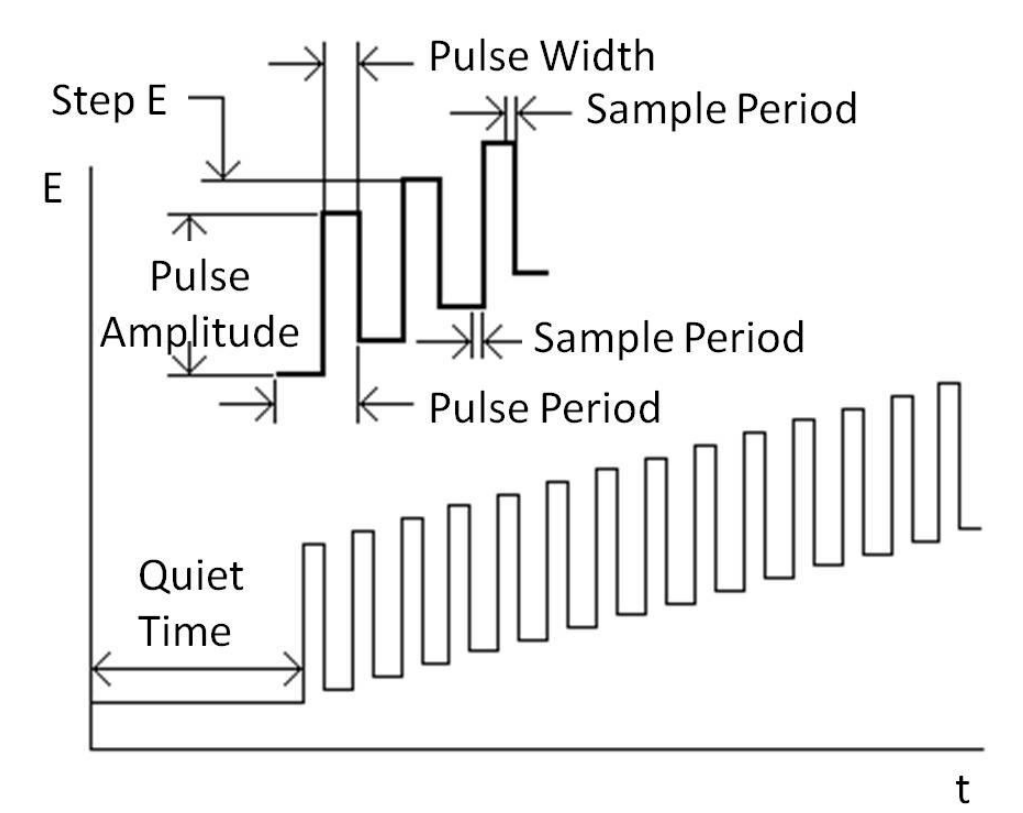


Figure 2.4. Potential wave form for differential pulse voltammetry (From [16])

potential (1 mV increment). Current is measured at two points during each pulse, the first point just before the application of the pulse and the second at the end of the pulse. Pulse period is 200msec. Powders erre anodicly polarized at 1.2, 1.0 V and 1.6 V vs. Ag/AgCl electrode (25 °C) for 1 h. After each polarization, cyclic voltammetry and DPV measurements were recorded to probe the electrochemical properties.

2.4.3 Pt deposition on diamond powders (Chapter 5)

The conducting diamond powder was impregnated with Pt by a wet chemical process. In this method, an appropriate quantity of the Pt(II) acetylacetonate salt (Aldrich) was dissolved in 25 mL of ethanol and acetic acid (Aldrich) 3:2 (v/v). After that, an appropriate amount of the diamond powder was added to yield a theoretical catalyst loading of 20%. The mixture was

homogenized by ultrasonic mixing for 30 min (Fisher Scientific, FS30 Sonicator). The solvent was then slowly evaporated while the suspension was continuously stirred. The powder was then submitted to a thermal treatment at 400° C for 30 min in order to stabilize the platinum.

2.4.4 Rotating Disk electrode preparation (Chapter 5)

A glassy carbon rotating disk electrode (Brinkmann Instruments, 3 mm diam, 0.07 cm²) served as substrate for the Pt/B-UNCD-diamond powder catalyst. The electrode was mechanically polished on separate felt polishing cloths using aqueous slurries of 1.0, 0.3, and 0.05 μm diam. deagglomerated alumina powder (Buehler, Ltd., Illinois) After each polishing step, the electrode was copiously rinsed with ultrapure water and ultrasonically cleaned in ultrapure water for 10 min. Aqueous suspensions of 2 mgpt/mL were produced by stirring 10 mg of the Pt/B-UNCD-diamond powders in isopropyl alcohol (Aldrich) (IPA) for 4 hours. A 30 μL aliquot of the suspension was pipetted onto the glassy carbon substrate, yielding a Pt loading of 0.05 mg/cm². After evaporation of the IPA, diluted (0.05 wt %) Nafion solution (originally 5 wt %, ElectroChem) was put on top of the dried catalyst powder. The volume of the Nafion solution used was calculated to yield a Nafion film thickness of 0.1 μm. (Nafion solution density 0.924 g/cm³, dry Nafion density 1.99 g/cm³) A final cure in an oven (air atmosphere) at 80 °C for 30 min was then applied to cured Nafion.

After preparation, the electrode was immersed in 0.5 M H_2SO_4 and purged with N_2 for 30 min. Under the N_2 blanket, the potential was cycled between 0 and 1.1 mV vs. RHE. The voltammetric i-E curve usually stabilized within five cycles at 5 mV/s. The charge for H^+ desorption (between 0.0-0.3 V) was used to determine the electrochemically active Pt surface

area, assuming a 1H:1Pt surface interaction and a columbic charge of 210 μ C/cm² for monolayer hydrogen adsorption on an atomically flat Pt(111) surface [8]. For the oxygen reduction reaction, linear sweep voltammograms were recorded in oxygen-saturated 0.5 M H₂SO₄ electrolyte. The corrosion resistance of the platinized powders was tested by anodic polarization in 0.5M H₂SO₄ (25 $^{\circ}$ C) at 1.2 V vs. RHE for 1 h. Comparison measurements were made using 20 wt % Pt/Vulcan XC-72 powder (ETEK).

For the oxygen reduction reaction studies, linear sweep voltammograms were recorded in oxygen-saturated $0.5\ M\ H_2SO_4$.

2.4.5 Atomic absorption spectroscopy (Chapter 5)

To determine the actual Pt loading, 10 mg of platinized diamond powder was dissolved in 4 mL warm aqua-regia for 1 h. The aqua-regia was prepared by mixing 3 mL HCl (36.5-38.0 % Columbus Chemical Industries, Inc., Columbus, WI) and 1 mL HNO₃ (70% Columbus Chemical Industries.). Pt is known to dissolve in warm aqua-regia, while the diamond powder is quite stable. The yellowish solution was carefully decanted to a clean beaker at the end of the digestion period. The powder was then rinsed with ultrapure water several times and these rinses were collected and mixed with original acid solution. The total solution volume was increased to 80 mL by addition of ultrapure water. AAS was performed directly on this solution using a Hitachi Z-9000 Atomic Absorption spectrophotometer (Hitachi, Ltd., Tokyo, Japan) with a graphite tube furnace.

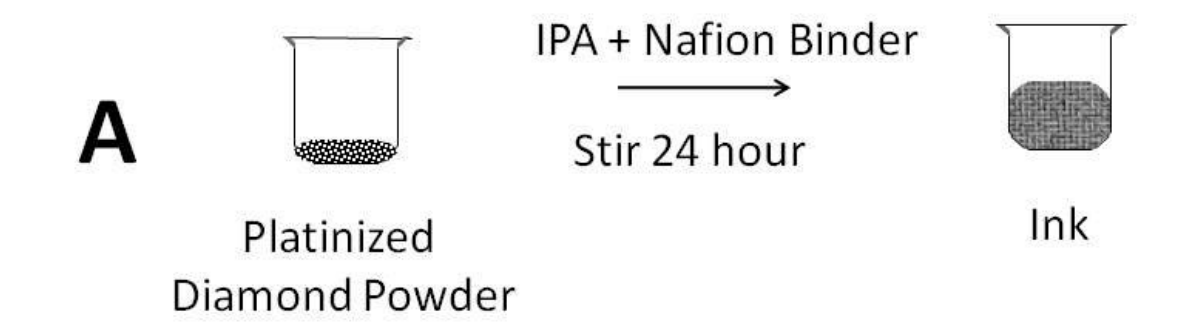
2.4.6 X-ray photoelectron spectroscopy (Chapter 5)

The XPS system is a Kratos Axis-165 equipped with both Al/Mg twin-anode and monochromated Al X-ray guns. The analyzer has 8 channeltrons for collecting high energy-resolution spectra. The Kratos system has a unique charge neutralizer built into the lens assembly to compensate for charging in insulating materials. It is also fitted with an ion gun for sputter-cleaning and ion-scattering spectroscopy.

2.5 Membrane Electrode Assembly (MEA) preparation (Chapter 6)

MEAs were prepared by the catalyst-coated membrane (CCM) method. The preparation steps are illustrated in Figure 2.5. The electrodes were prepared from an ink that consisted of the carbon-supported Pt catalyst, the ionomer solution (5 wt. % colloidal Nafion, 0.924 g/cm³, Sigma Aldrich) and isopropyl alcohol. The mass ratio of liquids (ionomer solution and isopropanol) to solids (ionomer, carbon and catalyst) in the catalyst inks was ca. 5. Different ionomer weight ratios were used (15, 40 and 60 wt. % Nafion) to prepare catalyst inks. For Vulcan MEAs, the mass ratio of ionomer to carbon and catalyst in the ink was ~ 40 wt. %. The optimum Nafion content in the electrode layer, as a function of the support material and electrocatalyst weight, was determined by finding the ratio of Nafion content (mg) to electrode weight (support material, electrocatalyst and Nafion content weight in mg).

Inks were prepared by stirring platinized powders and the Nafion ionomer in isopropyl alcohol for 12-20 h at room temperature. The electrodes were formed by slot-coating the ink on to 0.5-mm thick PTFE decals using slots 1 cm² in area. The slots were prepared with double-sided tape. Each decal was coated 2 times with intermediate drying at ca. 80 °C. Loadings were calculated by weighing the decals before (blank) and after applying the catalyst. Before the decal



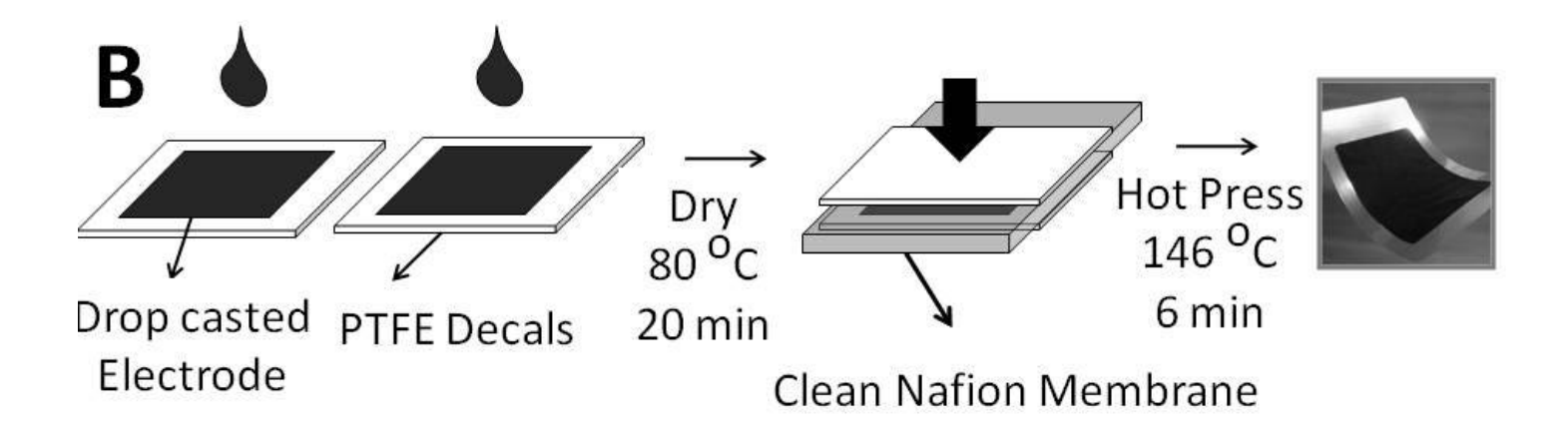


Figure 2.5 (A) Ink preparation from platinized diamond powder, Nafion binder and isopropyl alcohol. (B) MEA preparation procedure from ink drop casting and hot press.

transfer process, Nafion 115 membranes (DuPont) were cleaned as follows:(i) 1-h exposure to boiling 3% H_2O_2 solution to remove organic impurities; (ii) rinsing with boiling H_2O ; (iii) 1-h exposure to 1 M H_2SO_4 to remove metallic impurities, and (iv) rinsing with boiling H_2O .

The decal transfer process consisted of hot-pressing the 1 cm² catalyst-coated PTFE sheets onto the polymer electrolyte membrane (Nafion 115). The membrane electrode assembly (MEA) was then placed between two metal plates. The metal plates were compressed with 15 in·lbf of a torque and heated to 146 °C for 6 min. The MEA was then sandwiched between commercially-available gas diffusion Toray paper and assemble in a 1 cm² cell. Gas diffusion media were wet-proofed in house using polytetrafluoroethylene (PTFE) [27]. 60 wt % PTFE solution was applied to both sides if the carbon paper by painting up to 30 wt % of the Toray paper. All catalyst loadings are referenced to the geometric area of the MEAs labeled as (mgpt/cm²). The 1 cm² MEA was placed between a Toray gas diffusion layer, bipolar plates and current collectors. This testing unit was secured to both sides of the MEA, using bolts and nuts.

Gas flow controllers were used to control the flow rates of pure hydrogen and oxygen gas at 50 and 225 mL/min, respectively. The gases were passed through a container of room temperature water before flowing into the cell. The pressure of the oxygen and hydrogen gas supplied was ~1 atm. The anode, at which hydrogen oxidation takes place, was used as the reference in the open circuit voltage measurements, and reference and counter electrodes in the cyclic voltammetry and polarization measurements. For the cyclic voltammetric measurements,

Table 2. 1. Test protocol for catalyst support cycle and metrics

Cycle	Measure OCP for 10 h. Run polarization curve and determine ECSA Hold at 1.2 V for 10 h; run polarization curve and determine ECSA; Complete for total 200 h (20 cycles) Single cell, 1 cm ²	
Total time	Continuous operation for 200 h	
Diagnostic Frequency	10 h	
Temperature	Room temperature (23 ±1)	
Relative Humidity	Anode/Cathode 100/100%	
Fuel/Oxidant	Hydrogen/Oxygen	
Metric	Frequency	Target
Open Circuit Potential	Every 10 h	≤10% rated OCP degradation
ECSA/Cyclic Voltammetry	Every 10 h	≤40% loss of initial area

the cathode was purged with nitrogen for 20 min to remove the oxygen. The cycles started from the OCV and scans were recorded at 5 mV/sec.

2.5.1 Test Conditions for Carbon Support Stability (Chapter 6)

Accelerated degradation testing protocols for fuel cell materials have been recommended by DOE. The testing protocols and performance metrics used in this work are given in Table 2.1.

The testing began with a measurement of the OCV for 10 h. Then, cyclic voltammetric i-E curves of the cathode were recorded to determine the electrochemically active surface area (ECSA) of the Pt. The ECSA was determined by integrating the hydrogen desorption current form between 0.2 V to 0.5 V and assuming full monolayer coverage of hydrogen to be 0.21

mC/cm² [17]. After this, polarization curves (i-V curves) were recorded for the fuel cell by stepping the current from zero to the maximum test current density. After these measurements, anodic polarization at 1.2 V vs. the anode (RHE) was applied to cathode for 10-h at room temperature. After anodic polarization, ECSA and I-V curves were obtained again. And these cycles was completed to 200 h.

2.5.2 Morphological characterization of MEA (Chapter 6)

After the accelerated degradation testing, the MEA was sliced into 1 mm-thick sections and examined by SEM. The sample morphology was probed by field-emission scanning electron microscopy (JSM-6400F, JEOL, Ltd., Tokyo, Japan) using a 10 kV accelerating voltage and a working distance of 15 mm.

References

- 1. Handbook of industrial diamonds and diamond films By Mark Antonio Prelas, Galina Popovici, Louis K. Bigelow. Marcel Deker Inc. Newyork 1998.
- 2. Schwartz, R. and Robbins, H. J. Electrochem. Soc., 123, 1903, 1976.
- 3. Schreurs, J., and Barendrecht, E., Recl. Trav. Chim. Pays-Bas, 193, 205, 1984.
- 4. Hu, I.; Karweik, D. H.; Kuwana, T. J. Electroanal. Chem., 188, 59-72, 1985.
- 5. Granger, M. C.; Witek, M.; Xu, J.; Wang, J.; Hupert, M.; Hanks, A.; Koppang, M. D.; Butler, J. E.; Lucazeau, G.; Mermoux, M.; Strojek, J. W.; Swain, G. M. Anal. Chem., 72, 3793-3804, 2000.
- 6. Skoog, D. A.; Holler, J. F.; Nieman, T. A. Principles of Instrumental Analysis, Fifth ed.; Harcourt Brace College Publishers: Philadelphia, 1998
- 7. Stefan, R. I. and Bairu, S. G., Anal. Chem., 75, 5394, 2003.
- 8. Perez, J., Tanaka, A. A., Gonzalez, E. R. and Ticianelli, E. A., J. Electrochem. Soc., 141, 431, 1994.
- 9. Bevers, D., Wagner, N. and Von Bradke, M., Int. J. Hydrogen Energy, Vol. 23, No. I, pp. 57-63, 1998.
- 10. U.S. DOE, Durability test Protocol for PEM Fuel Cells, 2005
- 11. Borup, R et al. Chemical Reviews, Vol. 107, No. 10 3907, 2007.
- 12. Mehta, V. and Cooper, J.S., J Power Sources, **114**, pp. 32–53, 2003.
- 13. Rice, M., Galus, Z. and Adams, R. N., J. Electroanal. Chem. Interfacial Electrochem., 143, 89, 1983.
- 14. T. Kodas and M. Hampden-Smith, The Chemistry of Metal CVD, VCH Publishers Inc., New York, NY, 1994.
- 15. Ay, A.; Swope, V. M.; Swain, G. M. J. Electrochem. Soc., 155, B1013, 2008.
- 16. http://www.basinc.com/mans/EC_epsilon/Techniques/Pulse/pulse.html
- 17. Y. Y. Shao, G. P. Yin, and Y. Z. Gao, Chin. J. Inorg. Chem., 21, 1060, 2005.

Chapter 3

The Physicochemical and Electrochemical Properties of Diamond Powders Coated with Boron Doped Ultrananocrystalline Diamond (B-UNCD)

3.1 Introduction

We recently reported on the overcoating of insulating diamond powder with a layer of boron-doped diamond [1, 2]. In this core-shell approach, either a boron-doped microcrystalline or ultrananocrystalline diamond layer was deposited on 8–12 μ m, 500 nm, 100 nm or 3-6 nm diam. diamond powder particles using microwave CVD and a conventional CH₄/H₂ and Ar/CH₄/H₂ source gas mixture [3]. The electrical conductivity is controlled by the doped-diamond over layer (carrier concentration and mobility) rather than by some adventitious nondiamond sp² carbon impurity phase. Coating the large diameter diamond powder was the first step in our development of a high-surface-area, electrically conducting form of diamond. We gradually progressed toward coating smaller diameter (i. e. higher surface area powder). The ultimate targets for an electrocatalyst support are a specific surface area \geq 100 m²/g and electrical conductivity \sim 1 S/cm. In our earlier work, the specific surface area and electrical conductivity of the doped diamond powder were below these targets: 2 m²/g and 0.4 S/cm [1].

In this chapter, the preparation of high specific surface area (\sim 170 m²/g) and electrically conducting (\sim 0.6 S/cm) diamond powder is described. The powders were prepared by coating 500, 100 and 3-6 nm diam. particles with a layer of boron-doped ultrananocrystalline diamond. The ultrananocrystalline diamond was deposited from an Ar-rich source gas mixture consisting of 1% CH₄, 5% H₂, and 94% Ar with B₂H₆ used for boron doping. Smooth, nanograined

diamond is formed in these Ar-rich mixtures because of a high rate of renucleation that is achieved by virtue of the gas-phase composition and conditions. Because of the high renucleation rate, ultrananocrystalline diamond is a more practical coating for substrate powders than is diamond deposited from H₂-rich CH₄/H₂ source gas mixtures. The powders were characterized before and after UNCD overcoating by scanning electron microscopy (SEM), high resolution transmission electron microscopy (HRTEM), Raman spectroscopy, and Brunauer-Emmett-Teller (BET) surface area and electrical conductivity measurements. Additionally, the electrochemical properties of the powders were evaluated using $Fe(CN)_6^{-3/-4}$, $IrCl_6^{-2/-3}$, and $Fe^{+3/+2}$ as redox probes by mounting the powders in a pipette electrode [4]. Finally, the microstructural stability and corrosion resistance of the conductive diamond powder was evaluated during anodic polarization at 1.4 V vs. Ag/AgCl in 0.5 M $_2SO_4$ for 1.5 h at 80 $^{\circ}C$. This is an accepted accelerated degradation test conditions for carbon materials. This potential was selected because such values can be experienced in fuel cell stacks during start-up under H₂starved conditions [5, 8]. Carbon corrosion (gasification) can occur under this condition that is significant enough to produce lost catalyst activity and increased ohmic resistance. For comparison, 3-4 µm diam. glassy carbon (GC) powder was also tested. The powders were evaluated by cyclic voltammetry and SEM before and after anodic polarization.

3.2 Mechanism of Ultrananocrystalline Diamond Growth

Synthetic diamond can be grown via chemical vapor deposition (CVD) and made electrically conductive by doping with boron. High-quality microcrystalline, nanocrystalline and ultrananocrystalline diamond (UNCD) can be produced by CVD methods. These include

microwave, hot-filament, or DC discharge. All involve the dissociation of source gases to produce reactive radicals.

The boron-doped UNCD overlayer was grown on insulating diamond powders by microwave plasma-assisted chemical vapor deposition (PACVD). In PACVD, microwave energy is coupled into a deposition chamber, causing the source gas components to dissociate into reactive species (radicals). Both microcrystalline (grain size ~1-3 µm) and ultrananocrystalline (grain size ~3-5 nm) diamond can be grown via PACVD by selection of the appropriate source gas composition, pressure, and microwave power.

The selection of deposition conditions was based on results in the literature. According to various papers, suitable gas mixtures used for UNCD deposition are composed of CH₄, as a carbon precursor, highly diluted in argon [3]. A small amount of H₂ may be added in the source gases in order to maintain stable plasma at relatively high microwave power [9, 10]. A low level of H₂ gas (0-5%) is used for UNCD deposition, and strongly affects structural properties including surface morphology, film roughness, and grain size [9, 11] Atomic hydrogen is thought to play a number of roles including abstraction reactions, termination of dangling carbon bonds, and gasification of nondiamond sp² carbon at the growth surface [12-14]. Reducing the concentration of hydrogen while continually increasing the hydrocarbon content of the plasma normally causes the growth of UNCD [15, 16] UNCD is the nanocrystalline diamond formed from the Ar-rich mixtures. Nanocrystalline diamonds all other nanograined materials that formed in the high ratio of CH₄.In methane-hydrogen plasmas, noble gas addition has a profound effect on the chemical characterization of the plasma, including additional ionization and dissociation of source gases. [17]

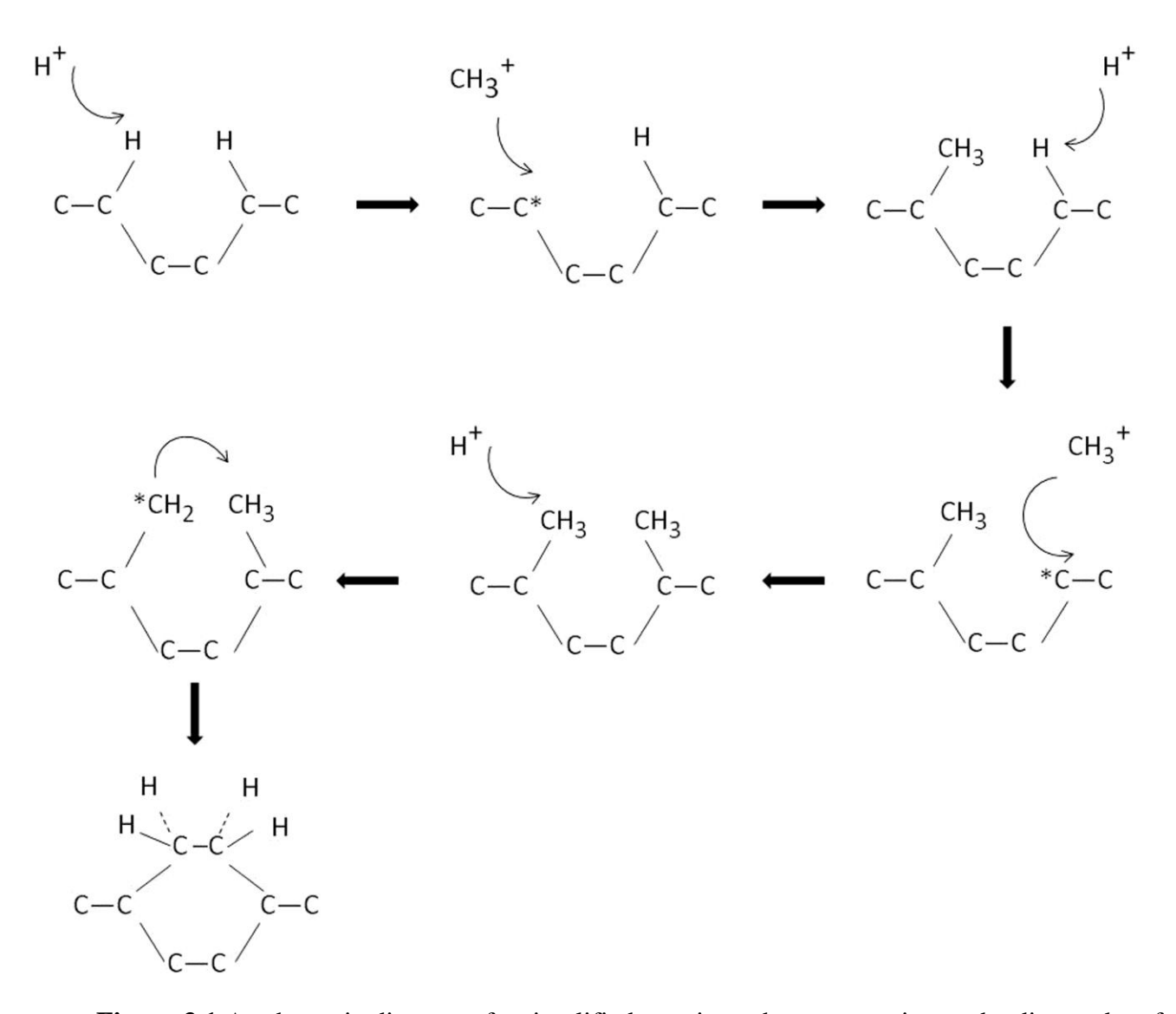


Figure 3.1 A schematic diagram of a simplified reaction scheme occurring at the diamond surface leading to stepwise addition of CHx species and diamond growth, via a sequence of H atom abstraction reactions [20].

Previously, it was suggested [18] that, for UNCD growth, the C₂ radical was playing a central role. In particular, it was proposed that C₂ could directly insert into the growing diamond lattice, with little or no energy barrier. However, recent studies have doubt on the reality of this C₂ mechanism [19-21]. The in early study about C₂ mechanism it was reported [22] that UNCD could be grown in completely hydrogen-free gas chemistry, however; now it is generally agreed that for UNCD deposition to occur, hydrogen atoms must be present in the gas mixture in small amounts. With little hydrogen gas either from addition or dissociation of CH₄, graphite structure is formed. As the hydrogen gas ratio increase, better quality diamond from (nanocrystalline or microcrystalline) are formed [23-25].

The model for diamond growth [27] described in Figure 3.1. Diamond growth can be considered to be a stepwise addition of carbon atoms to the existing diamond lattice catalyzed by the presence of excess atomic H. The atomic H formed in the plasma abstracts a surface H to form H₂, leaving behind a dangling bond for reaction. A gas phase CHx radical can collide and react with the dangling bond. This process of H abstraction and methyl addition may then occur on other site adjacent on the surface. A further H abstraction process on one of the chemisorbed groups creates a radical, which attacks the other nearby carbon group to form the ring structure and to lock the two carbons into the diamond lattice.

It proposes that UNCD is simply an extension of mechanism down to lower crystallite sizes. It is suggested that the ratio of [H]:[CHx] close to the substrate decreases below about 2, the crystallite size (<d>) is predicted to drop below 10 nm. However, this ratio should be balance accordingly to minimize formation of amorphous carbon. It is believed that the required [H]:[CHx] ratio is obtained due to the unique conditions prevailing in these higher pressure Ar-

rich gas mixtures. When the bulk of the gas in the plasma has high ratio of Ar, the collisions between CHx and inert Ar do not result in any reactions, and so these reactive CHx species can survive long enough to strike the surface, whereupon they may contribute to diamond growth. The combination of growth by CH₃ and growth from a significant fraction of the other CHx species, leads to the surface to continually renucleate (or more accurately, restructure) during growth, resulting in very small grain sizes [26-28]

3.3 Results

3.3.1 Diamond powder morphology and microstructure

The morphology of the powder before and after B-UNCD deposition was investigated by SEM. Figure 3.2A shows an SEM image of 500 nm diam. powder prior to deposition. The uncoated powder particles are irregularly shaped with sharp, jagged edges. The facet surfaces, however, are relatively smooth. After deposition, the seed particles were covered by a diamond overlayer possessing a nodular morphology, as seen in Fig. 3.2B. The jagged edges are no longer present because of this overlayer. The nodular morphology is characteristic of diamond grown from Ar-rich source gas mixtures and results from the high rate of renucleation during growth [29-31]. In other words, new nucleation events frequently happen that limit any one of the nuclei from growing into a large crystal. It appears in the image that much of the diamond powder surface has been covered with the doped UNCD overlayer. Particle—particle fusion, an inevitable occurrence with this approach, is evident in the three coalesced particles in the upper part of the image. This coalescence reduces the specific surface area but likely improves the electrical conductivity through increases in the carrier mobility.

It is more difficult to resolve morphological changes of the UNCD coated on the smaller 100 nm diam. powders. Images of the powder before and after coating are presented in Fig. 3.2C

and 3.2D. After coating, there is a considerable increase in the size of most of the seed particles with significant size variability. Based on the variable particle size, there are undoubtedly some regions where the rate of diamond growth is higher than others. Additionally, the larger particles also result from extensive particle–particle fusion. In fact, particle coalescence appeared more prominent for the 100 nm than for the 500 nm diam. powder. This caused a reduction in the specific surface area from 53 to 26 m²/g (Table 3.1). A challenge with preparing conducting diamond powder via this core-shell approach is the balance between the growth time and conditions needed to achieve a near complete coating of individual particles with the avoidance of significant particle fusion.

Raman spectroscopy was used to evaluate the microstructure of the uncoated and coated powders. Figure 3.3 shows typical Raman spectra for a 100 nm diam diamond powder sample before and after B-UNCD deposition. The spectrum for the coated 500 nm diam. diamond powder had similar spectral features. The spectrum for the uncoated diamond powder consists of a single peak at 1332 cm⁻¹ with a full width at half maximum (fwhm) of 12 cm⁻¹ [32-34]. This is the first-order phonon mode for cubic diamond. There is little photoluminescence background and little scattering in the 1500–1600 cm⁻¹ region that is characteristic of sp² and mixed sp²/sp³-bonded carbon impurity. The fwhm is inversely related to the phonon lifetime [34]. The relatively narrow linewidth for the powder compares favorably with that seen for a diamond standard and indicates that the powder particles are relatively defect-free.

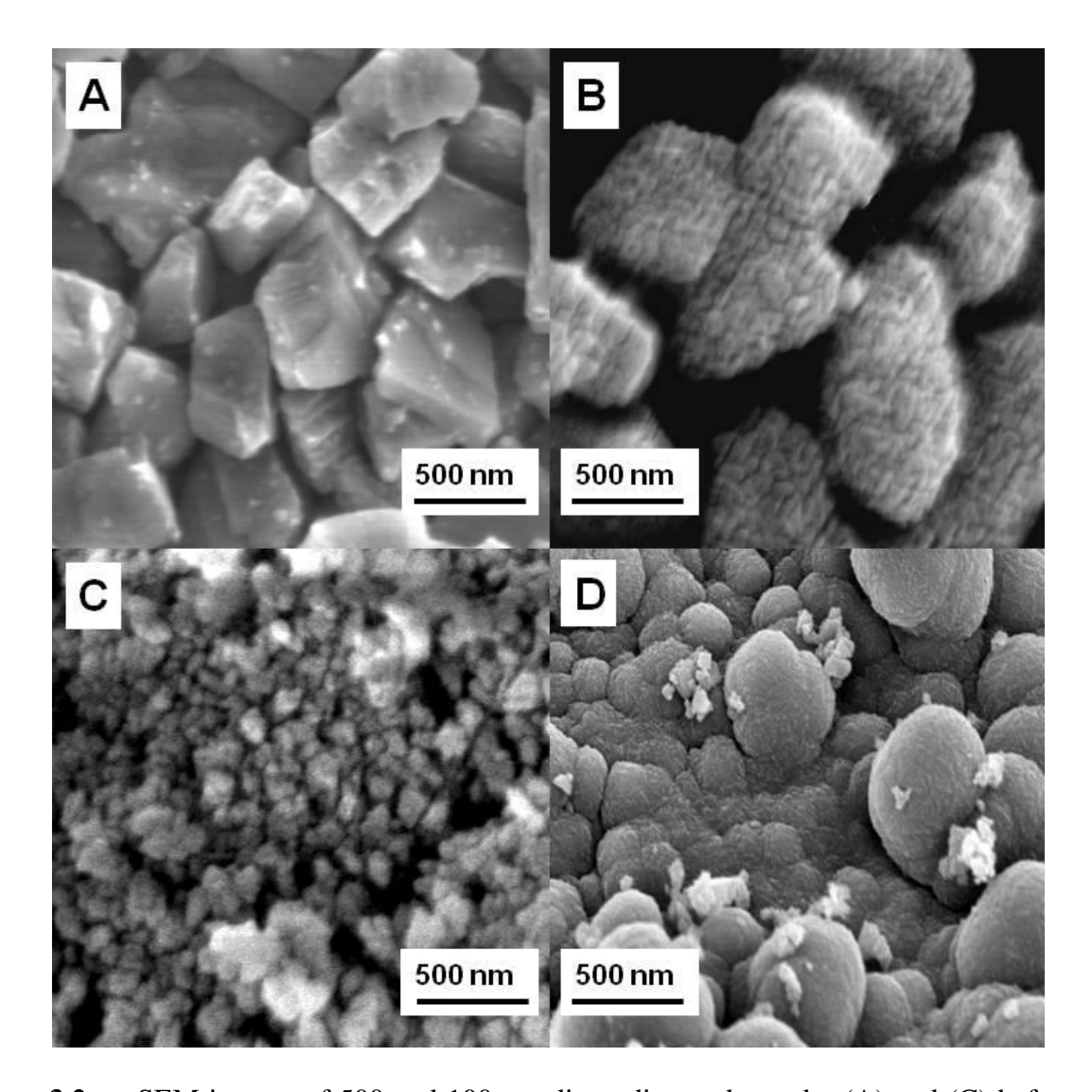


Figure 3.2 SEM images of 500 and 100 nm diam. diamond powder (A) and (C) before, and (B) and (D) after deposition of a boron-doped UNCD for 2 h.

The spectrum for the coated powder is identical to that for UNCD films deposited from Ar-rich source gas mixtures [35-40]. In addition to the diamond peak at 1332 cm⁻¹, which is largely buried within more intense scattering in this region, the spectrum has 4 additional peaks at 1150, 1350, 1450, and 1550 cm⁻¹. UNCD grown from Ar-rich source gas mixtures is characterized by 50–100 nm nodules consisting of individual diamond grains (~15 nm)

connected to one another sp²-bonded carbon at the grain boundaries. Based on HRTEM images, the grain boundatries are 2-4 atom wide. The high fraction of grain boundary gives rise to a relatively large number of sp²-bonded carbon scattering centers [41-43]. The Raman scattering cross section for this carbon is 50x larger than that for diamond, so the spectrum is dominated by the grain boundary carbon [38-43] The one phonon diamond line at 1333 cm⁻¹ decreased in intensity and significantly broadened from 12 to 140 cm⁻¹ as the film changed from a microcrystalline (0.5% CH₄) to a nanocrystalline (1% CH₄) morphology.

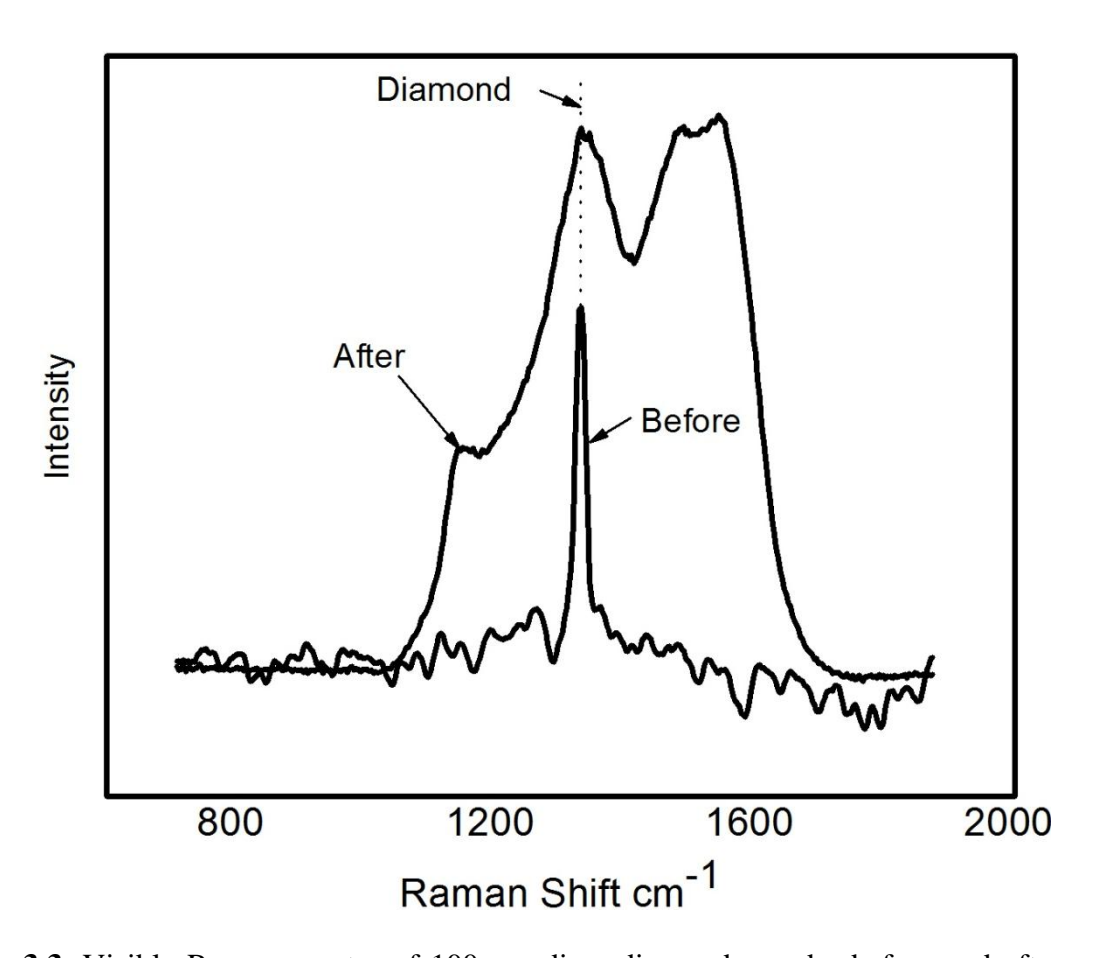


Figure 3.3. Visible Raman spectra of 100 nm diam diamond powder before and after coating with a layer of boron-doped nanocrystalline diamond.

The high grain boundary density in this film reduces the phonon lifetime, and this is manifested in an increased linewidth. Relative to the diamond line, the intensities of the 1150, 1470, 1550, and 1590 cm⁻¹ peaks increased significantly for the nanocrystalline film. The peak at 1150 cm⁻¹ is much more pronounced and it occurs in tandem with the 1470 cm⁻¹ peak. The peaks at 1550 and 1590 cm⁻¹ arise from the nondiamond sp²-bonded carbon atoms in the grain boundaries. The origin of the 1150 and 1470 cm⁻¹ peaks has been the subject of some discussion in the literature. The 1150 cm^{-1} peak is often used as a diagnostic feature of nanocrystalline sp³bonded diamond mainly because of its presence in the spectrum. This assignment is based on the fact that this peak is near a maximum in the vibrational density of states at ca. 1200 cm⁻¹. It is generally observed that the 1150 and 1470 cm⁻¹ peaks occur in tandem, with the 1470 cm⁻¹ peak being more intense. The most seminal work understanding the origin of these two peaks has come from Ferrari and Robertson, who concluded that the scattering at these two frequencies is not due to C-C sp³ vibrations but rather to scattering from trans-polyacetylene oligomers (C-C sp² vibrations) of different conjugation lengths in the grain boundaries [38]. These oligomers have a mixture of sp² and sp³ bonding and differ in length depending on the film quality. These vibrational modes are connected to the presence of hydrogen as postgrowth annealing in a vacuum (desorption of hydrogen) causes the vibrational modes to disappear. Assignment of these two peaks to C–C sp^2 rather than C–C sp^3 vibrations is based on the following observations: (i) the peak intensities decreased with increasing excitation energy, which is exactly the opposite of what is expected for an sp^3 phase, (ii) no peaks at 1150 or 1470 cm⁻¹ were seen for nanocrystalline diamond powders produced by detonation techniques, and (*iii*) no peak near 1150 cm⁻¹ was seen in tetrahedral amorphous carbon films (ta-C) deposited with 80–90% sp³ carbon, as the scattering from the 10–20% sp² carbon overshadows that from the sp³ phase with visible excitation [34-43].

3.3.2 Specific surface area and electrical conductivity measurements

The specific surface area of the powders was determined by the BET method before and after layer coating with boron-doped diamond. As shown in Table 3.1, the specific surface area of the 3-6 nm diamond powder decreased from a nominal value of 260 to 170 m²/g after diamond coating. This is due to diamond growth over not individual particles but multiple neighboring particles effectively fusing them together. After coating, the 100 nm doped diamond powder had a specific surface area of 27 m²/g. The specific surface area of both powders decreased by ca. 50% after diamond coating due mainly to particle–particle fusion and multiple particle overgrowth. This is consistent with the SEM image shown in Fig. 3.2, which revealed extensive particle–particle fusion and a corresponding increase in the particle size. HRTEM measurements revealed 40-100 nm clusters of diamond particles after deposition. 3-6 nm diam. diamond powders well aggregate due to high surface energy [44]. Specific surface areas of other powders are also shown in Table 3.1, for comparison. For example, the coated 500 nm diam. diamond

powder had a nominal value of 8 m 2 /g, The GC powder had a nominal value of 1–2 m 2 /g, and Vulcan XC-72 carbon powder had a value of 250 m 2 /g.

Table 3.1 Electrical conductivity and specific surface area of the uncoated, B-UNCD coated diamond, and sp²-bonded carbon powders before and after acid washing. Values shown are means +/- standard deviations

Powder Sample	Conductivity (S/cm)	BET (m ² g)
3-6 nm powder uncoated and acid	0	260
3-6 nm powder coated ones	0.43 ± 0.03	N/A
3-6 nm powder coated twice	0.77 ± 0.05	170
3-6 nm powder coated and acid washed	0.65 ± 0.07	N/A
100 nm powder uncoated and acid	0	52.6±0.3
100 nm powder coated	0.47 ± 0.14	26.5±0.2
100 nm powder coated and acid	0.41 ± 0.02	N/A
500 nm powder coated	0.59 ± 0.05	8.0 ± 0.4
500 nm powder coated and acid	0.45 ± 0.04	N/A
Glassy Carbon	1.41 ± 0.24	1-2
Vulcan XC-72	1.87±0.19	250

Table 3.2 Cyclic voltammetric peak potential separation (ΔE_p) and peak current ratio ($i_p^{forward}/i_p^{reverse}$) for various redox analysis at 500 nm and 100 nm doped diamond powder, and glassy carbon powder electrodes.

Analyte	Electrode	$\Delta \mathbf{E_p}$	i _p forward reverse
$Fe(CN)_6^{-3/-4}$	500 nm	76 ± 6	0.99
	100 nm	120 ± 14	0.95
	GC	76 ± 4	1.00
$IrCl_{6}^{-2/-3}$	500 nm	81 ± 4	0.99
	100 nm	98 ± 8	1.00
	GC	67 ± 2	1.00
$Fe^{+3/+2}$	500 nm acid washed	221 ± 30	0.97
	500 nm rehydrogenated	560 ± 28	0.92
	GC	121 ± 89	0.98

In order to verify that a conductive layer formed over the diamond particles, electrical resistance measurements were made on the dry powder and the calculated conductivities are presented in Table 3.1. The uncoated diamond powder had no measurable conductivity after it has been cleaned by acid washing. This is an important point to mention. As-received detonation nanodiamond powder often possesses some electrical conductivity, but this conductivity arises because of sp² carbon impurity phases on the surface. Anything chemically or electrochemically that alters the structure of this impurity phase (e.g., acid washing) will necessarily decrease the electrical conductivity.

In contrast, the electrical conductivity of the diamond-coated powder arises from a distinctly different mechanism; the carrier concentration and carrier mobility within the doped diamond overlayer. After a 2 h B-UNCD overcoating, the conductivity of the 500 and 100 nm diam. powders increased to nominal values of 0.59 and 0.41 S/cm, respectively. Importantly, the conductivity was not significantly altered after acid washing, consistent with a chemically stable, doped diamond overlayer. Furthermore, this result proved that adventitious nondiamond sp² carbon impurity that might form on the diamond surface during deposition does not contribute to the electrical properties; as such impurity phase would be expected to be removed by the acid treatment.

The 3-6 nm diam. diamond powder was coated twice using a 2-h growth period with powder mixing in between to increase the number of particles coated and the coverage over each particle. After the 2nd coating, the conductivity increased almost 100 %. The electrical conductivity measurements are the most definitive data for the existence of a doped diamond

overlayer. For comparison, the nominal conductivities of the GC and Vulcan XC-72 powders were slightly higher at 1.4 and 1.9 S/cm, respectively.

3.3.3 Background cyclic voltammetric current density–potential curves

Background cyclic voltammetric i-E curves provide insight on the physicochemical properties of conductive diamond powders. The potential limits, voltammetric features, and the magnitude of the background current are all sensitive to the microstructure of the carbon phase on the surface, the surface chemistry and the electronic properties. Figure 3.4 shows typical curves in 1 M KCl for the 500 and 100 nm diam, doped diamond powder. The currents are normalized to the electrode area geometer. We tried to ensure maximum wetting of the powder by extended potential cycling between -0.5 and 1.2 V. During the cycling, the diamond powder surface becomes more hydrophilic due to the incorporation of surface carbon-oxygen functionalities. As a consequence, more of the powder surface slowly wets with the supporting electrolyte solution. All measurements with the powders were not begun until the background voltammetric current reached a constant level. These stabilized curves were obtained after a few cycles and remained unchanged with additional cycling. This is consistent with a constant wetted area during the measurements. Due to its electrically insulating nature, the curve for the uncoated diamond powder exhibited zero current at all potentials (dotted line). The background current for the 500 nm powder is lower than that for the 100 nm diamond powder due to a reduced surface area exposed to the solution. This result because of the lower specific surface area of the 500 nm diam. powder and the greater mass of the 100 nm diam. powder used to prepare the pipette electrode. The background current for the 500 nm powder electrode is low and featureless between -300 and 800 mV. At the anodic limit, chlorine is presumably generated from the oxidation of chloride. The origin of the cathodic current, which begins to flow at -0.3 V, is

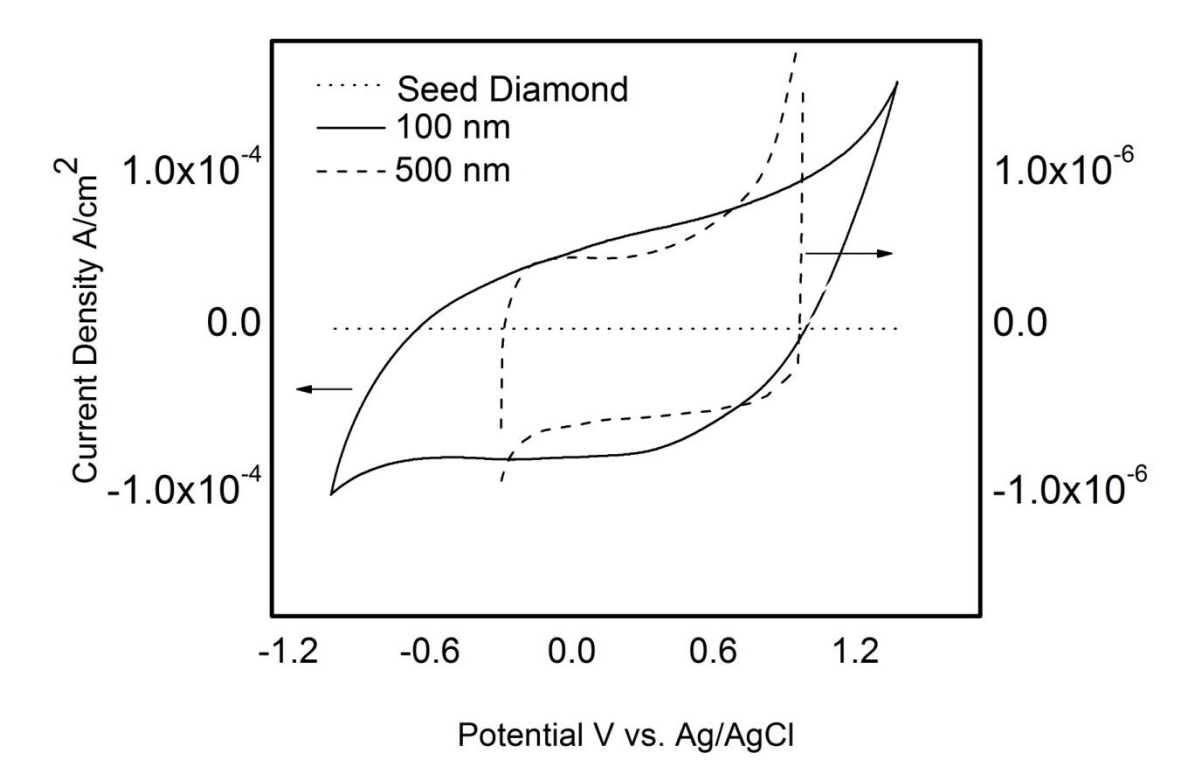


Figure 3.4 Background cyclic voltammetric i-E curves for acid-washed 500 and 100 nm diam. B-UNCD-coated powders recorded using the pipette electrode. A comparison curve for the insulating diamond powder ((prior to nanocrystalline diamond deposition) is also shown. The curves were recorded in 1 M KCl at 50 mV/s. The currents are normalized to the area of the electrode contacting the supporting electrolyte solution.

unknown. This current does not appear to be associated with the reduction of dissolved O_2 , as it is still present in the voltammograms after solution purging with N_2 . The apparent potential window for the 100 nm powder is wider than that for the 500 nm powder electrode, particularly at negative potentials, as some cathodic current begins to flow at -0.6 V that is due to an unknown reaction. The wider potential window is due, at least to some extent, to ohmic resistance within the powder network. This is discussed further below. Evidence for this is the shift slope of the i-E curve relative to the zero current line. The electrochemical characterization of the coated 3-6nm diam. diamond powder is discussed in Chapter 5.

3.3.4 Cyclic voltammetric response for different redox systems

Figure 3.5 shows a series of cyclic voltammetric i-E curves for $Fe(CN)_6^{-3/-4}$ and $IrCl_6^{-2/-3}$ at pipette electrodes prepared with coated diamond and GC powders. The currents are normalized to the geometric area of the electrode (0.002 cm²). The $Fe(CN)_6^{3-/4-}$ redox couple does not undergo simple electron transfer at carbon electrodes as is commonly thought [45-50]. The heterogeneous electron-transfer rate constant is strongly influenced by the electrode surface cleanliness, electrolyte type, and concentration, as well as the electrode's density of electronic states near the formal potential of the couple. The rate constant is relatively insensitive to the surface oxygen functionalities on sp² carbon electrodes as long as a thick oxide film is not present [46-48]; however, it is very sensitive to the presence of surface oxygen on diamond electrodes [49, 50]. The heterogeneous electron-transfer rate constant for $IrCl_6^{2-/3-}$ is relatively insensitive to the surface microstructure, surface oxides, and adsorbed monolayers on sp² carbon electrodes [46-48]. It is primarily influenced by the electrode's (both sp² and sp³ carbon) density of electronic states near the formal potential [29-31, 46-48]. This redox system was chosen to probe the electronic structure of the powder electrode, which is related to density of charge carriers and their mobility. The boron-doping level and homogeneity are very important determinants of fast charge transfer kinetics. In Figure 3.5A and B, curves are shown for these two redox systems at 500 nm doped diamond powder electrodes. Well defined, peak-shape voltammograms are seen for both redox systems at all the scan rates. At the lowest scan rate, 30 mV/s, the nominal ΔE_p values were 76 and 81 mV, respectively (see ΔE_p Table 3.2). The oxidation peak current for $Fe(CN)_6^{-4}$ and the reduction peak current for $IrCl_6^{-2}$ varied linearly

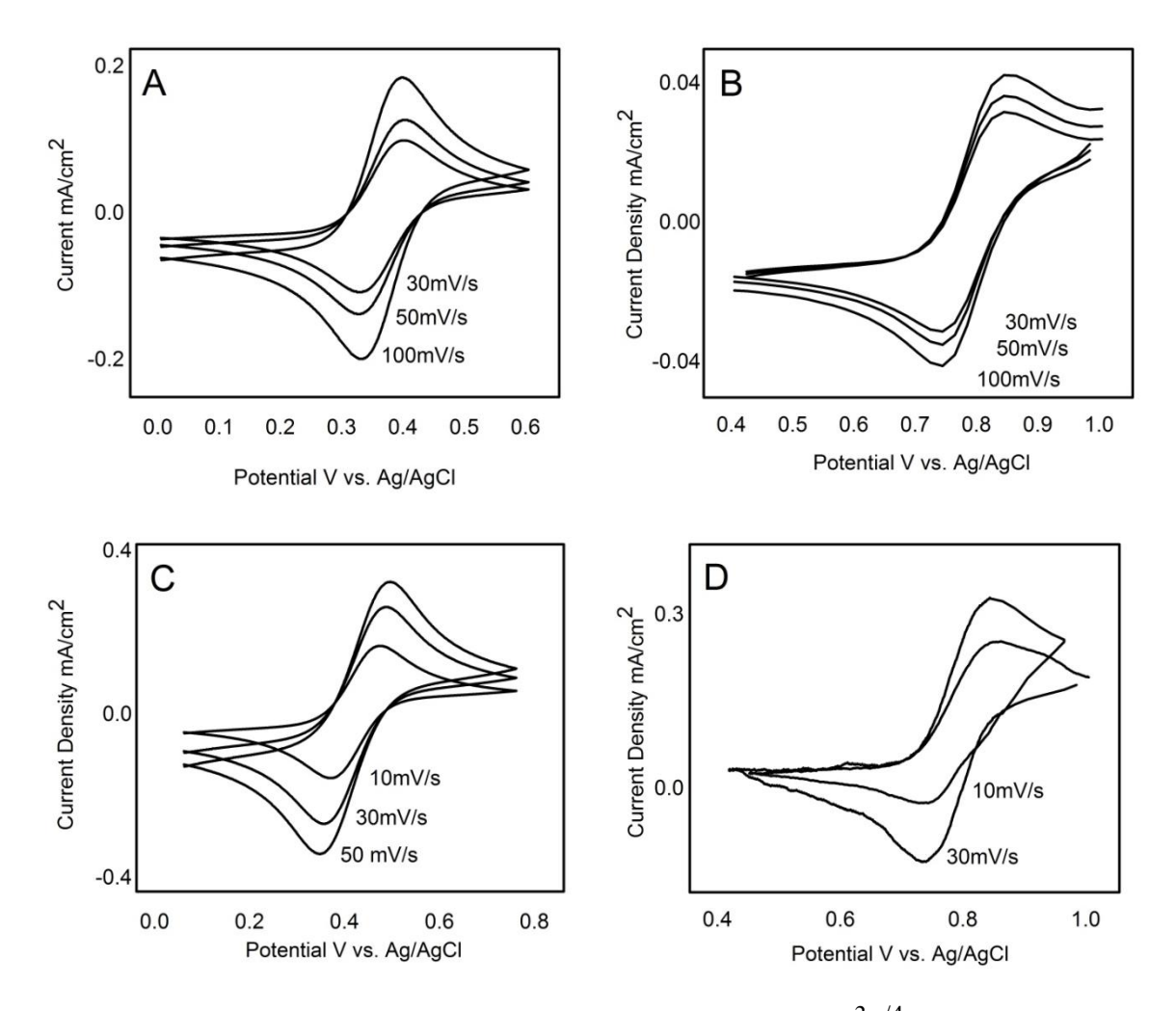


Figure 3.5 Cyclic voltammetric i-E curves for 1 mM Fe(CN) $_6^{3-/4-}$ in 1 M KCl at (A) 500 nm and (C) 100 nm diam. B-UNCD-coated diamond powder electrodes. Cyclic voltammetric i-E curves for 1 mM IrCl $_6^{2-/3-}$ in 1 M KCl at (B) 500 nm diam. B-UNCD-coated diamond powder and (D) 100 nm B-UNCD-coated diamond powder electrodes. The curves were recorded using the pipette electrode, and the currents are normalized to the geometric area of the electrode, 0.002 cm^2 .

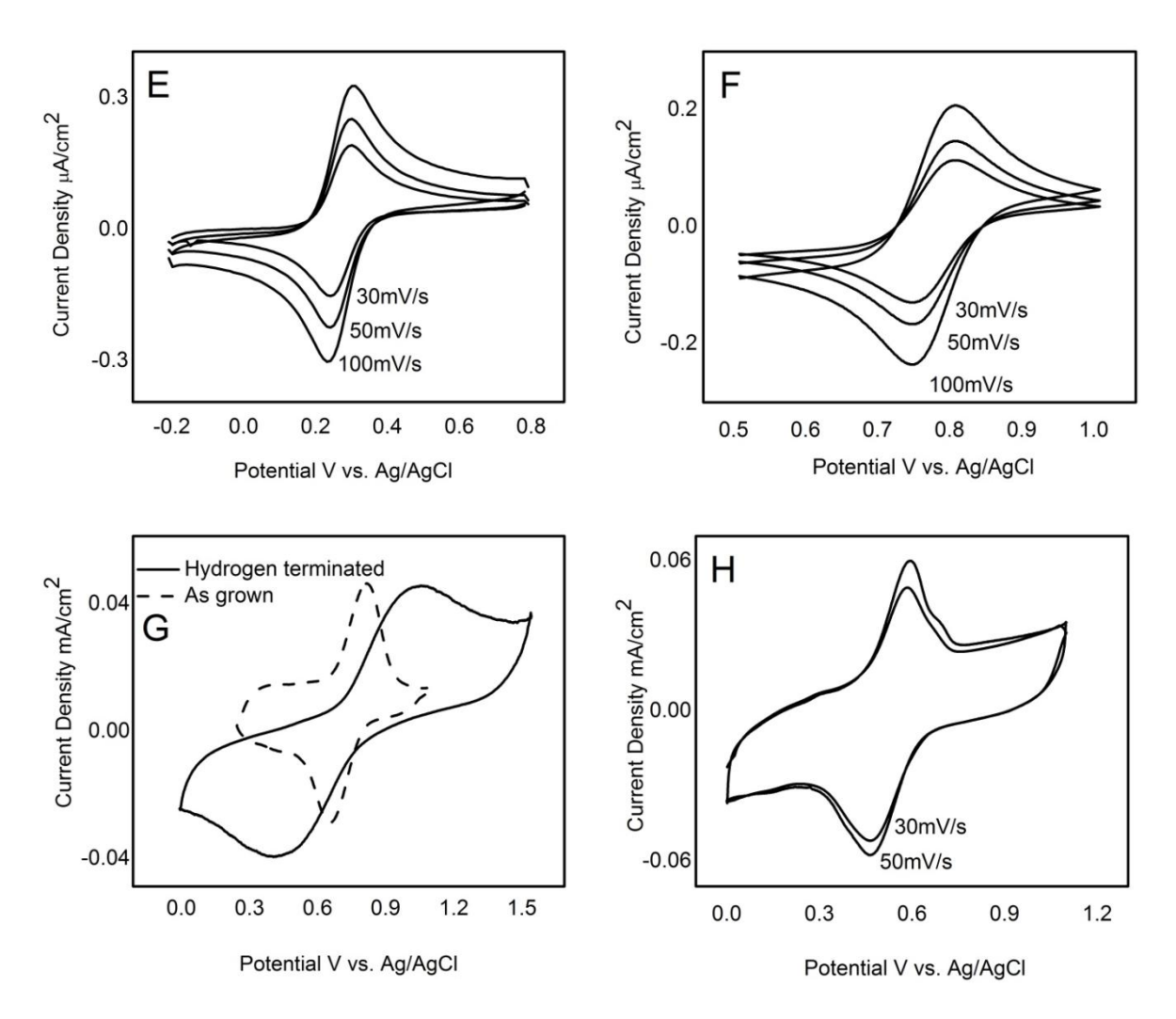


Figure 3.5 Continue. Cyclic voltammetric i-E curves at GC powder electrodes for (E) for 1 mM $Fe(CN)_6^{3-/4-}$ in 1 M KCl and (F) for 1 mM $IrCl_6^{2-/3-}$ in 1 M KCl. Cyclic voltammetric i-E curves for 1 mM $Fe^{3+/2+}$ in 1 M HClO₄ at (G) 500 nm diam. B-UNCD-coated diamond powder and (H) GC powder electrodes. The curves were recorded using the pipette electrode, and the currents are normalized to the geometric area of the electrode, 0.002 cm^2 .

with (scan rate) $^{1/2}$ from 10 to 300 mV/s ($r^2 > 0.98$), indicative of reaction rate limited by semiinfinite linear diffusion of the reactant.

In Fig. 3.5 C and D, curves are shown for the two redox systems at the 100 nm doped diamond powder. Well-defined, peak-shaped voltammograms are also seen for both at the different scan rates. At the lowest scan rate, 30 mV/s, the nominal ΔE_p values were 120 and 98 mV, respectively, for $Fe(CN)_6^{-3/-4}$ and $IrCl_6^{-2/-3}$. These same redox systems were tested at a GC powder electrode. Nominal ΔE_p values of 76 and 67 mV were observed at 30 mV/s. Clearly, the 500 nm powder exhibits electrochemical activity similar to that of the GC powder. Furthermore, the electrochemical activity for these two redox systems is similar to that seen for thin films of B-UNCD.[39, 51, 52] Larger peak splitting is seen for the 100 nm powder, even though the electrical conductivity of the powder is similar to that for the 500 nm powder. This apparently arises because of ohmic resistance within the powder network in the pipette electrode. In fact, measurements as a function of the concentration revealed an increasing ΔE_p with increasing concentration for both redox systems (30 mV/s) indicative if the ohmic resistance. Additional evidence for the ohmic resistance is the sloping background voltammetric i-E curve seen in Fig. 3.4. The resistance arises from the incomplete overcoating of the powder particles and their irregular shape, which reduces the particle-particle contact.

The electrode response for $Fe^{+3/+2}$ was also tested using as-received and acid washed/rehydrogenated 500 nm B-UNCD coated diamond powder to study the effect of surface chemistry on the response. The McCreery group has shown that the $Fe^{+3/+2}$ redox system is catalyzed at carbon electrodes by a specific chemical interaction with surface carbonyl

functionalities [53]. Therefore, the heterogeneous electron-transfer rate constant is highly sensitive to the presence of oxides on sp² and sp³ carbon electrodes [49, 50, 53]. The ΔE_p for the as-grown powder was nominally 221 mV. This powder consists of both sp³ and sp² carbon impurity due to the variation in temperature during deposition. It is supposed that some carbon-oxygen functionalities exist at sites within the impurity phase. After acid washing and rehydrogenation, ΔE_p increased considerably to 560 mV (50 mV/s). It was the same powder that was used to obtain the voltammograms for $Fe(CN)_6^{-3/-4}$ and $IrCl_6^{-2/-3}$ in Fig.3.5A and B. Therefore, the large increase in ΔE_p for $Fe^{+3/+2}$ is not due to ohmic resistance effects but rather to a loss in surface carbon–oxygen functionalities on the surface. The large ΔE_p for this redox system is consistent with the sluggish kinetics typically seen for this redox system at hydrogen-terminated nanocrystalline diamond thin-film electrodes [49, 50, 53].

3.3.5 Morphological and microstructural stability testing

One motivation for investigating boron-doped diamond powders is their potential use as a dimensionally-stable electrocatalyst support material. Figure 3.6 shows continuous amperometric current density—time (i-t) curves recorded for 100 and 500 nm doped diamond powders during a constant potential polarization at 1.4 V vs Ag/AgCl in 0.5 M H₂SO₄. The polarization was performed for 1 h at 80 °C. A curve for GC powder is also shown, for comparison. The current is normalized to the area contacted by the supporting electrolyte solution. The curves reveal that significantly less current density passes through the diamond powders as compared to the GC powder. The i-t profiles for the two diamond powders are relatively smooth and devoid of

temporal fluctuations. The current for the GC powder, on the other hand, is significantly greater and there are sizable temporal fluctuations seen. These fluctuations are due to dynamic increases in the surface area of the powder as the particles morphologically degrade and corrode. There is also a general increase in the current starting at about the 2400 s mark. This is consistent with an increase in the electrode area due to microstructural degradation and corrosion. Integration of the i-t curves yields the oxidation charge passed. This charge results from oxidation of the powder, which involves a combination of surface carbon–oxygen functionality formation, microstructural degredation, and corrosion (i.e., gasification of the carbon). The total charge passed was greater for the GC powder (0.4 C/cm²) than for the diamond powders (0.06 C/cm²). This is consistent with the diamond powders being less active than the GC powder toward oxidation. Several processes could contribute to the oxidation current for sp² carbon powders: intercalation and subsequent oxidation of the intercalation compound, and surface oxide formation at existing edge plane sites and at edge sites formed as a result of the lattice strain caused by the oxide formation, gas evolution, and corrosion or gasification.

Although from these electrochemical data alone, one cannot determine if any morphological or microstructural degradation of the carbon occurred. Additional electrochemical tests and SEM imaging were performed to gain more insight regarding possible degradation. For example, cyclic voltammetric i-E curves were recorded for the 500 and 100 nm B-UNCD coated diamond and GC powders in 0.5 M H₂SO₄ before and after polarization at 1.4 V. Representative curves for all three electrodes are presented in Fig. 3.7 A-C. For the 500 nm doped diamond powder, the cyclic voltammograms are largely unchanged after the polarization (Fig. 3.7A). The currents are normalized to the electrochemically active area. If the surface had been damaged by

degradation and corrosion, then an increased background current would be expected due to an increase in the surface area of the powder exposed to the solution. It is also possible that if the degradation were severe enough, then the powder particle—particle contact would be significantly compromised, leading to an increase in the electrode ohmic resistance. This would be evidenced by a sloping voltammetric i-E curve rather than one that is symmetric around the zero current line. The fact that the curves are largely unchanged is good evidence for the absence of significant structural degradation or corrosion. The diamond surface gets converted from an H-terminated one to an O-terminated one. There is, however, no microstructural change associated with oxidation of diamond, simply a change in surface chemistry. This is consistent with previous studies of the dimensional stability of diamond powders and thin films supported on Si [1-2]. The fact that the curves are unchanged indicates that there is no significant increase in the wetted area of the electrode after polarization.

There is minor change in the curve for the 100 nm B-UNCD-coated diamond powder. First, the curve prior to polarization is sloped due to some ohmic resistance within the powder network. It is supposed that this is due to limited contact between the hard, irregularly shaped particles as well as incomplete doped diamond coverage around the particles. Achieving a uniform coverage of doped diamond around the seed particles is more arduous the smaller the particle size. The upward slope of the curve actually increases some after polarization, consistent with an increase in the ohmic resistance of the powder network.. Furthermore, unlike the curve for the 500 nm diamond powder, the curve for the 100 nm powder prior to polarization is characterized by small oxidation and reduction peaks between 0 and 0.2 V. These peaks are often seen on disordered sp² carbon materials (see the GC powder data in Fig.3.7 C) and result from redox-active carbon–oxygen functional groups (e.g., hydroquinone/quinone couple) formed at

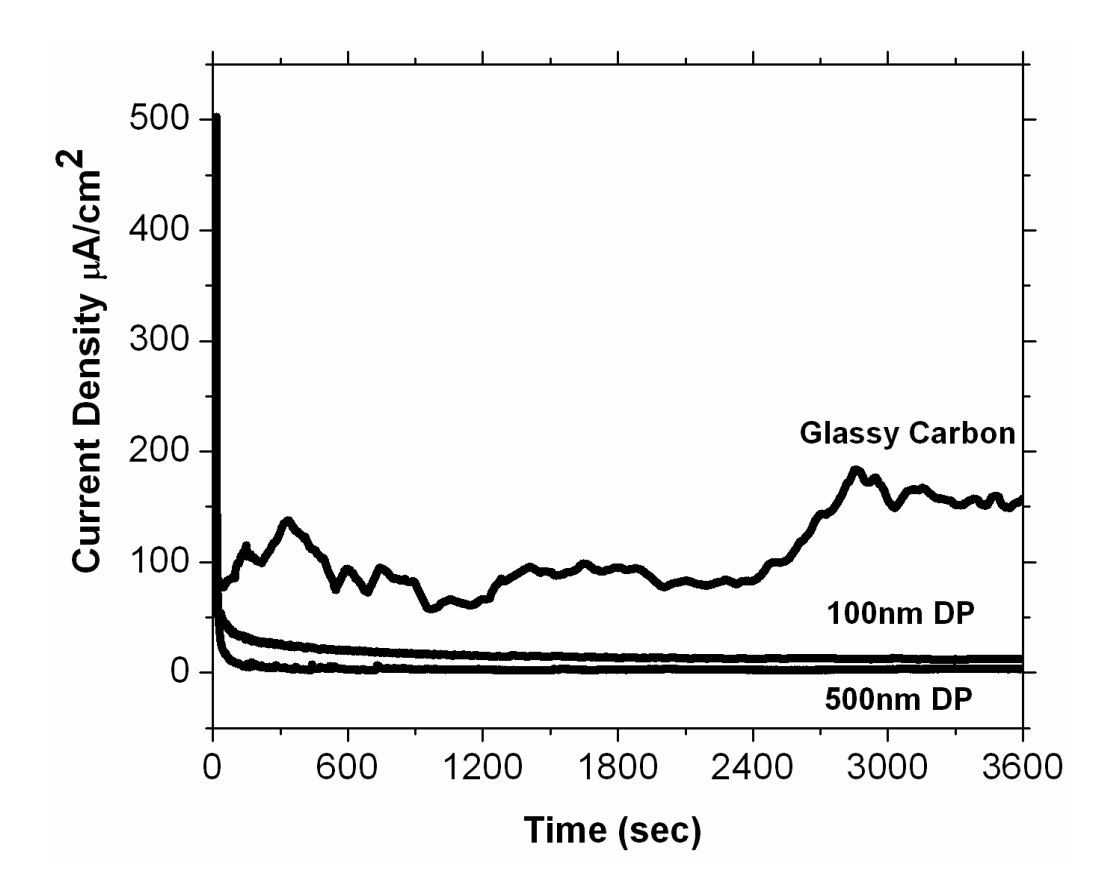
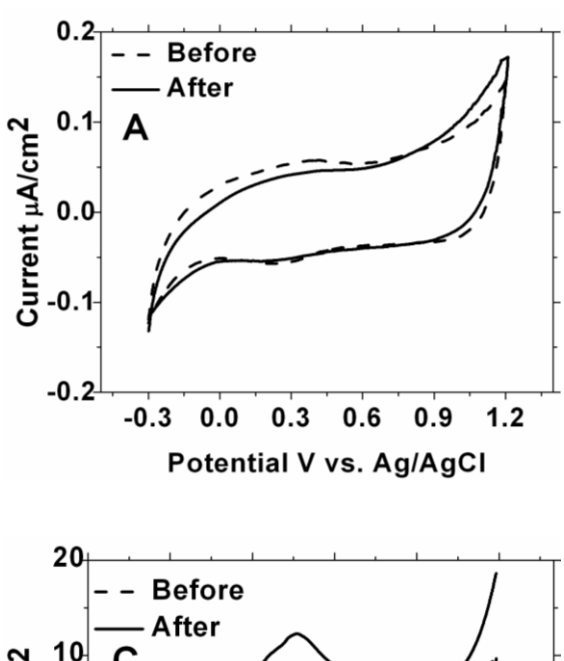
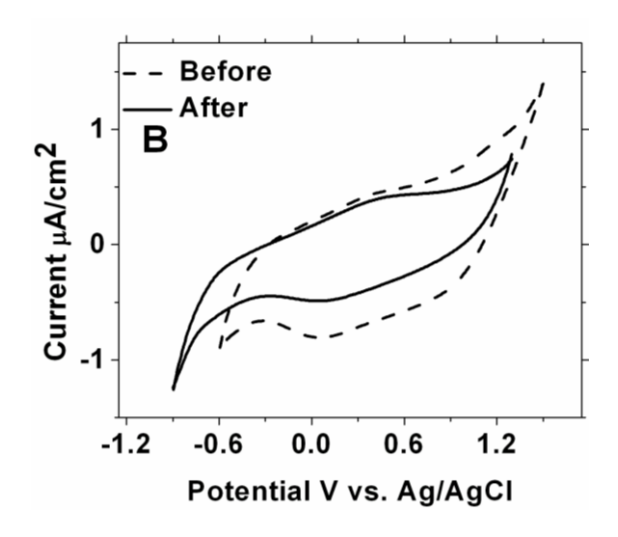


Figure 3.6 Continuous amperometric i-t curves for 500 and 100 nm diam. B-UNCD-coated diamond powders recorded at 1.4 V vs. Ag/AgCl in 0.5 M $_{2}SO_{4}$ for 1 h at 80 $_{2}CC$ C. A comparison curve for GC powder is also shown. The curves were recorded using the pipette electrode. The currents are normalized to the area of the electrode contacting the supporting electrolyte solution.

the edge plane sites [54-58]. Such redox-active functional groups are not expected for diamond and are normally not observed. Their presence here may mean that these small powder particles have some sp² carbon impurity exposed with reactive sites where these functional groups can readily form. The background current and charge slightly decrease after the polarization, and the redox peaks are still present with amplitude that is about the same as before the polarization. It is possible that the reduced background current seen is caused by the loss of some of the nondiamond carbon impurity from the diamond powder surface in the forms of CO and or CO₂ [59].





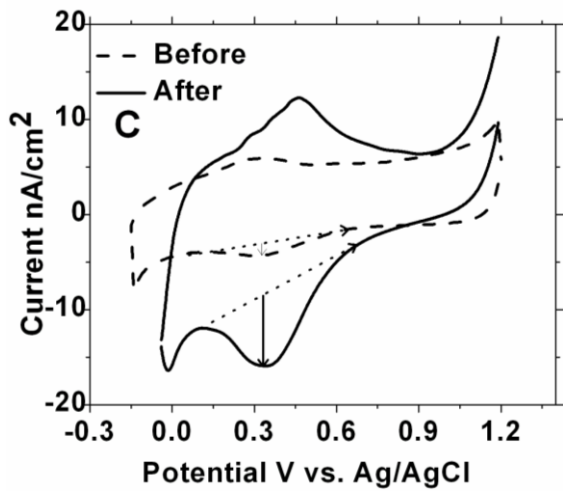


Figure 3.7 Cyclic voltammograms for (A) 500 nm, (B) 100 nm B-UNCD-caoted diamond powder and (C) glassy carbon Before (......) and after (_) anodic polarization in 0.5M H_2SO_4 for 1 h. Scan rate=20 mV/s. Temperature = 80 °C.

The cyclic voltammetric i-E curve for the GC powder was significantly altered after the anodic polarization (Fig. 3.7C). Specifically, the peak current and charge for the redox-active functional groups increased [58]. The peak positions are largely unchanged. The increased peak amplitude results from the formation of greater functional group coverage because of microstructural degradation and corrosion, processes that produce new active sites for the functional group formation. The overall background current and charge also increased after polarization, consistent with an increase in the exposed surface area due to microstructural damage.

SEM was used to confirm the presence or absence of morphological and microstructural damage to the powders. Characteristic images of the GC and 500 nm doped diamond powders, before and after polarization, are presented in Fig. 3.8 A-D. These powders were taken from the portion of the sample exposed to the electrolyte solution during the 1.4 V polarization. Prior to polarization, spherically smooth, GC particles are seen with diameters of 3–4 µm (Fig. 3.8A). After polarization, morphological and microstructural degradation is seen (Fig. 3.8B). Some particles were fractured and broken apart during the polarization, which produced a greater surface area and led to the formation of a greater number of redox-active carbon–oxygen functional

groups. Not only does the polarization degrade the powder morphology and microstructure, but if allowed to proceed long enough, it would result in significantly increased ohmic resistance through the powder network due to reduced particle connectivity. In contrast, there was no apparent change in the structure of the 500 nm doped diamond powder after polarization. Sharp, irregularly shaped crystals are apparent before and after polarization. The nominal diameters are the same, and there is no evidence for any particle roughening or pitting.

3.4 Discussion

The results demonstrate that high surface area (~170 m²/g) and electrically conducting (~1 S/cm) diamond powder can be formed by overcoating inexpensive diamond abrasive with a layer of boron-doped ultrananocrystalline diamond. In this core-shell approach, one must empirically determine the growth conditions needed to achieve maximum homogeneity in the overlayer while avoiding significant particle—particle fusion, which reduces the specific surface area. Our procedure for producing the electrically conducting diamond powder is not optimal but does enable materials to be produced for proof-of-concept investigations. New reactor designs

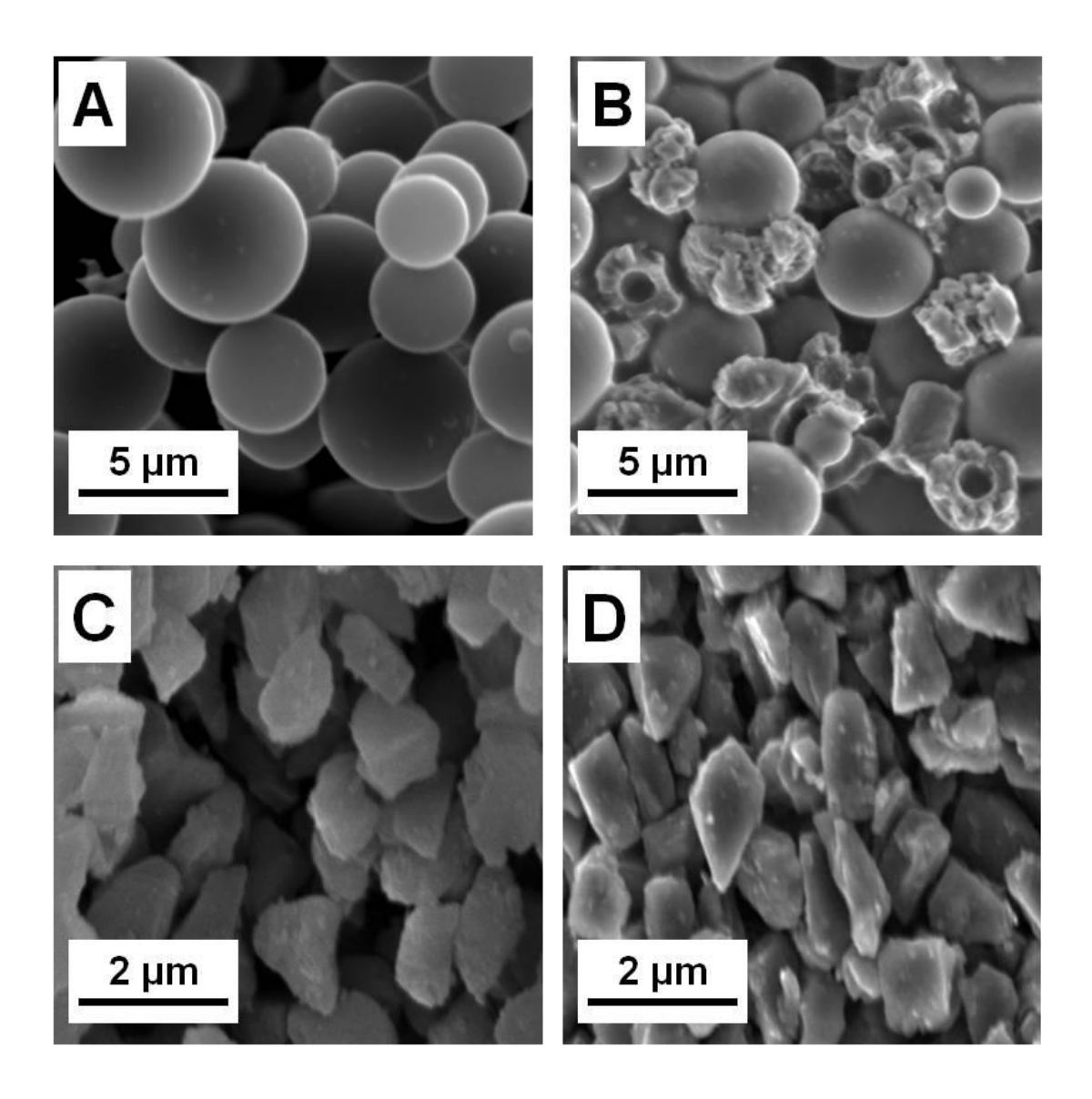


Figure 3.8 SEM images of GC powder (A) before and (B) after 1-h polarization at 1.4 V vs. Ag/AgCl in 0.5 M $_{2}$ SO₄ for at 80 $_{2}$ C. Images are also shown of 500 nm B-UNCD-coated diamond powder (C) before and (D) after the same anodic polarization. The polarization was performed using the pipette electrode.

are required for more rapid, efficient, and homogeneous diamond coatings over individual substrate particles. For instance, designs where the powders are suspended in or repeatedly get transported through the plasma would be ideal for achieving a more homogeneous coating.

The physicochemical properties of the carbon coating depend on powder position in the plasma. In our approach, the powders were spread across a Si wafer with most but not all of the particles immersed in the plasma. The height of the particles differed so the temperature and plasma density were variable across the powder sample. Independent substrate temperature control, rather than collisional heating in the plasma, would be ideal for achieving a more uniform sample temperature and hence, a more phase-pure diamond coating. Furthermore, particles buried in the center of the sample interact less with the reactive plasma species than do those particles at the surface. This leads to heterogeneity in the coverage and type of carbon formed. Even with these current technological limitations, the results clearly demonstrate that electrically conducting diamond particles can be produced by the core-shell approach and that these particles are more resistant to microstructural degradation and corrosion during anodic polarization than are GC powders.

The pipette electrode allows one to test the electrochemical properties of the powders conveniently without the need for a binder. The electrical conductivity data presented in Table 3.1 indicate that the packed powders are highly conducting, on par with GC and Vulcan XC-72 sp² carbon powders. A difficulty, however, with making a low-resistance electrode out of diamond is not the electrical conductivity of the individual powder particles but rather the resistance that results from poor particle–particle contact when packed. The diamond particles are hard and irregularly shaped. Therefore, they do not pack efficiently to yield high particle–

particle contact areas and cannot be compressed to increase the conductivity. The contact resistance, R_c , between particles is given by Eq. 3.1, and this limits the electrical conductivity of packed powders. It is larger for smaller diameter powders because the contact radius, b, becomes smaller between two spherical particles

$$R_{c} = \frac{\rho}{2h}$$
 [3.1]

where ρ is the specific resistivity (Ω cm) and b is the contact radius (cm) [62]. Innovative strategies will be needed to achieve lower resistance powder electrodes with small diameter diamond powders, like preparing electrodes with mixed diameter powders.

Reasonably good electrochemical behavior was exhibited by both the 500 and 100 nm doped diamond powders toward several aqueous redox systems. The data, particularly that for the 500 nm doped diamond powder, were very comparable to data obtained for high-quality, boron-doped nanocrystalline diamond thin-film electrodes.

The voltammetric data for the 100 nm doped diamond powder were more influenced by ohmic resistance than were the data for the 500 nm powder.

3.5 Conclusion

The deposition of B-UNCD layer on the insulating 500 and 100 nm diamond powder via CVD and its electrochemical, microstructural, and morphological characterization was reported. On the basis of these results, we can conclude that, 100 and 500 nm diam. diamond powders are coated with a thin layer of boron-doped diamond. According to BET surface area measurements the uncoated powders have higher surface area than the coated diamond powder. Overcoating makes the particles larger due to particle–particle fusion, which reduces the specific surface area. The relatively high electrical conductivity after acid washing proved that the electronic

properties of the diamond powder result from the doped diamond overlayer and not from any adventitious nondiamond carbon impurity phase. SEM images and Raman spectroscopy yielded further evidence in support of a nanocrystalline diamond overlayer. Both powders exhibited electrochemical responses for Fe(CN)₆^{3-/4-}, Ir(Cl)₆^{-2/-3}, and Fe^{+2/+3} that were comparable to typical responses seen for high-quality, boron-doped nanocrystalline diamond thin-film electrodes. The electrochemical behavior of the powders was assessed using a pipette electrode that housed the packed powder with no binder. The 100 nm doped diamond powder electrodes were more plagued by ohmic resistance effects than were the 500 nm powder electrodes because of reduced particle contact. Importantly, it was found that the doped diamond powder electrodes are dimensionally stable and corrosion-resistant during anodic polarization at 1.4 V vs Ag/AgCl (1 h) in 0.5 M H₂SO₄ at 80 °C. In contrast, GC powder polarized under identical conditions underwent significant microstructural degradation and corrosion.

References

- 1 . E. Fischer and G. M. Swain, J. Electrochem. Soc. 152, B369 (2005).
- 2 V. M. Swope, I. Sasaki, A. Ay, G. M. Swain, ECS Trans. 3, 27 (2007).
- D. Zhou, T.G. McCauley, L.C. Qin, A.R. Krauss, D.M. Gruen, Synthesis of nanocrystalline diamond thin films from an Ar-CH₄ microwave plasma, *J. Appl. Phys.* 83, 540 (1998).
- 4 R.-I. Stefan and S. G. Bairu, Anal. Chem., 75, 5394 (2003).
- 5 C. He, S. Desai, G. Brown and S. Bollepalli, Interface (Electrochem. Soc.) 14, 41 (2005).
- 6 H. A. Gasteiger, S. S. Kocha, B. Sompalli and F. T. Wagner, Appl. Catalysis B: Environ. 56, 9 (2005).
- M. F. Mathias, R. Makharia, H. A. Gasteiger, J. J. Conley, T. J. Fuller, C. J. Littleman, S. S. Kocha, D. P. Miller and C. K. Mittelsteadt, Interface (Electrochem. Soc.) 14, 24 (2005).
- 8 L. M. Roen, C. H. Paik and T. D. Jarvi, J. Electrochem. Soc. 151, E125 (2004).
- 9 D. Zhou, D.M. Gruen, L.C. Qin, T.G. McCauley, A.R. Krauss, Control of diamond film microstructure by Ar additions to CH4/H2 microwave plasmas, *J. Appl. Phys.* 84, 1981 (1998).
- S. Jiao, A. Sumant, M.A. Kirk, D.M. Gruen, A.R. Krauss, O. Auciello, Microstructure of ultrananocrystalline diamond films grown by microwave Ar-CH4 plasma chemical vapor deposition with or without added H2, *J. Appl. Phys.* 90, 118 (2001).
- 11 Angus, J. C.; Argoitia, A.; Gat, R.; Zhidan, L.; Sunkara, M.; Wang, L.; Wang, Y. *Philos. Topics*, *342*, 195-208, (1994).
- 12 J. C. Angus, H. A. Will, and W. S. Stankop, J. Appl. Phys. 39, 2915 (1968).
- 13 M. Frenklach, J. Appl. Phys. 65, 5124 (1989).
- 14 W. L. Hsu, J. Vac. Sci. Technol. A 6, 1803 (1988).
- 15 Y. Saito, K. Sato, H. Tanaka, K. Fujita, and S. Matsuda, J. Mater. Sci. 23, (1988).
- 16 Y. Liou, A. Inspektor, R. Weimer, D. Knight, and R. Messier, J. Mater. Res. 5, 2305 (1990).
- W. Zhu, A. Inspektor, A. R. Badzian, T. Mckenna, and R. Messier, J. Appl. Phys. 68, 1489 (1990).
- 18 D. Zhou, T.G. McCauley, L.c. Qin, A.R. Krauss and D. M. Gruen, J. Appl. Phys., 83, 540, (1998)
- 19 J.R. Rabeau, P. John, J.I.B. Wilson and Y. Fan, 1. Appl. Phys., 96, 6724, (2004).

- 20 P.W. May, J.N. Harvey, J.A. Smith, Yu. A. Mankelevich, 1. Appl. Phys., 99, 104907, (2006).
- 21 P.W. May, Yu. A. Mankelevich, J. Appl. Phys., 100, 024301, (2006).
- 22 D.M. Gruen, S. Liu, A.R. Krauss, J. Luo and X. Pan, Appl. Phys. Letts., 64, 1502 (1994).
- J. Birrell, J.E. Gerbi, a. Auciello and J.A. Carlisle, J. Phys.: Condens. Matter, 18, SI771, (2006).
- 1. Birrell, J.E. Gerbi, *a.* Auciello, J.M. Gibson, J. Johnson and J.A. Carlisle, Diamond Relat. Maters., 14, 86, (2005).
- 25 Y.K. Liu, Y. Tzeng, C. Liu, P. Tso and I. N. Lin, Diamond Relat. Maters., 13, 1859, (2004).
- 26 P.W. May, M.N.R. Ashfold, Yu. Mankelevich, J. App!. Phys., 101, 053115, (2007).
- N. Spataru, X. Zhang, T. Spataru, D. A. Tryk and A. Fujishima, J. Electrochem. Soc. 155, B264 (2008).
- N. Spataru, X. Zhang, T. Spataru, D. A. Tryk and A. Fujishima, J. Electrochem. Soc. 155, D73 (2008)
- G. M. Swain, in Electroanalytical Chemistry, A. J. Bard and I. Rubinstein, Eds, Vol. 22, p. 181-277, Marcel Dekker, Inc., New York (2003).
- 30 S. Alehashem, F. Chambers, J. W. Strojek and G. M. Swain, Anal. Chem. 67, 2812 (1995).
- 31 Y. Show, M. A. Witek, P. Sonthalia, G. M. Swain, Chem. Mater. 15, 879 (2003).
- 32 D. S. Knight and W. B. White, *J. Mater. Res.*, 4, 385 (1989)
- 33 S. A. Solin and A. K. Ramdas, *Phys. Rev. B*, 1, 1687 (1970)
- 34 M. Mermoux, B. Marcus, G. M. Swain, and J. E. Butler, *J. Phys. Chem. B*, 106, 10816 (2002).
- 35 D. Zhou, D. M. Gruen, L. C. Qin, T. G. McCauley, and A. R. Krauss, *J. Appl. Phys.*, 83, 540, (1998).
- 36 J. Birrell, J. E. Gerbi, O. Auciello, J. M. Gibson, D. M. Gruen, and J. A. Carlisle, *J. Appl. Phys.*, 93, 5606, (2003).
- 37 S. Prawer, K. W. Nugent, D. N. Jamieson, J. O. Orwa, L. A. Bursill, and J. L. Peng, *Chem. Phys. Lett.*, 332, 93 (2003).
- A. C. Ferrari and J. Robertson, in *Nanostructured Carbon for Advanced Applications*, p. 177, Kluwer Academic Publishers, Amsterdam, The Netherlands (2001).

- 39 A. C. Ferrari and J. Robertson, *Phys. Rev. B*, 63, 121405-1 (2001).
- 40 J. Birrell, J. E. Gerbi, O. Auciello, J. M. Gibson, J. Johnson, and J. A. Carlisle, *Diamond Relat. Mater.*, 14, 86 (2005).
- 41 P. C. Redford, D. A. Horner, L. A. Curtiss, and D. M. Gruen, *J. Phys. Chem.*, 100, 11654 (1996).
- 42 P. Zapol, M. Sternberg, L. A. Curtiss, T. Frauenheim, and D. M. Gruen, *Phys. Rev. B*, 65, 045403-1 (2001).
- 43 M. Sternberg, P. Zapol, and L. A. Curtiss, *Phys. Rev. B*, 68, 205330-1 (2003).
- 44 A. Krüger, F. Kataoka, M. Ozawa, T. Fujino, Y. Suzuki, A. E. Aleksenskii, A. Ya. Vul', E. Osawa, Carbon, 4, 1722–1730 (2005)
- 45 M. C. Granger, M. Witek, J. Xu,J. Wang, M. Hupert, A. Hanks, M. D. Koppang, J. E. Butler, G. Lucazeau, M. Mermoux, J. W. Strojek and G. M. Swain, Anal. Chem., 72, 3793 (2000).
- 46 P. Chen, M. A. Fryling and R. L. McCreery, Anal. Chem. 67, 3115 (1995).
- 47 Q. Chen and G. M. Swain, Langmuir 14, 7017 (1998).
- 48 K. R. Kneten and R. L. McCreery, Anal. Chem. 64, 2518 (1992).
- 49 M. C. Granger and G. M. Swain, J. Electrochem. Soc. 146, 4551 (1999).
- 50 I. Yagi, H. Notsu, T. Kondo, D. A. Tryk and A. Fujishima, J. Electrochem. Soc. 473, 173 (1999).
- 51 G. M. Swain, J. Electrochem. Soc. 141, 3382 (1994).
- 52 J. Wang, G. M. Swain, T. Tachibana and K. Kobashi, J.New Mater. for Electrochem. Sys. 3,75 (2000).
- 53 C. A. McDermott, K. R. Kneten and R. L. McCreery, J. Electrochem. Soc. 140, 2593 (1993).
- 54 J. F. Evans and T. Kuwana, Anal. Chem. 49, 1632 (1977).
- 55 J. F. Evans and T. Kuwana, Anal. Chem. 51, 358 (1979).
- 56 C. W. Miller, D. H. Karweik and T. Kuwana, Anal. Chem. 53, 2319 (1981).
- 57 D. T. Fagan, I-F. Hu and T. Kuwana, Anal. Chem. 57, 2759 (1985).
- 58 K. Kinoshita and J. Bett, Carbon 12, 71 (1988).

- 59 M. Cai, M. S. Ruthkosky, B. Merzougui, S. Swathirajan, M. P. Balogh, S.H. Oh, J. Power Sources 160, 977 (2006).
- 60 K. Kinoshita, in Carbon: Electrochemical and Physiochemical Properties, p. 72–79, John Wiley & Sons, Inc., New York (1988).

Chapter 4

Characterization of Redox-Active Surface of Carbon-Oxygen Functional Groups Formed on Boron-Doped Ultrananocrystalline Diamond Coated Powders.

4.1. Introduction

UNCD powder consists of small (~5 nm) particles with a surface that can be terminated with hydrogen or oxygen. Understanding the surface functionality of UNCD is important not only for stability and graphitization but also for controlling the chemical properties of the surface. Through control of the UNCD surface functionalization, a variety of biomedical applications can be achieved, such as separation, purification, and immobilization of nucleic acids and proteins,[1, 2-7] luminescent biochips,[4, 8] biosensors,[9] and drug delivery vehicles.[10]

A UNCD powder has a core consisting of sp³-hybridized carbon atoms with a diamond cubic lattice as shown by X-ray data. X-ray analysis also reveals the presence of a transient carbon shell around the core, consisting of amorphous carbon structures 4–10 Å thick. This amorphous envelope has a porous texture and contains numerous defects, ruptures in the carbon structures, and, sometimes, a small amount of hetero-atoms incorporated during the detonation synthesis. The functional groups have also been found to contain small amounts of hydrogen and nitrogen atoms, but most of them include oxygen in the form of hydroxyl, carboxyl, ketonic, lactonic, and other groups[12-15].

B-UNCD powder surfaces can be either hydrophobic or hydrophilic by controlling the surface chemistry. If a diamond coating was obtained in a hydrogen atmosphere, its surface is covered by a hydrogen monolayer and displays hydrophobic properties [11]. These surfaces are inert in the purest hydrogen-terminated sp³ form. [12-15].

Ultrananocrystalline diamond formed in Ar-rich mixtures is characterized by 50–100 nm nodules consisting of individual diamond grains (15 nm) connected to one another by 2–4 atom wide grain boundaries containing sp² bonded carbon.[16, 17] The high fraction of grain boundary gives rise to a relatively large number of sp²-bonded carbons. The UNCD samples, even after acid washed or hydrogen plasma treatment, may still contain some semi-quinone-like oxygen functionalities due to numerous defects and ruptures, which may affect electrochemical activity.

There is extensive literature on the oxygen functional groups that can exist on carbon surface. These groups can influence reaction activities, surface wettability, and pH values.[19-22] The methods for determining the coverage and types of the functional groups have been reviewed by Boehm [23]. X-ray photoelectron spectroscopy (XPS) is one efficient tool [24]. IRactive oxygen containing groups can also be distinguished by Fourier transform infrared spectroscopy [25]. Toebes et al. employed thermogravimetry to investigate the coverage and the thermal stability of the oxygen-containing surface groups on carbon material, together with acid—base titration and XPS [26].

Several electrochemical methods have been used to characterize these groups. These measurements do not provide a number of total oxide coverage, rather only these functional groups that are electrochemically active. Some electrochemical studies have been made by using linear sweep voltammetry at an electrode in deoxygenated electrolyte. These studies revealed anodic and cathodic peaks, which were attributed to the oxidation and reduction of quinone-like functional groups formed on the surface. [22, 23, 58-61].

In this chapter, investigation of the surface functional groups on B-UNCD coated glassy carbon and 3-6 nm diamond powders is described. The coated powders were compared to

uncoated GC powders. Raman spectroscopy, Fourier Transform Infrared (FT-IR) spectroscopy, cyclic voltammetry and differential pulse voltammetry (DPV) were employed to form the oxides on these powders. The purpose for the study was to determine the types of surface functional groups present on these powders before and after anodic polarization. DPV is a sensitive electrochemical method for detecting electroactive functional groups, and has been used in the past to study the functionalities of glassy carbon and carbon fibers.

4.2. Results

4.2.1. Morphology and Microstructure

Figure 4.1 shows representative SEM and HRTEM images of GC, B-UNCD-coated GC, acid washed 3-6 nm diamond powder and B-UNCD-coated diamond powder. Glassy carbon powder has a nominal diameter around 4 µm and it is spherical in shape with no observed porosity. The morphology of the B-UNCD-GC particles after a 2-h overcoating is noticeably rougher with a nodular morphology. The nodular morphology results from the nanometer faceting and the aggregates of diamond grains (10-20 µm diam.) UNCD is grown from an Arrich source gas mixture and this produces a high rate of diamond renucleation that is the reason of the ultrananocrystalline structure. As we have discussed in chapter 3, powder particles coated in this manner are often fused with agglomerates due to the fact that the diamond overlayer does not solely form on individual particles. Rather it forms over neighboring particles "cementing" them together. This is undesirably reduces the specific surface area of the material. The SEM images show that most of the GC powder surfaces get coated with UNCD layer but still small percentage of the powder remains uncoated or partially coated.

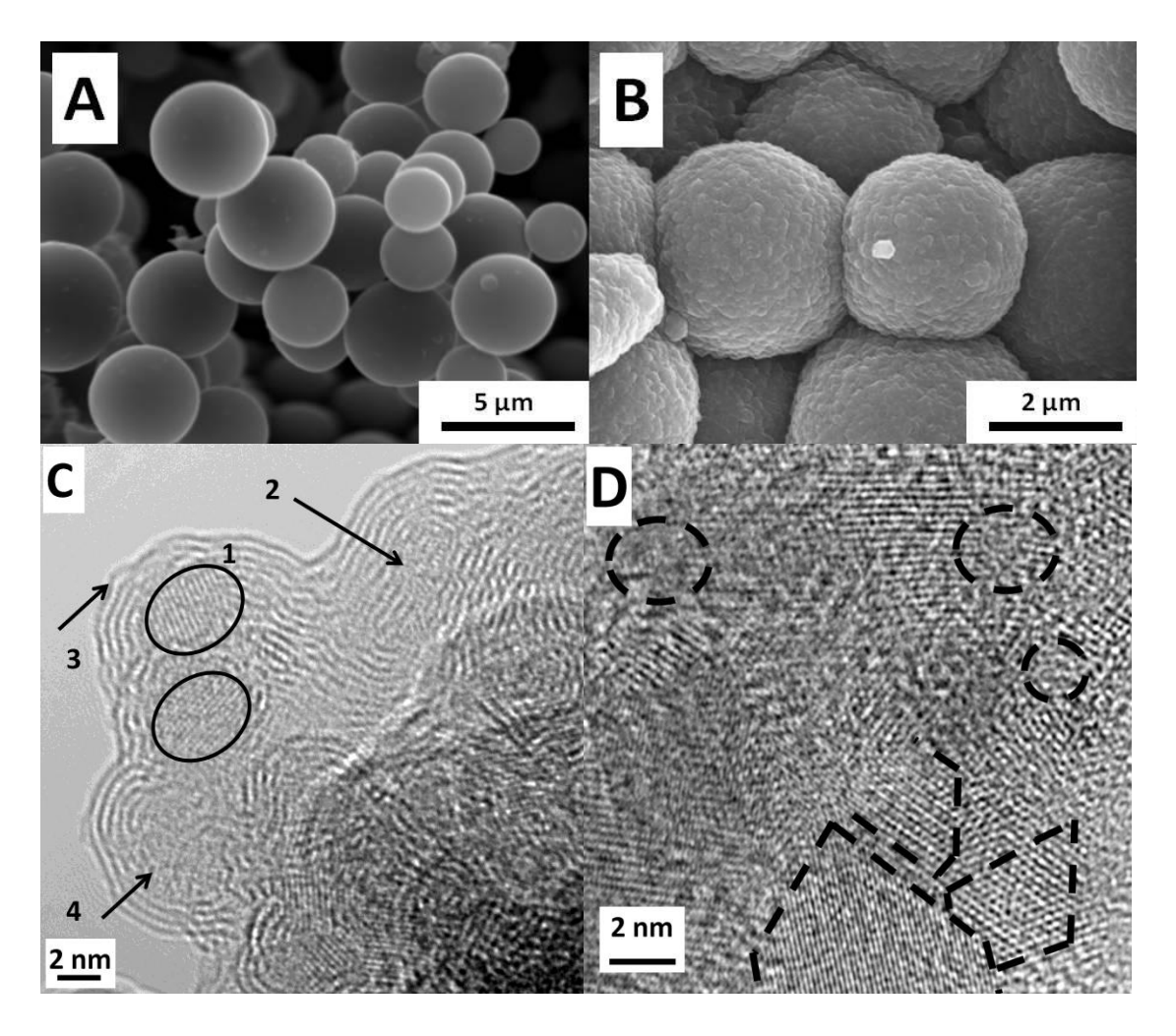


Figure 4.1 SEM and TEM images of (A) GC, (B) B-UNCD-coated glassy carbon, (C) acid washed 3-6 nm Diamond and (D) B-UNCD-Diamond powder. Notation used in the TEM: (1) Nanodiamond, (2) Carbon onion, (3) Fullerenic shell, (4) Amorphous carbon. [29]

In the HRTEM measurements, we observed larger particles for 3-6 nm diamond powder around 40-100 nm in diameter before overcoating. The detonation diamond powder tends to form aggregates due to a high surface free energy [28]. These clusters can be broken into 3-6 nm particles by intense sonication. The nanodiamond powder consists of a diamond (core) and a nondiamond sp² carbon outer shell structure after acid washing step, as evidenced in the HRTEM images. Figure 4.1C and 4.1D show representative images of acid washed 3-6 nm diamond and diamond powder coated with B-UNCD powder, respectively. Clearly the acid

washing treatment is not effective at removing the outer graphite skin when the skin is low in defects (edge plane). The powder core is diamond (indicating by circles in Figure 4.1C); however, there is a nondiamond structure, possibly amorphous carbon, fullerenic carbon shells, carbon onions and graphite ribbons on the surface [29]. After B-UNCD coating and the postgrowth acid washing, the diamond powder turned a darker grey color, which might be related to the content of sp² carbon as it is seen in HRTEM imaging.

UNCD nucleation and the crystalline grain size can be seen by using diffraction contrast yielded an average grain size of about 15 nm. We observed the nanodiamond nucleation as (111) lattice planes (lattice spacing= 0.206 nm) oriented around the diamond powder. Between the diamond grain, amorphous carbon was observed.

Raman spectroscopy was used to evaluate the carbon microstructure of the uncoated and coated powders. Figure 4.2 presents Raman spectra for (A) 3-6 nm acid washed diamond, (B) B-UNCD-diamond, (C) B-UNCD-GC, (D) GC powders. The intensity difference between the spectra is due, in part, to variable amounts of powder used. Figure

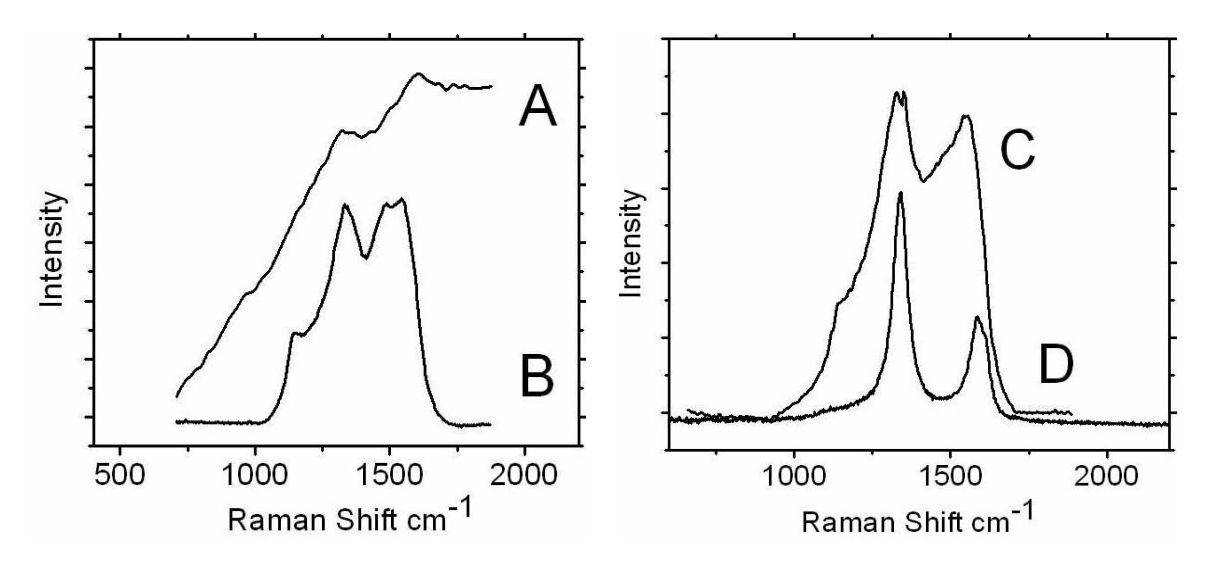


Figure 4.2. Raman spectra of (A) acid washed 3-6 nm diamond (B) B-UNCD-diamond, (C) B-UNCD-GC and (D) GC powder.

4.2A shows the Raman spectrum of uncoated diamond powder after acid washing. Raman spectra of diamond powders, as a function of the particle size were recorded by Yoshikawa. As the particle size become smaller the intensity of the diamond phonon line (1332 cm⁻¹) weakened. They postulated that the reason for the first order Raman band, which is characteristic feature of diamond was not be detected for diamond particles less than 5 nm was because of a confinement effect [30]. In our Raman spectra of the 3-6 nm diam, diamond powder, we observed this peak, however; the peak was broadened due to the transition from bulk to nanocrystalline diamond [31]. The broad Raman band at around 400-700 cm⁻¹ arises from the amorphous carbon [32]. The GC powder has two sharp peaks at 1350 and 1580 cm⁻¹, which are known D- and G-bands, respectively [33, 34]. The broad peak at 1350 cm⁻¹ arises from microstructural disorder (D band). This mode becomes active when a carbon material possesses small crystallites or a high fraction of crystalline boundary. The peak at 1580 cm⁻¹ originates from in-plane stretching mode of the bonded carbon atoms. In other words, the 1580 cm⁻¹ band is the in-plane lattice phonon of the material. The Raman spectra for B-UNCD-GC and B-UNCD-diamond are similar (Fig. 4.2B and 4.2C). The characteristic fingerprint of microcrystalline diamond is shown at 1333 cm⁻¹ as a single sharp peak. [35, 36]. As the diamond crystallites reduce in size from micrometer to nanometer size, more vibrational modes become Raman active. The B-UNCD GC spectrum has broad peaks at 1150, 1333, 1350, 1470, and 1550 cm⁻¹. These peaks are typical of boron-doped UNCD grown from Ar-rich source gas mixtures [37-40]. Peak shifting and asymmetric broadening has been observed in the 1332 cm⁻¹ peak for nanodiamond powders. This is due, in part, to the small diamond grain size (ca. 20-30 nm), but also to the D-band scattering intensity at 1350 cm⁻¹ from sp² carbon impurity. The peak at 1550 cm⁻¹ arises from the nondiamond sp²-bonded carbon atoms in the grain boundaries [41-43]. The peaks at 1150 and 1470 cm⁻¹ are often used as a signature for high quality nanocrystalline diamond, but have been assigned to sp² hybridized structure such as poly acetylene type molecules that may be present on the structure and in grain boundaries [42, 43].

4.2.2. Electrical Conductivity Measurements

In order to verify that a conductive UNCD layer formed over the powders, electrical resistance measurements were performed on the dry powder. As seen in the HRTEM image (Figure 4.1C), the as-received diamond powder has a graphite carbon structure surrounding a diamond core. Even after acid washing and H_2O_2 treatment, the outer graphitic shell still remained. The uncoated diamond powder had little conductivity (< 10^{-6} S/cm) after it was cleaned by acid washing. After B-UNCD deposition though, the conductivity of diamond powder increased to 0.7 (\pm 0.1) S/cm. Importantly, the conductivity unaltered by acid washing, consistent with a chemically stable, doped diamond coating. The conductivity of the GC and B-UNCD-GC powder was determined to be 1.4 and 1.6 S/cm, respectively.

4.2.3. Background Cyclic Voltammetric Current Density-Potential Curves

Figure 4.3 shows the cyclic voltammetric i-E curves for (A) GC, (B) B-UNCD-GC and (C) B-UNCD-diamond powder before and after anodic polarization at 1.4 V vs. Ag/AgCl (~1.6V vs. RHE) for 1 h in 0.5 M H₂SO₄. Unchanged curve shapes were observed after the 4th scan and the curves remained stable over an additional 16-cycle period. This reflects the microstructural stability of the material. The background current for the B-UNCD-GC powder is 10 times lower

than that for the GC powder even though the specific surface area of the powders is similar. B-UNCD-GC and diamond powder has similar E-i curves in acidic solution. The potential window increases some after UNCD coating for GC. The curves for B-UNCD-diamond powder appear very flat and featureless within the working potential window. It has none of this reactive redox couple on the surface that is detectable with cyclic voltammetry.

Glassy carbon which was polarized at 1.4 V vs. Ag/AgCl (~1.6 V vs. RHE) at 25 °C showed much larger anodic and cathodic peaks at 300 mV. The overall background current and charge also increased after polarization, consistent with an increase in the exposed surface area due to microstructural damage [44]. The influence of the UNCD coating is seen in Fig. 4.3B and 4.3C for B-UNCD-GC and B-UNCD-diamond, respectively. There is no notable change in the magnitude of the current after polarization at 1.4 V vs. Ag/AgCl in acidic solution. For B-UNCD-diamond, the background current slightly increased after polarization, and no peak observed before and after polarization.

4.2.4. Differential Pulse Voltammetric Analysis

Figure 4.4 shows the differential pulse voltammetric i-E curves for (A) GC, (B) B-UNCD-GC and (C) B-UNCD-diamond in 0.5 M H₂SO₄ before and after polarization at different potentials. The currents are normalized to the specific surface area of the powders. (Assuming the same amount of powder at the tip was polarized.) Broad anodic peaks are present for GC at 0.4 V vs. Ag/AgCl. The peak height increased with the anodic polarization potential. The peak area is proportional to the number of moles of surface oxides formed. Clearly the oxide coverage increased with polarization potential but the peak position did not change. The main peak potential for B-UNCD-GC powder is at 0.45 V vs. Ag/AgCl electrode. The magnitude of the

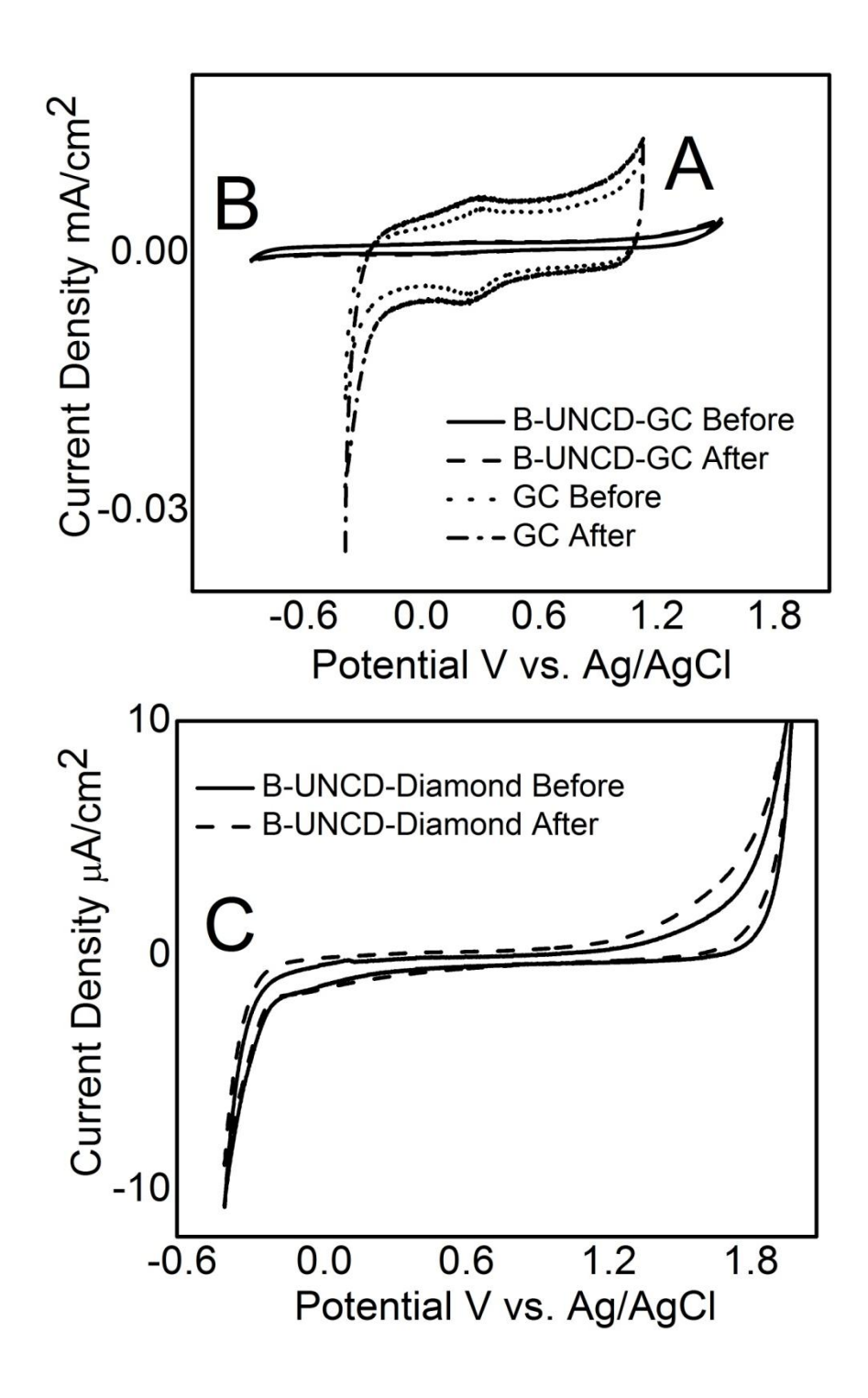


Figure 4.3. Cyclic Voltammetric i-E curves for (A) GC, (B) B-UNCD-GC and (C) B-UNCD-diamond powder in $0.5 \text{ M H}_2\text{SO}_4$ at 50 mV/sec before and after anodic polarization at 1.4 V for 1h at room temperature.

faradaic current for B-UNCD-GC is 2 orders of magnitude smaller than the GC powder even though their surface area is almost similar. After polarizations at 1.4 V and at 1.6 V vs. Ag/AgCl, this main peak shifted to positive direction approximately 70 mV. The current magnitude increased after each polarization for B-UNCD-GC powders. From the previous study, [44, 45] it has been seen that GC powders were fractured and broken apart during the polarization. We observed that microstructural degradation and corrosion produce new active sites for the functional group formation and result in increase in the amplitude of the current. Even very small number of uncoated powder presence may influence this peak amplitude.

Before polarization, another peak appeared around 0.25 V vs. Ag/AgCl electrode. After polarization at 1.4V and 1.6 V vs. Ag/AgCl, this peak did not appear. The broad peaks seem to involve at least two different redox processes. These peaks might be related to o-and p-quinone structures in which the latter structure presents in lower concentration [46].

bifferential pulse voltammograms for B-UNCD-diamond in 0.5 M H₂SO₄ solution are shown in Fig. 4.4C. Even though it cannot be detectable by cyclic voltammetry, a broad peak around 0.35 V and 0.8 V are seen by DPV. The redox-active functional groups were not expected since these powders were acid-washed and H₂O₂ treated and hydrogen terminated. The amplitude of the peak after anodic polarization at 1.2 V vs. Ag/AgCl electrode did not change noticeably. The current increased after 1.4 V and 1.6 V vs. Ag/AgCl polarizations.

In order to clarify source of the current observed in DPV studies, an ultrananocrystalline, a nanocrystalline and a microcrystalline thin film electrodes were tested in 0.5M H₂SO₄. Microcrystalline and nanocrystalline thin film diamond electrodes were chosen because the electrode surfaces were hydrogen terminated during postgrowth annealing in atomic hydrogen to

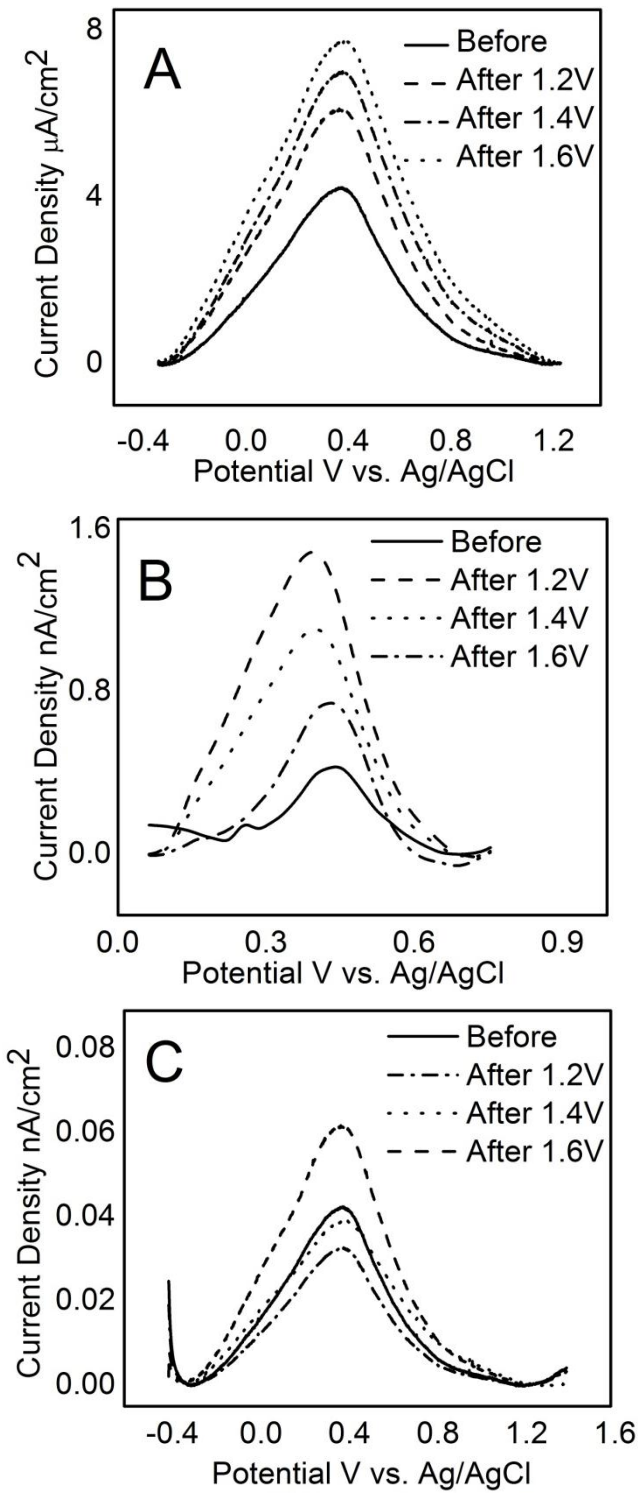


Figure 4.4 Differential Pulse voltammetric i-E curves for (A) GC, (B) B-UNCD-GC and (C) B-UNCD-diamond in 0.5M H₂SO₄. Polarization potentials were 1.2, 1.4 and 1.6 V for 1 h each

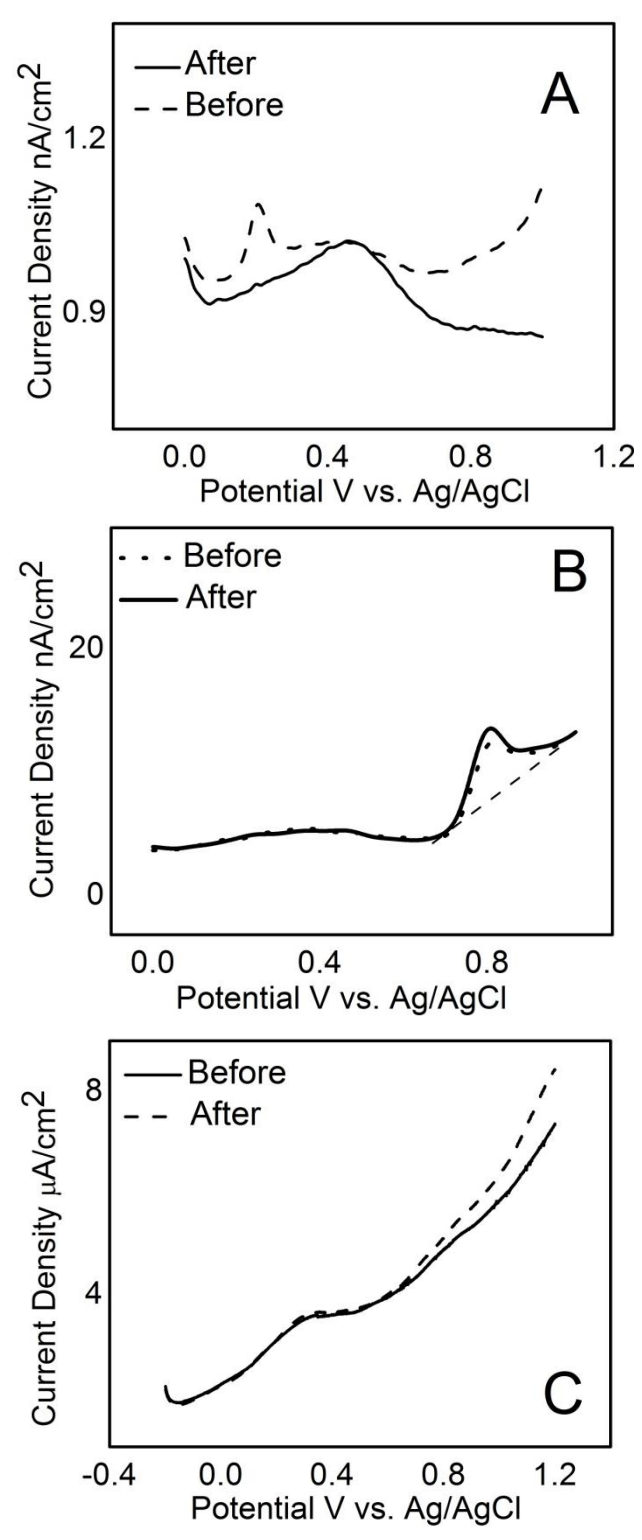


Figure 4.5 Differential Pulse voltammetric i-E curves for (A) Microcrystalline, (B) Nanocrystalline and (C) Ultra-nanocrystalline diamond thin film electrodes in $0.5M\ H_2SO_4$ before and after polarization at $1.4V\ vs.\ Ag/AgCl$ for 1 h.

gasify any adventitious nondiamond sp² carbon impurity and to minimize dangling bonds. We assume, microcrystalline diamond electrode has minimum sp² carbon impurity, compared to nanocrystalline and ultrananocrystalline due to larger grain boundaries. For ultrananocrystalline diamond film electrode growth condition is the same for powder coating. This comparison will give us idea about the sp² impurities at the grain boundaries (film electrode) and sp² impurities due to non-diamond growth like graphene plate for powder [47]. Figure 4.5 shows differential pulse voltammograms before and after polarization at 1.4V vs. Ag/AgCl electrode. The currents were normalized to electrode area which is 0.2 cm².

For microcrystalline electrode before polarization we observed a peak around 0.3V. After polarization this peak removed and a broad peak was detected between 0.1 V to 0.7 V. We speculate that these surface impurities originated from the reaction chamber during shutdown procedures of the microwave system. These peaks could not be detected by cyclic voltammetry due to low intensity of the peaks. The DPV voltammograms obtained for NCD film electrode is similar to B-UNCD-diamond powder electrodes. A broad peak around 0.3 V was observed before and after polarization. The peak intensity at 0.8V decreased after anodic polarization. This peak is assigned to the oxidation of the grain-boundary sp² carbon, where electrochemically-active carbon–oxygen functionalities can form [48-50]. The peak intensity at 0.8 V is larger for UNCD electrodes compared to NCD film electrodes which shows that the UNCD film has more sp² carbon than does the NCD film due to the higher fraction of grain boundaries. Our previous studies on these electrodes suggest that these electrodes likely possess a mixed sp²–sp³ microstructure [51]. We did not observe this peak on microcrystalline diamond electrode.

Figure 4.6 shows the dependence on potential of the mole of electrochemically active surface oxides introduced to the surface groups by polarization. Mole number of electrochemically active surface oxides was calculated from the area under anodic peaks

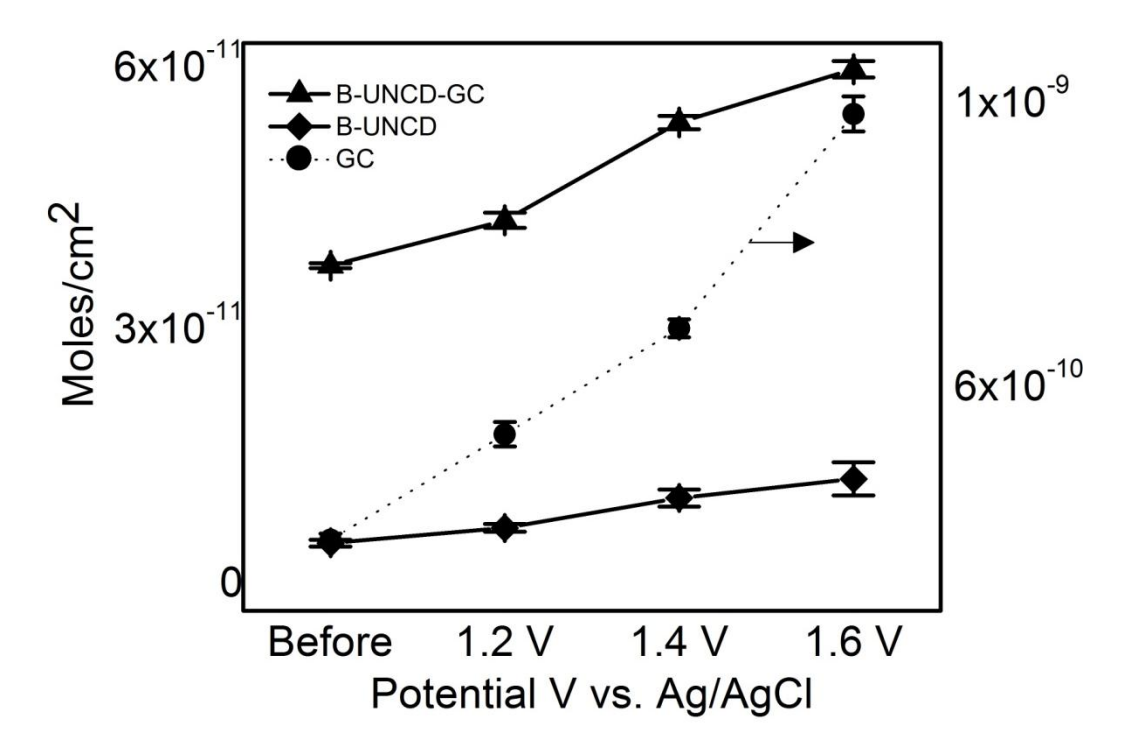


Figure 4.6 Electrochemically active surface oxide species on GC ($-\bullet-$), B-UNCD-GC ($-\bullet-$) and B-UNCD-diamond powder ($-\bullet-$) before and after anodic treatment at different potentials in 0.5 M H₂SO₄ for 1 h at room temperature. Experiments were repeated 3 times with freshly prepared pipette electrodes.

of differential pulse voltammograms and normalized to the specific surface area of the powders. We assume redox reaction in reaction 1 takes place on the surface. For GC and B-UNCD-GC powder, mole number increases as the polarization potential increase. For GC, the rate of the change raised up rapidly after 1.4V vs. Ag/AgCl polarization. For B-UNCD-GC electrochemically active surface oxides increase with potential however we did not observe any

sharp increase as potential increase up to 1.4V. The magnitude of the surface oxide amount is 10 fold less for coated glassy carbon which is a good indicator of diamond overcoating. This shows that diamond coated glassy carbon powders are more resistant to oxidation and corrosion than uncoated GC powders at high potentials.

For B-UNCD-diamond powders, the redox-active surface oxide molecules are almost 2 orders of magnitude smaller than GC. As it is shown in the Fig. 4.6, polarization at 1.2 V vs. Ag/AgCl did not change the surface oxide amount on diamond powder. As the polarization potential increases to 1.4 V and 1.6 V vs. Ag/AgCl, surface oxides slightly increase. At these high potential, electrochemical anodization of diamond surfaces in acidic media showed a surface composition dominated by ether (C–O–C), carbonyl (C=O) and hydroxyl (OH) groups. The presence of the surface hydroxyl species was demonstrated by FT-IR measurements. Therefore, the charge increase observed in DPV measurements is due to this change in surface chemistry of diamond powders.

4.2.5. Fourier Transform Infrared Spectroscopy (FTIR) Characterization

Differential pulse voltammetry is a very sensitive technique for the detection of electrochemically active functional species. However, the corresponding electrochemical results represent only functional groups which are electrochemically active. Therefore, FT-IR was applied to obtain IR active functional groups, adsorbed molecules, and impurities on the surface of the carbon powders. The physico-chemical structural changes of glassy carbon, hydrogen terminated and anodicly polarized diamond powder were studied by FT-IR, as shown in Fig. 4.7. Table 4.1 lists the assignments of the IR frequencies of B-UNCD. In order to assign the IR bands of B-UNCD more completely, the frequency positions of some of the superimposed peaks are determined in deconvoluted and second derivative spectra derived from the absorbance

spectra. Origin program was used to obtain Gaussian curve fitting and for the approximate relative proportions of the component peaks. In the table, the relative proportion is written near the observed peak after different experimental conditions.

The main features in the FT-IR spectra of all powders are related to C-H (2854-2920 cm⁻¹), C=O (1740-1757 cm⁻¹), and -OH vibrations (3280-3675 cm⁻¹ stretch). The peak at 2920 cm⁻¹ and the shoulder around 2850 cm⁻¹ are attributed to aromatic and aliphatic C-H asymmetrical and symmetrical stretching vibrations, respectively. The peak at 1740-1757 cm⁻¹ is characteristic for -COOH. The band at 1640 cm⁻¹ can be assigned to aromatic C=C in-plane stretching vibration and -OH bend vibration (1640-1660 cm⁻¹). The adsorption band at 1600cm⁻¹ is attributed to carbonyl stretching frequency for quinone groups. The presence of the peaks at 1640-1660 cm⁻¹ is also evidence of graphitic structure of the powders. It is reasonable to expect some shifts in wavenumbers of the surface groups, since the surface species on powders differ slightly from the ordinary functional groups of organic compounds having quite definite characteristic frequencies.

It is found that B-UNCD powders adsorb atmospheric water and in the IR region of OH stretching vibration of water centered at 3412 cm⁻¹ observed. [52] –OH region is an important part of the spectra to understand the formation of oxide layer after polarization. Therefore, to evaluate the effect of absorbed water on diamond coated powders spectra, two different spectra before and after long term heating were compared. Figure 4.7C shows the spectra of the hydrogen terminated diamond powders after heat treatment at 150 °C for 24 hours and immediately transferred to the sample chamber of FTIR instrument. The strongest band, - 3430

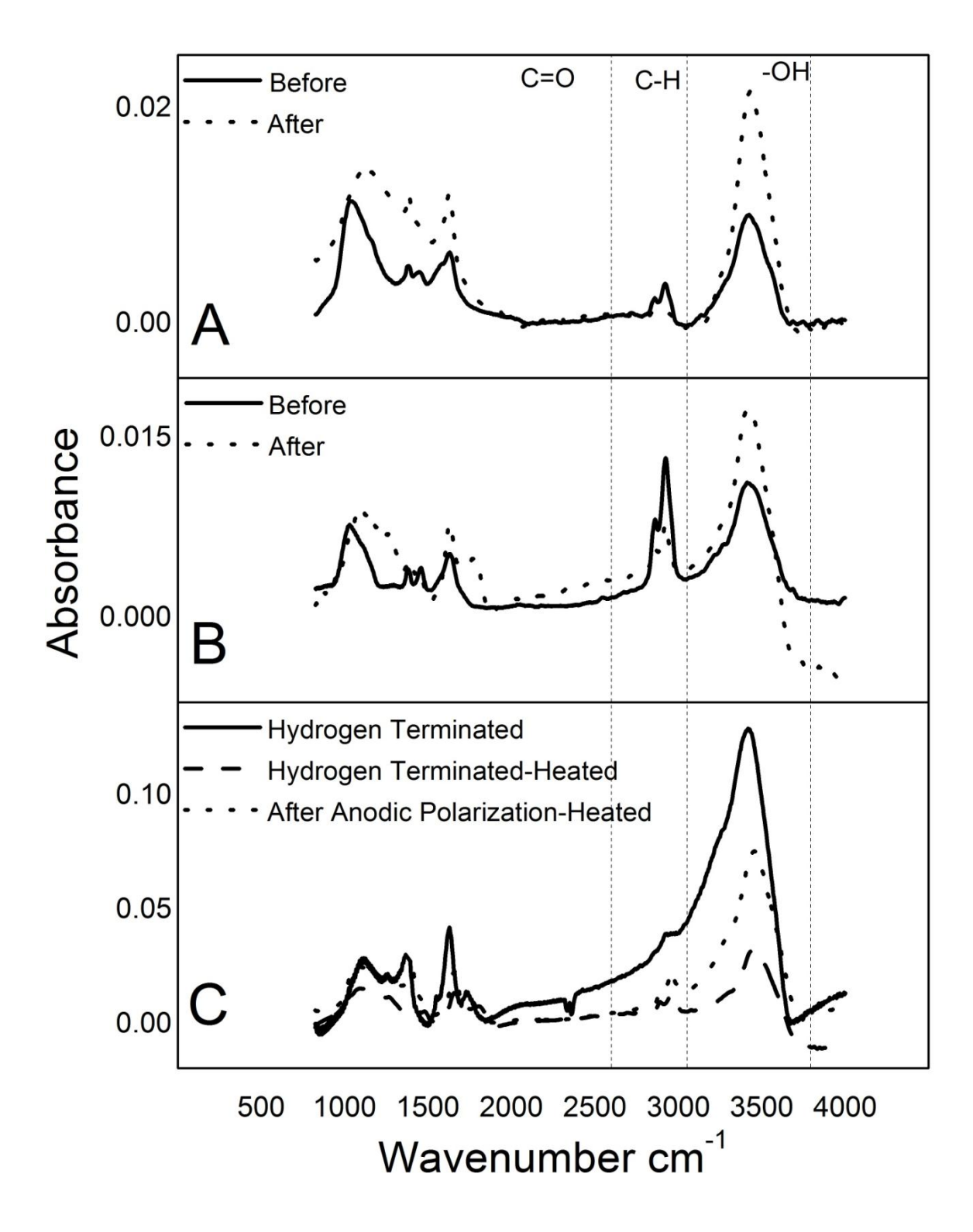


Figure 4.7 FT-IR spectra of (A) GC, (B) B-UNCD-GC and (C) B-UNCD-diamond powder before and after anodic polarization at 1.4 V vs. Ag/AgCl for 1 h in 0.5 M H_2SO_4

Table 4.1 Summary of main IR frequencies of Glassy Carbon, B-UNCD coated Glassy carbon powder

Glassy Carbon				B-UNCD coated Glassy Carbon			Assignment	
Before Polarization		After Polarization		Before Polarization		After Polarization		
				1	026	1	1026	νC-O-C etheral
1040		1040 ↑						δОН
				1090		1090 ↑		vas COC ether δΟΗ
				*		1265		vC-O epoxy, ≡C- OH,
1	1380		1384 ↑		1378		378 ↑	δCH, δΟΗ
1460		1457↓		1459		1459		δas CH3, CH2, CH δs CH3, δOH
1628		1626 ↑		1627		1627 ↑		δOH Water
				*		1780		carbonyl, cyclic carboxylix anhydride
2858		2858 ↓		2858-5		2858-6		CH2 sym
				2890-6		2890-5		CH3 sym
2	921	2921 ↓		2923-5		2923-12		CH2 asym
				2950-9		2950-5		CH3 asym
	3560-1		3563-5		3556-5		3552-5	Tertiary alcohol
3422	3431-9	3436 ↑	3431- 11	3418	3432- 16	3418	3430-22	vOH water
	3260-2		3252-1		3276-8		3260-11	bonded OH

Table 4.2 Summary of main IR frequencies of B-UNCD coated diamond powder

<u></u>		B-UNCI	oated diamond powder Assignment					
		iamond	Assignment					
Before Polarization		Before Polarization		After Polarization				
Hydrogen Terminated		Hydrogen Terminated						
	Heat treated							
1028		1028		1028		νC-O-C ethereal		
						δОН		
1	1096		1096 ↓)96↑	vas COC ether δOH		
1	1265		1260 ↓		65↑	νC-O epoxy, ≡C-OH,		
1	1381		1367 ↓		881↑	δСΗ, δΟΗ		
1	1459		1459		59↓	δas CH3, CH2, CH		
						δs CH3, δΟΗ		
1	1551		1558		50↑	δ ΝΗ		
1	1629		1625↓		29↑	δOH Water		
*		*		1781		carbonyl, cyclic carboxylix anhydride		
28	2858-3		2858-5		58-5	CH2 sym		
28	2890-6		2890-36		90-13	CH3 sym		
29	2923-4		2923-5		23-6	CH2 asym		
29	2950-2		2950-21		50-19	CH3 asym		
	3559-3		3554-1		3553-1	Tertiary alcohol		
3422	3432-12	3413	3436-5	3422	3424-6	vOH water		
_	3269-5		3250-3		3254-2	bonded OH		

cm⁻¹, is mainly the vOH of adsorbed water, its intensity decreases to about 70% of the original after heating at 150 °C for 24 hours, and the intensity of bending mode of hydroxyl group of water (- 1630 cm⁻¹) also weakens greatly after thermal treatment. Since no water or crystallization is expected in this B-UNCD powder, we assume that, other hydroxyl species are formed on the surface that also make contributions to 3426 and 1630 cm⁻¹ bands as described by Struck and Evelyn [53].

For pure diamond, only two phonon (or second order) absorption processes (the broad bands around 2000 cm⁻¹, C-C bond) are infrared-active. However, as the size becomes smaller and as the presence of defects in structure and surface impurities cause the forbidden single phonon modes to become infrared active.

For GC powder, after oxidation, -CH2- and -CH3 groups stretching vibration mostly removed from GC powder and the intensity of -OH (3434 cm⁻¹) groups is increased about 70 % after anodic treatment in acidic solution. The intensity of bending mode of hydroxyl group (1630 cm⁻¹) also became stronger after electrochemical oxidation. Since intensity of C-H decreased, we assume C-OH vibration also contributed. The broad absorbance near 1130 cm⁻¹ in both spectra before and after polarization is assigned to the v_{C-O-C} of ethereal type according to the characteristic frequencies tables [64]. The small peak at 1440 cm⁻¹ is attributed to asymmetric stretching of -CH2- bonds. After anodic polarization this peak intensity decreased which is evidence of surface oxidation.

The major changes in the functional groups after oxidation were found for B-UNCD-GC powder. After oxidation, -C-H groups stretching peaks intensity between 2800-3000 cm⁻¹ decreased. Gaussian fitted spectra of this powder before polarization in this region showed that 4 different kinds of C-H stretching vibrations (2856, 2890, 2923, and 2950 cm⁻¹) are observed with relative proportions of 5:6:5:9. The peak at 2950 cm⁻¹ is due to asymmetric stretching and 2890 cm⁻¹ is due to symmetric stretching of -CH3 groups which are indication of UNCD overcoating. After oxidation, relative proportion changes to 6:5:12:5: which shows a decrease in the -CH3 asymmetric vibration and increase in the asymmetric (2923 cm⁻¹) vibration of -CH2 stretches. The intensity of -OH groups at 3418 cm⁻¹ is increased which shows the oxidation of the -CH2 and -CH3 groups. The most characteristic feature of B-UNCD-GC powders before and after anodic polarization is displayed in the absorbance around 1775 cm⁻¹ that is the carbonyl groups. This peak which appears after polarization of powder is attributed the ketonic (>C=O) group which has a rigid cyclic structure like cyclopentanone. The broad peaks between 950 to 1330 cm⁻¹ are assigned to the different vibrational modes of C-O-C and C-OH groups. The peak appears at 1270 cm⁻¹ after polarization is suggested to the presence of =C-OH groups [65].

The significant changes were observed for B-UNCD- diamond powders' IR spectra. We have started with acid washed and hydrogenated diamond powder. -OH and C=O oxides still on the surface of the diamond powder after acid washing and hydrogen termination. From at least three different kinds of OH stretching vibrations (3558, 3434, 3245 cm⁻¹) are observed with relative proportions of 3:12:5. -OH vibration intensity at 3426 cm⁻¹ increased approximately

50% after polarization. For C-OH stretching, we observed a shoulder around 3256 cm⁻¹ and a main peak around 3430 cm⁻¹. In this boad peak, by fitting at least 3 different kinds of -OH stretching vibrations can be assigned to different structures. The 2 shoulders ~3256 and ~3560 cm⁻¹ are assigned to the tertiary alcohol on the diamond powder surface. Another difference in IR spectra of B-UNCD-diamond powder after anodic polarization is the peak around 1730 cm⁻¹. These peaks are assigned to the carbonyl (>C=O), aldehyde or carboxyl group. In the IR spectra we observed a shift from 1790 cm⁻¹ to 1740 cm⁻¹ after anodic polarization. The peaks at 1790 cm⁻¹ are due to formation of cyclic ketonic carbonyl groups. This peak suggests that before anodic polarization in acidic environment oxide functional groups on diamond present even after hydrogen termination. After polarization, ester type of carboxylic type carbonyl species (~1740 cm⁻¹) predominates. The very broad absorption features in the region of 1500-1000 cm⁻¹ in diamond samples before and after polarization are not different significantly. In this region, the peaks between 1305 and 1200 cm⁻¹ are assigned to the bending mode of C-H, in CH, CH2 and CH3. The peak at 1260 cm⁻¹ is assigned to the C-O vibration in epoxy structure.

3-6 nm diamond powder is prepared by explosive detonation. Therefore, it is reasonable to expect bonding of nitrogen in the bulk or on the surface of the powders. We found that, there is an IR frequency assigned to the amide group, combination of N-H bending mode and C-H vibrational mode around 1550 cm⁻¹. This peak is shifted slightly by heat treatment and anodic polarization however the intensity of the peak does not change significantly. Since we did not

observe this peak in other sp² coated powders, we could assume that amino carbonyl groups also exist in the diamond powder.

It was observed by FT-IR spectroscopy that the region where C-H bending occurs (peaks between 1200 and 1305 cm⁻¹) did not change before and after anodic polarization. It is suggested that electrochemical treatment does not affect bulk chemistry of boron doped diamond electrodes but only the surface chemistry. The main difference between the powder before and after oxidation is the –OH peak intensity which is indication of surface oxide formation on all powders. The most characteristic difference between B-UNCD-GC and B-UNCD-diamond powder the absorbance peak around 1775 cm⁻¹ which appears after polarization of B-UNCD-GC powder. We assume this structure on coated glassy carbon occurs due to hydrogenated glassy carbon surface. As it has discussed in the previous work that, before overcoating GC powders, hydrogen termination is the transition step from sp² to sp³ bonding. Due to non-homogeneous coating there might be some powders that remain as hydrogen terminated but not fully coated with B-UNCD layer. This heterogeneity in the coating may result oxidation of these hydrogen terminated surfaces and cyclic structure like cyclopentanone.

4.3. Discussion

Previous studies about the surface properties of diamond proposed the existence of "dangling bonds" on the surface [54]. These chemically unsaturated surface carbon atoms have free valences, which may be saturated by chemisorptions of foreign elements or which may react with foreign elements to form bonded surface functional groups.

SEM images showed very small percentages of the powders which may interact less with the reactive plasma species were not homogeneously coated. The heterogeneity in the coverage and type of carbon formed maybe a reason to observe oxygen functional groups on B-UNCD coated powders. The powders' physicochemical properties depend on powder position in the plasma, the height of the particles, temperature, plasma power, time and density of reactive gases as discussed in chapter 3. This heterogeneity in the coating caused different types of carbon growth in the intercrystallite boundaries (like diamond like carbon, graphitic carbon or graphene nanoplatelet structure) Different carbon lattice structures have different strength to oxidation and diverse degrees of diamond surface oxidation may be seen at these high potential. Raman spectra were used to confirm that the platelet microstructure is indeed nanocrystalline graphite with a high fraction of exposed crystallite edges. We suggested that the oxygen functional groups that are detected by electrochemical measurements and FT-IR measurement are due to these non-diamond carbon impurities which are observed at grain boundaries and in the interstitial spaces at the bottom of the nanocrystalline diamond coated powders.

The Raman spectroscopy results suggest that grain boundaries has trans-polyacetylene oligomers with different conjugation lengths in the grain boundaries [42, 55]. These oligomers have a mixture of sp² and sp³ bonding and differ in length depending on the film quality. They may also contribute to the intensity of the broad peak. When we compare DPV results on UNCD films and B-UNCD-diamond powder similar results were observed which suggests the similar structures of the powders. For B-UNCD-diamond powder case, these impurities ratio might be higher than the film electrode due to heterogeneous overcoating. The powders have some nanoplatelet graphite structure where UNCD films do not [56].

The surface chemistry resulting from the electrochemical treatment is very complex. The oxygen functional groups on carbon surfaces lead to significant influence in electrochemical reactivity, adsorption, and stability [21, 57].

We observe a decrease in the background current for B-UNCD coated GC powder. The carbon oxygen functional groups on the GC surface incorporate to the inner or outer Helmholtz plane, and contributed to the increase in the double layer capacitance. The decreased current is attributed to the decreased pseudocapacitance associated with redox-active and/or ionizable carbon-oxygen functional groups on the diamond-coated surface. The GC surface possesses carbon-oxygen functional groups populating the edge plane sites and some of these all electroactive (e.g. quinone/hydroquinone) [22, 23, 58-61]. These functional groups give rise to the present anodic oxidation peaks centered at ca. 0.4V and cathodic reduction peak at about 0.38 V vs. Ag/AgCl. For B-UNCD coated powders, these peaks are broad between 0.2V to 0.5V and slightly shift from the peak that is observed on GC powder. These values are in the range for usual quinoid compounds [62]. From DPV results it can be suggested that various oxide groups and different structure of polycyclic nature of carbon powder surface causes a shift of redox potential expected for the quinone groups.

This study shows that, the response of the powders before and after B-UNCD coating depends on the potential that is applied to powders during anodic polarization. Figure 4.7 shows the effect of polarization potential on electrochemically active surface oxide on these powders. The current increased after 1.4 V and 1.6 V polarizations for all powders. At these high potentials, the diamond surface gets converted from an H-terminated one to an O-terminated one in acidic solution. Usually around 2 V vs. RHE is applied for a certain time (\sim 30 min) to oxidize boron doped diamond film electrodes. After electrochemical oxidation in acidic environment, pure diamond should have cyclohexanol like functional groups while glassy carbon surface oxide has catechol like surface structure due to extended π bonding.

For GC, the rate of the change raised up rapidly after 1.6V vs. Ag/AgCl polarization, which is due to degradation of the glassy carbon powders at that high potential in acidic solution [44]. This increase suggesting that anodic oxidation is severe at this high potential and most probably polarization occurs at higher surface area. This sharp increase in the surface oxide on GC powder at 1.6V can be also explained in terms of the porous structure of the glassy carbon powder surface. The pores are very small and oxidation of these pores needs larger overpotential than the surface oxidation.

In our study, we observed surface oxidation occurs on boron doped UNCD coated 3-6 nm diamond powders at potential around 1.4 V vs. Ag/AgCl electrode. The oxidation peak that is observed at 0.8 V also observed on boron doped UNCD film electrodes in previous studies [63]. It is suggested that these peak is due to graphite-oxide structure that is present in low concentration sp²-hybridized carbon which is commonly resulting in films produced by CVD growth techniques. The same structure could exist on B-UNCD coated powders. As it is seen in the results that, for diamond surfaces sp² impurity can be gasified at potentials around 1.2V vs. Ag/AgCl electrode, however for diamond surface oxidation in acidic solution the potential should be higher than this value.

4.4. Conclusion

The samples of GC, B-UNCD-GC and B-UNCD diamond powders were examined before and after anodic polarization by cyclic voltammetry, DPV and FT-IR spectroscopy. The SEM and HRTEM images show that most of the GC powder and 3-6 nm diam. diamond powder surfaces get coated with UNCD layer but still small percentage of the powder remains uncoated or partially coated. The electrochemically active surface oxide peaks on B-UNCD-diamond and B-UNCD-GC powders are very similar. The electrochemical results have shown that powders

polarized larger than 1.2 V can easily be oxidized and modified with oxygen functionalities in acidic solution. It was found that the B-UNCD-coated powders are more stable to surface oxidation than GC powders during anodic polarization at 1.4 V vs. Ag/AgCl 1 h in 0.5 M H₂SO₄.

When surface charges normalized to specific surface area B-UNCD diamond powder has very small amount of surface oxide compare to GC and B-UNCD-GC. As it is shown in figure 4.6, the change of surface oxide is 100 times less for B-UNCD-coated powders. The DPV study comparison of thin film diamond electrodes and powders show that electrochemically active surface oxide responses coming from grain boundaries for thin film electrodes. For B-UNCD-GC powder both sp² structure at grain boundaries and non-diamond impurity contributed to these electrochemical responses. The FT-IR measurements showed that the surface functionalities are very similar for B-UNCD-diamond and B-UNCD-GC powder. –OH and C=O structures were observed in FT-IR spectra which are the source of electrochemically active quinone/hydroquinone structure. It is shown in this work that B-UNCD-diamond powders contaminated with a small amount of adsorbed hydrocarbons and oxygen functionalities which are accumulated in the grain boundaries. We also observed adsorption of water molecules on diamond powders. Polarization of the powders could convert some C-H bonds to the surface hydroxyl group for all powder types. This conversion is observed on GC powders predominantly.

References

- 1. Fischer, A. E.; Swain, G. M. J. Electrochem. Soc. 2005, 152, B369.
- 2. Ay, A.; Swope, V. M.; Swain, G. M. J. Electrochem. Soc. 2008, 155, B1013.
- 3. Martin, H. B.; Argoitia, A.; Landau, U.; Anderson, A. B.; Angus, J. C. *J. Electrochem. Soc.* 1996, 143, L133.
- 4. Redford, P. C.; Horner, D. A.; Curtiss, L. A.; Gruen, D. M. J. Phys. Chem. 1996, 100, 11654.
- 5. Zapol, P.; Sternberg, M.; Curtiss, L. A.; Frauenheim, T.; Gruen, D. M. *Phys. Rev. B* 2001, 65, 045403-1.
- 6. Miller, B.; Kalish, R.; Feldman, L. C.; Katz, A.; Moriya, N.; Short, K.; White, A. E. J. Electrochem. Soc. 1994, 141, L41.
- 7. Rodr'ıguez-Reinoso, F. Carbon, 1998, 36, 159.
- 8. Auer, E.; Freund, A.; Pietsch, J.; Tacke, T. Appl. Catal. A 1998, 173, 259.
- 9. McCreery, R. L.; *Electroanalytical Chemistry*; Bard, A. J.; Ed.; Dekker: New York, 1991; 17, 221.
- 10. Kinoshita, K. Carbon: Electrochemical and Physicochemical Properties; Wiley: New York, 1988.
- 11. Boehm, H. P. Carbon, 2002, 40, 145.
- 12. Aleksensky A.E., Baidakova M.V., Vul' A.Ya., and Siklitzky V.I. The structure of a diamond cluster. *Fizika Tverdogo Tela*, 1999, Vol. 41, No. 4, pp. 740–743 (Russian edition).
- 13. Dolmatov V.Yu. and Fudjimura T. Nanodiamonds. *Superhard Materials*, 2001, No. 6, pp. 31–37.
- 14. Mazanov V.A. Macrokinetics of the retention of condensed carbon and detonation diamond in a hermetic explosion chamber. *Physics of the Solid State*, 2004, Vol. 46, 4, pp. 629–635.
- 15. Boehm, H. P. Adv Catal. 1966, 16, 179.
- 16. Bard, A. J.; Faulkner, L. R.; *Electrochemical Methods: Fundamentals and Applications*, 2nd ed., John Wiley and Sons, New York, 2001.
- 17. Schwartz, R.; Robbins, H. J. Electrochem. Soc. 1976, 123, 1903.
- 18. Wang, Y.; Alsmeyer, D. C.; McCreery, R. L. Chem. Mater. 1990, 2, 557.
- 19. Dennison, J. R.; Holtz, M.; Swain, G. M. Spectroscopy, 1996, 11, 38.
- 20. Solin S. A.; Ramdas, A. K. Phys. Rev. B 1970, 1, 1687.

- 21. Mermoux, M.; Marcus, B.; Swain, G. M.; Butler, J. E. J. Phys. Chem. B, 2002, 106, 10816.
- 22. Show, Y.; Witek, M. A.; Sonthalia, P.; Swain, G. M. Chem. Mater. 2003, 15, 879.
- 23. Gruen, D. M. Annu. Rev. Mater. Sci. 1999, 29, 211.
- 24. Gruen, D. M. MRS Bull. 1998, 23, 32.
- 25. Arenal, R.; Montagnac, G.; Bruno, P.; Gruen, D. M. Phys. rev. B 2007, 76, 245316.
- 26. Birrell, J.; Gerbi, J. E.; Auciello, O.; Gibson, J. M.; Gruen, D. M.; Carlisle, J. A. *J. Appl. Phys.* 2003, 93, 5606.
- 27. Ferrari, C.; Robertson, J. Phys. Rev. B 2001, 63, 121405-1.
- 28. Birrell, J.; Gerbi, J. E.; Auciello, O.; Gibson, J. M.; Johnson, J.; Carlisle, J. A. *Diamond Relat. Mater.* 2005, 14, 86.
- 29. Hupert, M.; Muck, A.; Wang, J.; Stotter, J.; Cvackova, Z.; Haymond, S.; Show, Y.; Swain, G. M. *Diamond and Related Materials*, 2003, 12, 1940.
- 30. McCreery, R. L. In *Laboratory Techniques in Electroanalytical Chemistry*, 2nd ed.; Kissinger, P. T., Heineman, W. R., Eds.; Dekker: New York, 1996, Chapter 10.
- 31. Chen, P.; McCreery, R. L. Anal. Chem. 1996, 68, 3958.
- 32. Osswald, S.; Yushin, G.; Mochalin, V.; Kucheyev, S. O.; Gogotsi, Y. J. Am. Chem. Soc. 2006, 128, 11635.
- 33. Yoshikawa, M.; Mori, Y.; Maegawa, M.; Katagiri, G.; Ishida, H.; Ishitani, A. Appl. Phys. Lett. 1993, 62, 3114.
- 34. Yoshikawa, M.; Nagai, M.; Matsuki, M.; Fukuda, H.; Katagiri, H.; Isida, H.; Ishitani, A. *Phys. Rev. B* 1992, 46, 7169–7174.
- 35. Yoshikawa et al. Appl. Phys. Lett. 1995, Vol. 67, No. 5.
- 36. Krüger, A.; Kataoka, F.; Ozawa, M.; Fujino, T.; Suzuki, Y.; Aleksenskii, A. E.; Ya. Vul', A.; Osawa, E. *Carbon*, 2005, 4, 1722–1730.
- 37. Anjo, D. M.; Kahr, M.; Khodabakhsh, M. M.; Nowinski, S.; Wanger, M. *Anal. Chem.* 1989, *61*, 2603-2608.
- 38. Beilby, A. L.; Sasaki, T. A.; Stem, H. Y. Anal. Chem. 1995, 67, 976-980.
- 39. Angus, J. C.; Hayman, C. C. *Science*, 1988, 241,913.
- 40. Fischer, A. E.; Show, Y.; Swain, G. M. Anal. Chem. 2004, 76, 2553-2560.

- 41. Granger, M. C.; Witek, M.; Xu, J.; Wang, J.; Hupert, M.; Hanks, A.; Koppang, M. D.; Butler, J. E.; Lucazeau, G.; Mermoux, M.; Strojek, J. W.; Swain, G. M. *Anal. Chem.* 2000, 72, 3793.
- 42. Philip, J.; Hess, P.; Feygelson, T.; Butler, J. E.; Chattopadhyay, S.; Chen, K. H.; Chen, L. C. *Journal of Applied Physics* 2003, Vol 93, No 4.
- 43. Xu, J.; Granger, M.C.; Chen, Q.; Strojek, J.W.; Lister, T.E.; Swain, G.M. *Anal. Chem.* 1997, 69, p. 591A.
- 44. Wang, S.; Swope, V. M.; Butler, J. E.; Feygelson, T.; Swain, G. M. Diamond & Related Materials 2009, 18, 669–677.
- 45. Wu, C.Q.; Fu, R.T.; Li, Z.Q.; Kawazoe, Y. J. Phys: Condens. Matter 1997, 9, p. L351.
- 46. Kim, D. Y.; Merzougui, B.; Swain, G. M.; Chem. Mater. 2009, Article ASAP.
- 47. Silverstein, R. M.; Morrill, T. C.; Bassler, G. C. *Spectrometric Identification of Organic Compounds*, John Wiley & Sons, Newyork, 1981, 4th edition.
- 48. Struck, L. M.; Evelyn, M. P. D. J. Vat. Sci. Technol. 1993, A11, 1992.
- 49. Jiang, T.; Xu, K. Carbon, 1995 Vol. 33, No. 12, pp. 1663-1671.
- 50. Sappok, R.; Boehm, H. P. Carbon, 1968 6, 283.
- 51. Hu, I.; Karweik, D. H.; Kuwana, T. J. Nectroanal. Chem. 1985, 788, 59.
- 52. Fieser, L. F. Science, 1924, 60, 48.

Chapter 5

The Corrosion Resistance and Electroactivity of Pt-Loaded High Surface Area Conductive Diamond Powder for Oxygen Reduction

5.6 Introduction

As described in Chapter 1, there are several material problems that need to be overcome in current fuel cell technology. Minimization of the loading of electrocatalytic metals (mainly platinum or Pt-based alloys) while maintaining high electrocatalytic activity is one challenge [1-9]. A related problem is how to maintain high activity over the projected lifetime of the cell (~5000 h for mobile power applications). Another problem is electrocatalyst support degradation.

A way to address the loading problems is to disperse the electrocatalyst as small particles on a high surface area (> 100 m²/g) support material. This leads to a large number of reaction sites per weight of catalyst. In addition to a high surface area, an electrocatalyst support must also have sufficient electrical conductivity (>0.5 S/cm) so that the support can act as a path for the flow of electrons. Moreover, chemical stability in aqueous environments, thermal stability up to 200 °C, and morphological and microstructural stability at high potentials (e.g. >1 V vs. the standard hydrogen electrode (RHE)) and current densities are essential properties [10].

Figure 5.1 pictorially represents the carbon corrosion process that can occur at the cathode during PEMFC operation. Electrochemical corrosion of the carbon support leads the agglomeration and sintering of the Pt catalyst particles (i.e, decreased electrochemical surface area (ECSA) of the catalyst). Corrosion of the support also leads to reduced particle-particle contact, which increases the ohmic resistance through the layer. Ultimately, corrosion reduces

Carbon Surface Area Decrease Carbon Support

Platinum Particles

e 5.1. Schematic representation of the effect of carbon corrosion on agglomeration and

loss of Pt particles and ohmic resistance in the membrane electrode assembly (MEA) during PEMFC operation.

the operational efficiency of the PEMFC [11-14]. In pact, due to support corrosion, the life time of the fuel cells in transportation applications leads short of the mandated 5000h [15].

There has been a considerable work over the years on the development of carbon supports ranging from the traditional blacks to various forms, treatments, surface modifications, and preparation protocols [16-21]. Among these alternative materials, UNCD powder possesses properties well suited for an electrocatalyst support for fuel cells. It has high surface area (~300 m²/g), superior morphological stability and corrosion resistance compared to conventional sp² carbon support materials [22-24]. It is chemically inert enabling its use at elevated temperatures in oxidizing or reducing media without loss of properties.

In order to use diamond as a support material, it needs to be conductive and methods should be developed for efficient decoration of the outer surface with catalytically-active metal nanoparticles. High surface area forms (300-3000 m²/g) of diamond are commercially available but none posses intrinsic electrical conductivity. Our approach for impacting conductivity to

diamond is to coat inexpensive insulating diamond powder with a layer of boron-doped ultrananocrystalline diamond (B-UNCD). In prior work, we reported 50 m²/g specific surface area and ~1 S/cm electrical conductivity for B-UNCD-coated 100 nm diam. particles [24].

Previously, we investigated oxidation resistance of bare and Pt-coated electrically conducting diamond powder by thermogravimetric analysis (TGA) and results were compared with bare and platinized Vulcan powder [25]. The oxidation onset temperature for B-UNCD-D powder decreased with the Pt loading (0 to 30 wt % (Pt/C)) from 620 to 558 $^{\circ}$ C. However, compared with the bare powder, the rate of carbon consumption was significantly greater for Pt-Vulcan as compared to the platinized diamond powder. For example, the temperature of the maximum carbon consumption rate, $T_{\rm d}$, occurred at 426 $^{\circ}$ C for Pt-Vulcan (20% Pt/C) which was 295 $^{\circ}$ C lower than the $T_{\rm d}$ for bare Vulcan. In contrast, $T_{\rm d}$ for Pt-B-UNCD-D (20% Pt/C) was 558 $^{\circ}$ C; a temperature that was only 62 $^{\circ}$ C lower than that for bare diamond. Isothermal oxidation at 300 $^{\circ}$ C for 5 h produced negligible weight loss for Pt-UNCD-D (20% Pt/C) while a 75% weight loss was observed for Pt-Vulcan (20% Pt/C). The results clearly demonstrate that platinized diamond is more resistant to gas phase oxidation than is platinized Vulcan at elevated temperatures.

In this chapter, the electrochemical performance and stability of, 100 nm and 3-6 nm diam. diamond powders overcoated with a layer of boron-doped ultrananocrystalline diamond and loaded with nanoscale Pt particles is described. The Pt particle size was determined by HRTEM. The catalytic activity of platinized diamond powder was evaluated by a rotating disk voltammetry (RDV). Rotating disk voltammetry is commonly used to study this reaction,

because it allows for the separation of the mass-transfer from the electron transfer kinetic parameters, and provides a measurement of the true catalytic activity [26]. Analysis of the oxygen reduction reaction kinetics in acidic media (0.5 M H₂SO₄ at 80 °C and 0.1 M HClO₄ at room temperature) was performed via cyclic and linear sweep voltammetry. The kinetic parameters (e.g., specific and mass activities) were determined as a function of the support material surface area. The corrosion resistance of the electrode was tested during anodic polarization at 1.4 V vs. RHE for 1 h in 0.5 M H₂SO₄ at 80 °C by characterizing the change in hydrogen adsorption/desorption (HAD) change and the shift in the half-wave potential for oxygen reduction.

5.7 Results

5.7.1 Physical and Chemical Characterization

For the 100 and 3-6 nm diam. diamond powders, the nominal Pt particle size was determined from HRTEM images. Micrographs of platinized diamond powders, as well as a histogram of the Pt particle size distribution are presented in Figure 5.2. The particle size analysis was performed on 100 single particles. Due to the larger atomic mass of Pt, it appears darker than the carbon atoms of diamond in the bright field images.

Images of the 100 nm diam. revealed that the Pt particles are homogeneously distributed over the conductive diamond powder surface. There are some regions where Pt agglomerates formed (10-30 nm clusters) but, for the most part, individual Pt particles decorate the powder surface. High Pt loadings were achieved with our method. AAS analysis revealed a ~17 wt. % Pt content (Pt/C) in the Pt-B-UNCD-D powders (compared to the theoretical 20 wt. %). EDX analysis confirmed that the dark spots are indeed Pt particles. The particles decorate both the

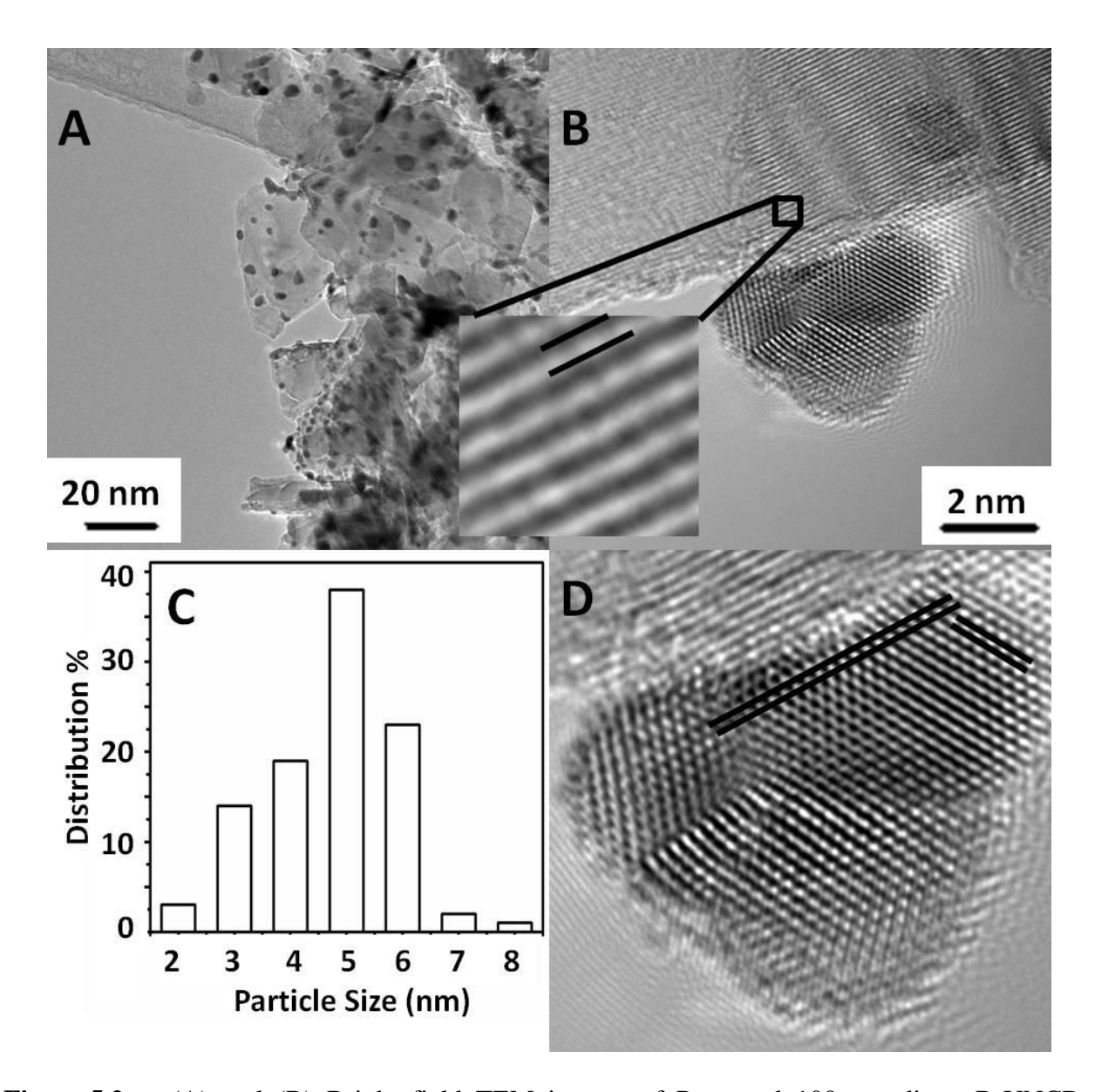


Figure 5.2. (A) and (B) Bright field TEM images of Pt-coated 100 nm diam. B-UNCD-diamond powder. (C) A histogram of the Pt particle size distribution on the 100 nm diamond powder. The data set includes measurements of 100 Pt particles. (D) HRTEM image of a Pt nanoparticle attached to the 100 nm diamond powder.

edges and the face sides of the diamond powders. This histogram in Fig. 5.2C reveals a particle size of around 5 nm. The nominal particle diameter average was determined to be 4.4 ± 1.4 . The light contrast lines belong to the (111) crystallographic diamond planes, which are separated by a

distance of 0.206 nm as observed in Fig. 5.2B. In Fig 5.2D the labeled crystalline region of a Pt nanoparticle has spacing of the atomic rows of high density atoms, which appears to be side view of (200) layers with spacing of 1.96 Å and (111) lattice with spacing about 2.6 Å which is slightly higher than the bulk platinum spacing (2.26 Å). We believe this is caused by stress at the bonding between diamond and platinum. Pt particle (111) crystal face continue to grow on (111) diamond surface epitaxially which might be indication of the chemical bond between Pt and diamond particle. HRTEM images provide insight on the nature of the sites at which Pt deposits on diamond. The image (Fig. 5.2B and 5.2D) reveals that the Pt atom directly contacts, and presumably bonds to, the carbon atoms of diamond. More importantly, there is no interfacial layer seen between the Pt and diamond, such as graphite or diamond-like carbon.

It is more difficult to resolve Pt particles on the smaller 3-6 nm diam. powders. TEM and HRTEM images of the Pt-coated powders are presented in Fig. 5.3A and 5.3B, respectively. After coating, there is a considerable increase in the size of most of the seed particles with quite a bit of variability. Based on the variable particle size across the image, there are undoubtedly some regions where the rate of UNCD growth on the diamond powder substrate is higher than others. After UNCD coating, the diamond powder had a specific surface area of 170 m²/g. The specific surface area of powders decreases by ca. 30-50% after UNCD overcoating due to particle–particle fusion and coating of multiple particles. This is consistent with the TEM image shown in Fig. 5.3A, which reveals extensive particle–particle fusion and a corresponding increase in the particle size. EDX analysis confirmed that the dark spots in Figure 5.3A and 5.3B are indeed Pt particles. The particles decorate the edges, the face sides and grain boundaries of the diamond powders.

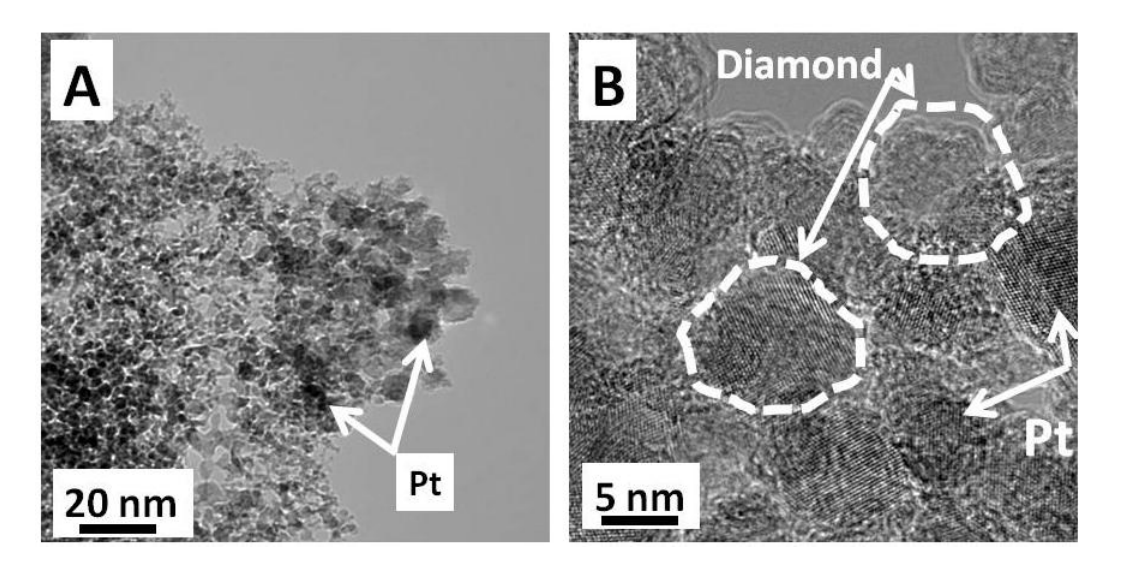


Figure 5.3. (A) TEM and (B) HRTEM images of Pt coated 3-6 nm diam. Boron-doped ultrananocrystalline diamond powder.

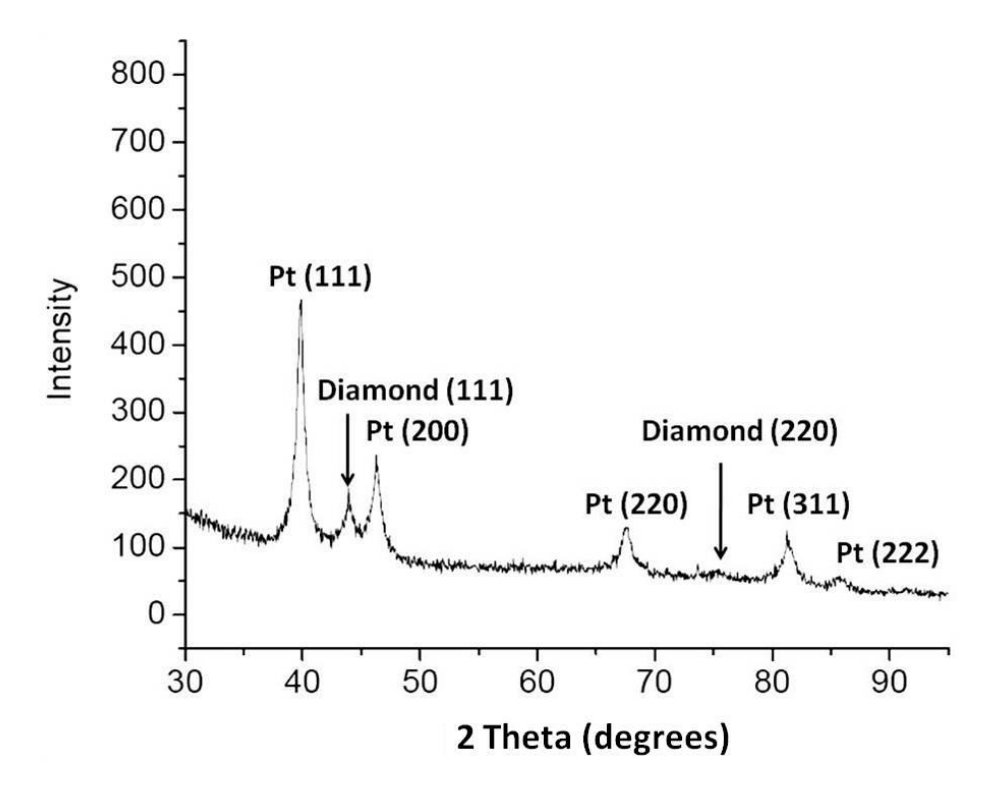


Figure 5.4. XRD pattern for 20 wt. % Pt-loaded B-UNCD-diamond powder. The diamond particles coated were 3-6 nm diam.

A typical XRD spectrum for the Pt-loaded B-UNCD-coated diamond powder is shown in Figure 5.4. The pattern shows characteristic reflections for Pt and diamond with a significant diamond (111) reflection at ca. 44° . The supported Pt forms a face centered cubic (fcc) structure and has major peaks at 2θ values of 39.7° (111), 46.2° (200), 67.4° (220), and 81.2° (311). The average Pt particle size was calculated from the line width and position of the Pt (111) peak using the Debye-Scherrer equation [27].

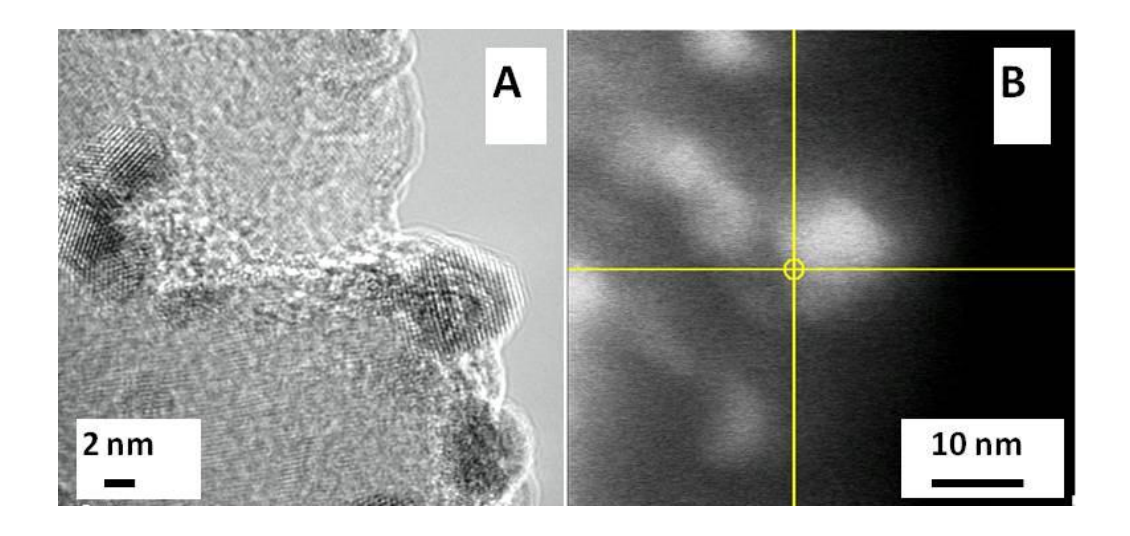
$$L = \frac{0.9\lambda_{K\alpha 1}}{B_{(2\theta)}\cos\theta_{max}}$$
 [5.1]

where L is the average diameter of the crystallites, λ the Cu K α X-radiation wavelength (1.5418 Å), B the excess line width (in radians) and θ the Bragg angle. Based on this analysis the average diameter of particles was determined to be 9 nm. This is slightly larger than the 5 nm size determined from TEM. This is expected as the x-ray data are reflection of all Pt particles in the sample including aggregates, while the TEM analysis reflects selected deposits on powder particle surfaces.

5.2.2 Effect of surface chemistry on Pt deposition

Before the platinum deposition, the B-UNCD-diamond powder was acid washed. This step is necessary to remove sp² bonded carbon impurities during overcoating. In addition to cleaning the powder sample, these chemical treatments produce an oxygen-terminated surface. The oxidized powders were used for Pt deposition as were oxidized powders that were rehydrogeneted in hydrogen plasma. The re-hydrogenation procedure involved stopping the CH₄

and B_2H_6 gas flows, while leaving the sample exposed to a H_2/Ar plasma for 10 min at 400 $^{\circ}C$. At these conditions, the hydrogen surface termination is stable and this adlayer serves to keep the surface carbon atoms in an sp³-hybridized bonding state. Figure 5.5A shows a representative HRTEM of the H-terminated Pt-coated, B-UNCD-diamond powder. The Pt particles are approx 2-5 nm in diameter. Both the lattice lines of the diamond and Pt are visible with no sp² carbon detectable in the image. Scanning transmission electron microscopy (STEM) was combined with electron energy loss spectroscopy (EELS) to probe the interface between the Pt and the support. The advantage of STEM over traditional TEM is the ability to precisely place the e-beam on a fixed point of the sample since the beam position can be manipulated with the scan coils. Because the STEM bright field detector physically blocks the EELS detector and must be removed, dark field images are collected in this mode, making higher atomic mass elements appear brighter than lighter elements. An electron beam spot size of 0.7 nm in diameter gave the best combination of spatial resolution and signal/noise for EELS. The shape of the EELS spectrum is reflective of diamond along with a little signal intensity $C(1s) \to \pi^*$ of graphite at 284-285 eV (Fig. 5.5C solid line) The peak maximum is centered at 287 eV instead of 285 eV [28-32] The peak at 287 eV is indicative of the C (1s) $\rightarrow \sigma^*$ of C-H bonds which lie close in energy to the C (1s) $\rightarrow \sigma^*$ transition for the sp³ bonds of diamond observed at 290 eV. The σ^* transition for C-H bonds at ca. 287 has been reported by Hoffmann et al. using NEXAFS studies of photon-stimulated desorption of hydrogen from diamond, and from Comelli et al. who observed a peak at 287.5 eV in the NEXAFS spectrum of cyclohexane [33-35]. The peak at 287 eV for H-terminated Pt-B-UNCD-diamond powder is unexpected but not unreasonable. Though



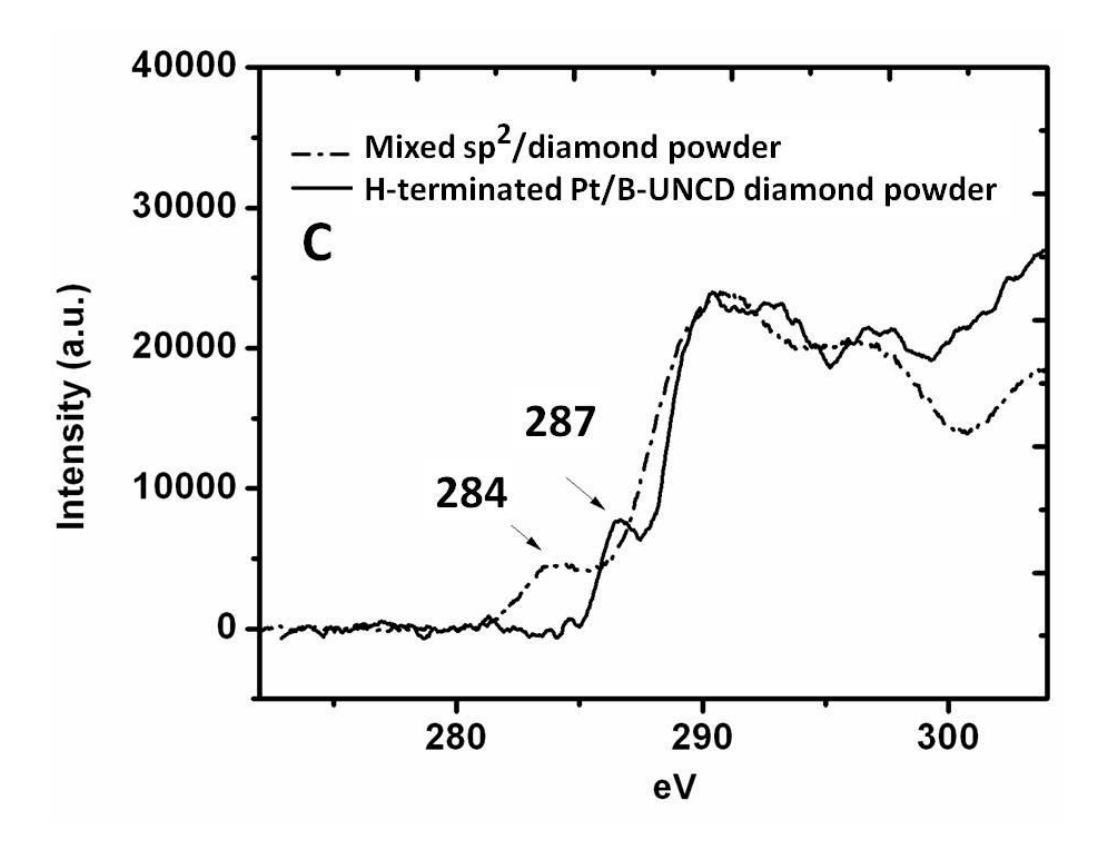


Figure 5.5 A representative bright-field HRTEM image (Fig A) of H-terminated Pt/B-UNCD-diamond powder, and a dark field STEM image (Fig B) of the EELS collection spot indicated by cross hairs. The diamond powder was 100 nm diameters. Both micrographs are from the same area of the sample. (C) EELS spectrum of H-terminated 100 nm Pt/B-UNCD-Diamond powder (solid line). The spectrum from is overlaid with a EELS spectrum from a mixed phase sp²/ 100 nm diam. diamond powder (dash line).

normally not observed in EELS of diamond or diamond powders, here the freshly hydrogenated diamond surface and small 0.7 nm electron beam spot size through a thin (< 10nm) section means the hydrogen-carbon ratio is likely much higher than in most diamond samples. To better determine the changes that mixed phase sp²/sp³ content has on the EELS spectrum for the 100 nm diamond powder, a spectrum was also collected for 100nm diamond powder but mixed with a small amount of amorphous carbon. These differences are demonstrated in Figure 5.5C, where the same EELS spectrum recorded from Pt-decorated diamond powder is overlaid with that of mixed phase sp²/diamond powder. There are two notable differences in the spectra. The mixed phase powder has a peak at 284 eV for the $\pi \rightarrow \pi^*$ transition of graphite while as previously discussed the H-terminated Pt-BND powder has a peak at 287 eV more consistent with a σ transition for C-H. The rise for the sp³ carbon σ - σ * transition peak at 290 eV is still sharp and well defined for the H-terminated Pt-BND as expected for phase-pure diamond, compared to the more gradual rise to the σ peak at 290 eV for the sp²/diamond mixed phase due to the greater disorder in the carbon microstructure. From HRTEM and EELS data, we conclude that the Pt nanoparticles attach directly to sp³ carbon sites with no sp² carbon interfacial phase.

5.2.3 Electrochemical Characterization

The Pt-loaded B-UNCD powders were electrochemically characterized by cyclic voltammetry and rotating disk voltammetry using a GC/diamond powder electrode. The Pt/B-UNCD-diamond powder (3-6 nm) electrode was initially conditioned in 0.1 M HCIO₄ by potential cycling between -0.050 and 1.4 V vs. RHE. This conditioning cleans and activates the Pt. Figure 5.6

shows a background cyclic voltammetric *i-E* curves for a Pt/B-UNCD-diamond powder electrode over 50 cycles. The potential sweep rate was 5 mV/s and the sweeps were initiated at 0.2 V and scanned in the positive direction. For the first cycles the characteristic hydrogen adsorption/desorption peaks for polycrystalline Pt were not clearly resolved. It is probable that the Pt surface is initially blocked by adsorbed contaminants from Nafion solvent. The contaminants appear to be effectively removed by cycling, as well resolved peaks developed after a short period, as seen in the figure. The resulting voltammetric features are all characteristic of polycrystalline Pt with

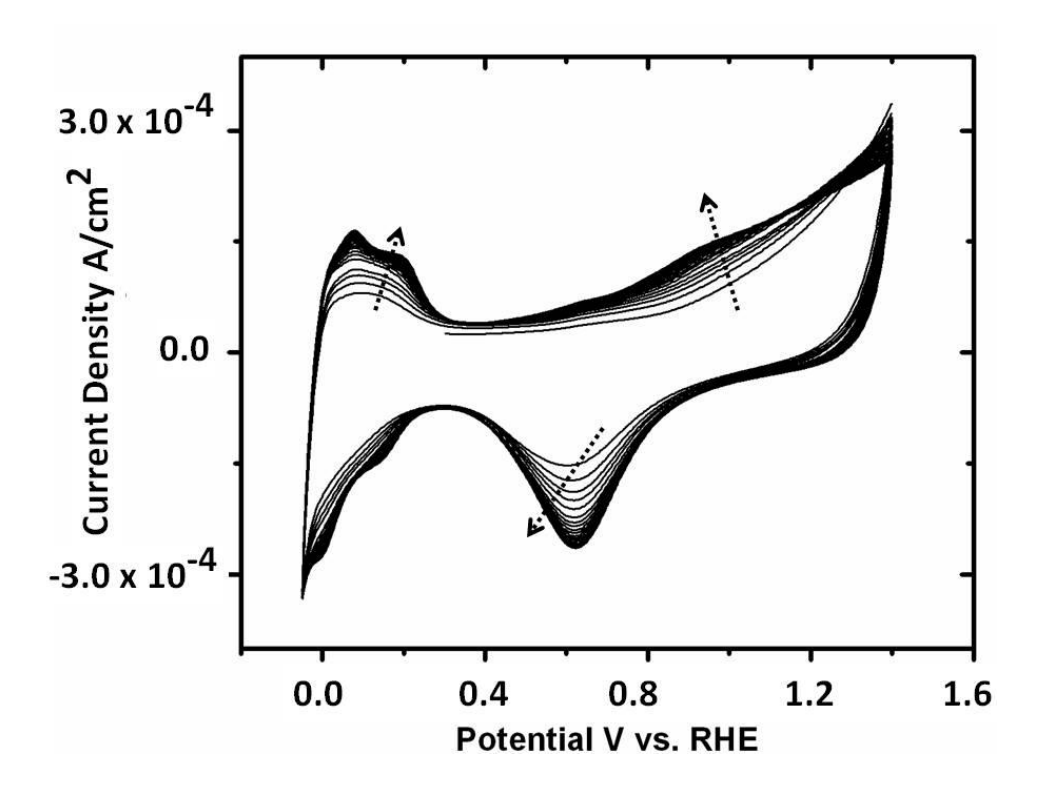


Figure 5.6. Cyclic voltammetric i-E curves in 0.1 M HClO $_4$ for a Pt/B-UNCD-diamond powder (3-6 nm diam.). Fifty potential cycles between -0.05 and 1.4 V vs. RHE are shown. Dashed arrow show the increase in current response with scan number. Potential scan rate=5mV/s

Table 5.1. Comparison of Pt nanoparticles properties on different support materials.

Diamond Support	20 wt. % Pt/C 100 nm diamond	20 wt. % Pt/C 3-6 nm diamond	20 wt. % Pt/C Vulcan XC-72	
Support BET (m ² /g)	52	170	235	
Pt Particle Size (nm)	4-5 4-5		2-3	
Pt Active Surface Area (cm ²)	~38	~60	75	
ORR E _{1/2} (V)	0.78	0.79	0.85	
Mass Activity (mA/mgPt)	40	90	110	
Specific Activity (μΑ/cm ² Pt)	102	138	170	

the Pt oxide formation and oxygen evolution at potentials positive of 0.8 V, the reduction of Pt oxide at ca. 0.6 V, the adsorption and desorption of hydrogen between 0 and 0.2 V, and the double layer charging region between ca. 0.2 and 0.4 V. An increase in the cathodic current is observed at potentials below 0.85 V, accompanied with the reductive removal of the Pt oxide, in agreement with the fast ORR kinetics on oxide-free Pt surface [42]. The cathodic current reaches a maximum of -0.26 mA/cm² at ca. 0.60 V, and decays rapidly on the low potential side of the peak due to the depletion of oxygen at the electrode surface (diffusion-controlled). Compared to the 100 nm Pt-loaded diamond powder, the capacitive current was greatly increased for 3-6 nm Pt-loaded diamond powder (Figure 5.9A) due to the significantly larger BET area.

Integration of the oxidation charge associated with desorption of hydrogen (0 - 0.2 V) was used to calculate the electrochemically-active Pt surface area (ECAS). By assuming a 1x1

H:Pt surface structure and a full monolayer coverage of active Pt [36, 37], the measured charge yielded a specific surface area of ~60 and 75 cm² for 3-6 nm Pt-B-UNCD-diamond and Pt/Vulcan, respectively. The results are presented in Table 5.1 for the different supports. These features demonstrate the Pt/B-UNCD-Diamond powder contains active Pt particles at the surface that are in good electronic communication with the current collecting RDE through the B-UNCD powder.

5.2.4 Oxygen Reduction Reaction

The oxygen reduction reaction kinetics on the oxide-free Pt surface were assume to be limited by mass transport of dissolved oxygen to the electrode surface. The oxygen reduction activity was quantified for Pt/B-UNCD-diamond powders at different rotation rates in 0.1 M HClO₄. Typical linear sweep voltammetric i-E curves are presented in Figure 5.7. All the curves were recorded during the cathodic potential sweep starting at 1.0 V. Well-defined, limiting current plateaus are seen, particularly at low rotation rates. The i-E curves have been background corrected using similar measurements in a nitrogen-purged solution. Solution resistivity was evaluated by increasing redox system concentration and the i-E curves have been corrected for solution resistivity, as well. The current density, i, for the reduction of oxygen on a rotating disk electrode is related to the kinetic current density, i, and the diffusion limited current density, i, determined by the mass-transport properties of the RDE. For a first-order reaction mechanism, the limiting current is proportional to the concentration of dissolved oxygen and the square root of the rotation rate, as predicted by the Levich equation [26].

$$i_L = 0.2 \text{nFAD}^{2/3} v^{-1/6} C_0 \omega^{1/2} = BC_0 \omega^{1/2}$$
 [5.2]

where D and υ are the oxygen diffusion coefficient (1.8 x 10^{-5} cm²/s) and the kinematic viscosity of the electrolyte solution (0.0087 cm²/s), respectively [38]. C_o is the concentration of the dissolved oxygen assumed to be (1.26 x 10^{-3} mol/L) [39], and ω represents the rotation rate (rad/s). The electrode area was 0.07 cm² in all measurements.

For the Nafion-coated powder electrodes, an additional mass-transport resistance might be considered since there are two-layers of diffusion (oxygen diffusion in the Nafion layer and boundary-layer diffusion in the electrolyte). However, it was shown that the Nafion film, which is used to bind the powder particles to the RDE, can be made sufficiently thin ($<0.2 \mu m$) such that the Nafion film resistance for diffusion becomes negligible [40].

$$\frac{1}{i} = \frac{1}{i_L} + \frac{1}{i_k} \tag{5.3}$$

Plotting i⁻¹ vs. $\omega^{-1/2}$ yields a y axis intercept equal to i_k⁻¹ and slope equal to B⁻¹. Koutecky-Levich plots for ORR on a Pt/B-UNCD-diamond powder in 0.1 M HClO₄ are presented in Figure 5.7B. These plots were constructed from the current values at 0.7, 0.8, 0.85, and 0.9 V in the polarization curves shown in Figure 5.7A. All the plots are straight lines with the similar slope at higher overpotential. For lower overpotentials (0.85 and 0.9 V) the slope increases, which is the indication of sluggish electron transfer. The y-intercept (1/i_k) is 0.05 for 0.7 V, 0.11 for 0.8 V, 0.25 for 0.85 V and 0.76 for 0.9 V, respectively. The corresponding slopes (1/B) are 72.7, 70.4, 103.4 and 199.2 mA⁻¹.rpm^{1/2} respectively, The B values, 1-1.5 mA·rpm^{-1/2}, are slightly higher than the theoretical value (0.87 x 10⁻² mA . rpm^{-1/2}

 $^{1/2}$) for higher over potentials (0.7-0.85) for 4-electron reduction pathway of ORR. This might be due to high surface area of powder (e.g., roughness). The geometric area of the electrode (0.07 cm²) is less than the active area of platinum particles. For lower overpotential (0.9 V), calculation was performed for the n using the slope of the plot. The n value of 2.3 was obtained at scan rate 5mV/sec for 0.9 V.

The kinetic current (y-intercept) was used to calculate the specific (SA) and mass activity (MA) of the electrocatalyst. The mass activity (i_{mv} mA/mgPt) was calculated by dividing kinetic current at 0.9 by the Pt loading (0.14 mgPt/cm²) (Equation 5.4). The specific activity (μ A/cm²) was determined by normalization of kinetic current to the Pt surface area (cm²/gPt) and the Pt loading (Equation 5.5)

$$i_{m}(mA/mg_{Pt}) = \frac{Kinetic Current (mA)}{Pt Loading (mg_{Pt})}$$
 [5.4]

$$i_{S}(\mu A/cm^{2}) = \frac{\text{Kinetic Current (A)}}{\text{Pt Surface Area } \left(\frac{cm^{2}}{g_{Pt}}\right)x \text{ Pt Loading}(g_{Pt})}$$
 [5.5]

The kinetic parameters, the exchange current densities and Tafel slopes, were obtained from mass-transfer-corrected Tafel plots (log i $vs. \eta$). The overpotential for the oxygen reduction, η , was determined by subtracting the equilibrium potential of ORR on Pt (1.23 V vs. RHE), from the applied potential, E_{app} . The kinetically-controlled currents were calculated using Equation 5.3, $i_k=i_Li/(i_L-i)$. The current densities were normalized to the geometric area of the electrodes. Figure 5.8 shows the set of Tafel plots constructed from the polarization curves at 500 rpm rotation rate. The plots for different rotation rates overlap and two distinct Tafel slopes are

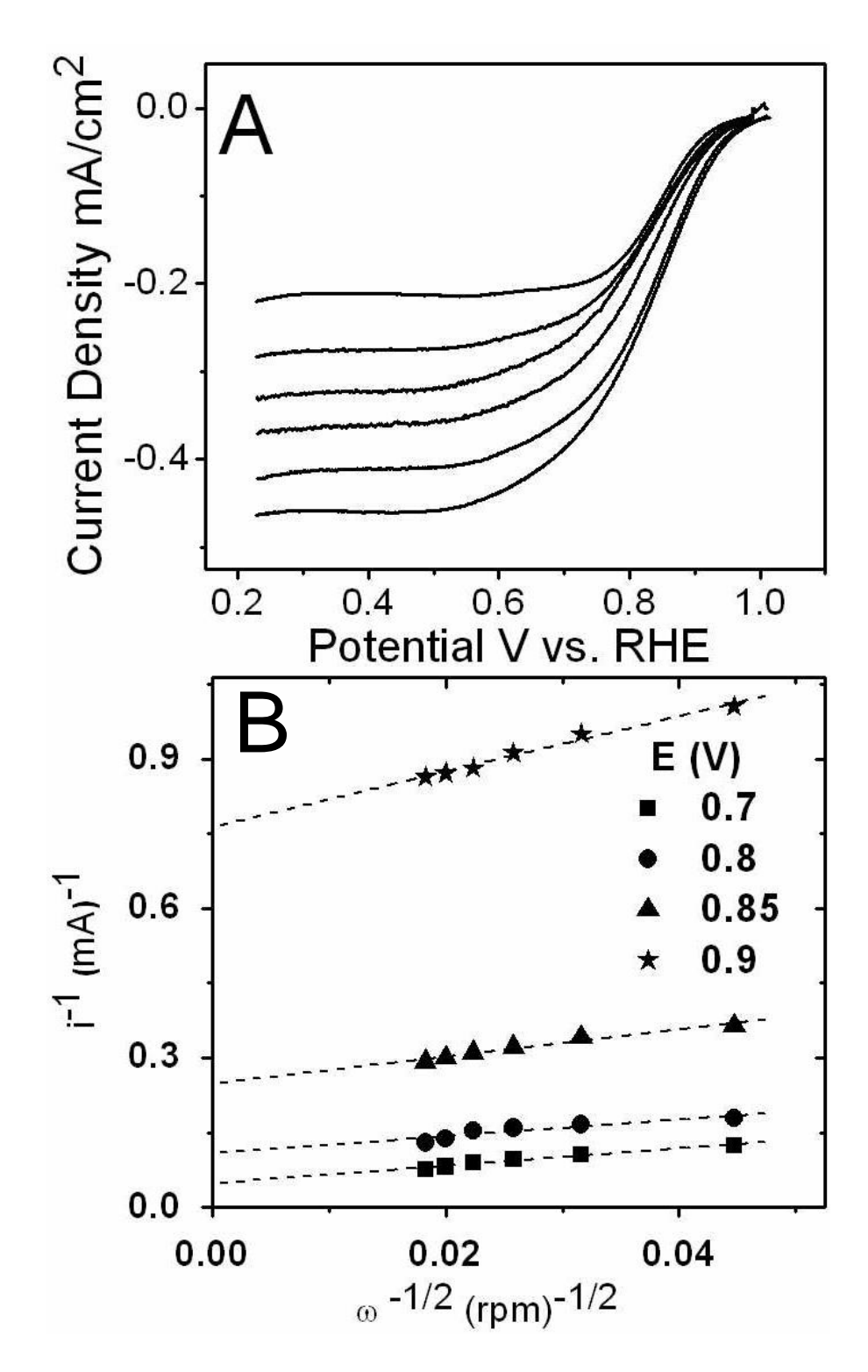


Figure 5.7. (A) Oxygen reduction current densities on 20% Pt/B-UNCD-diamond powder (3-6nm) supported on a glassy-carbon disk electrode. (B) Koutechy-Levich plots for the oxygen reduction reaction. Data taken from the LSV results shown in (A). Rotation rate of 500-3000 rpm were used and the measurements made in 0.1 M HClO₄ at room temperature. Scan rate=5mV/s.

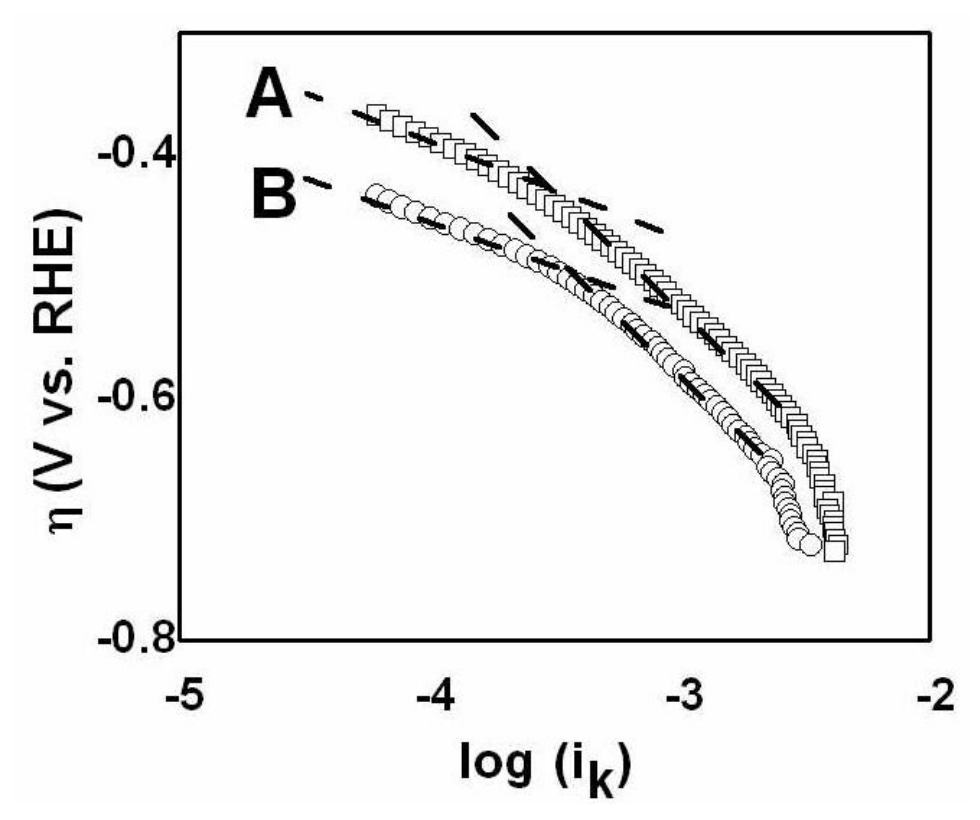


Figure 5.8. Tafel plots for the oxygen reduction reaction in 0.1 M HClO₄ for (A) Pt/Vulcan and (B) 3-6 nm Pt/B-UNCD-diamond powder. Data taken from the polarization curves at a 500 rpm rotation rate.

observed. The break in the Tafel plot, which occurs at an overpotential between -0.50 and -0.60 V, has been previously reported and interpreted as a change in the oxygen chemisorption mechanism [37, 38]. At low overpotentials, the Pt surface is completely or partially covered with oxide film. It has been reported that, a low Tafel slope of -60 mV/dec (2.3RT/F) is accounted for by assuming oxygen chemisorption under Temkin conditions in the potential range of oxide formation [49, 50]. At high overpotentials, the coverage of adsorbed oxygen-containing species becomes negligible, and a high Tafel slope of -120 mV/dec (-2 x 2.3RT/F) corresponds to a potential regime where oxygen reduction is under Langmuirian conditions [49, 50]. However, it was proposed by Perry et al. [44] showed that in the flooded-agglomerate model (Nafion layer on

the platinized powders), a double Tafel slope and first-order kinetics in oxygen partial pressure can be observed in a potential region where oxygen reduction is controlled by kinetics and diffusion of dissolved oxygen and a quadruple Tafel slope and half order kinetics in a region where oxygen reduction is controlled by kinetics, the diffusion of dissolved oxygen, and ionic transfer. The Tafel slopes in the Fig 5.8, can be partially considered by the flooded-agglomerated model. The lower overpotential region (above -0.50 η) correspond to the double Tafel slopes and the slope at below -0.50 η to the quadruple Tafel slopes. The kinetic data for each region were independently analyzed and the exchange current density corresponding to each Tafel slope was calculated by extrapolating the potential to $\eta = 0$, (i.e. the equilibrium potential). As shown in Table 5.2, for a Tafel slope of -110 mV/dec at low overpotentials for ORR in 0.1 M HClO₄, the exchange current densities, i₀, is 1.14 x 10⁻¹⁰ A·cm⁻² for Pt/B-UNCD-diamond powder.

5.2.5 Corrosion Test

The corrosion resistance of platinized B-UNCD-coated diamond powder (100 nm) was tested by anodic polarization at 1.4 V vs. RHE in 0.5 M H₂SO₄ for 1 h at 80 °C. The Pt morphology before and after the oxidation treatments was examined by transmission electron microscopy (TEM). Figure 5.9 shows cyclic voltammetric *i-E* curves before and after the polarization.

For the Pt/B-UNCD-diamond powder, the characteristic Pt features did not change significantly after the polarization. The active Pt surface area decreased slightly; however, clearer hydrogen adsorption/desorption region was observed with 2 adsorption peaks. This indicates a mixed crystal structure of the platinum [45]. Before polarization the cyclic

Table 5.2. Comparison of the kinetics parameters for ORR at the Pt/B-UNCD-diamond with the literature data reported for single crystal, polycrystalline, and carbon supported Pt at room temperature.

Electrocataliyst	Tafel Slope (-mV/dec)	i _o (A·cm ²)	Reference
Pt(111)	65	2.20 x 10 ⁻¹⁰	41
Pt(110)	65	3.40×10^{-10}	41
Pt(100)	65	4.60×10^{-10}	41
Bulk Platinum	70	2.00×10^{-11}	42
20 wt. Pt/Vulcan	65 123	1.70×10^{-10} 2.80×10^{-7}	43
20 wt. Pt/Vulcan	141 312	4.02×10^{-10} 2.98×10^{-8}	This work
20 wt. Pt/B- UNCD-diamond (100 nm)*	106 432	5.30 x 10 ⁻¹¹ 1.58x 10 ⁻⁷	This work
20 wt. Pt/B- UNCD-diamond (3-6 nm)*	109 211	1.14 x 10 ⁻¹⁰ 7.27 x 10 ⁻⁹	This work

^{*20} wt. % is the theoretical loading. Measurements of Pt loading revealed levels of ~ 17 wt. %.

voltammogram looks like resistive however after anodic polarization the resistivity and peak around 0.6 V is removed. There are multiple reasons for this peak: Nafion binder, $\rm sp^2$ carbon impurity or –OH adsorption [49, 50]. The initial Pt surface areas before the oxidative treatments were examined by CV, and the measured Pt surface areas were 75 and 40 m g 2 Pt for the Vulcan XC-72 and B-UNCD powder, respectively.

The chronoamperometric curves for the Vulcan XC-72 and B-UNCD powders (Fig. 5.10b and 5.10d) show that the B-UNCD powder shows 83% less corrosion current than Vulcan XC-72 under same conditions. Fig. 10 also shows the increased corrosion currents when these two materials are catalyzed with Pt nanoparticles (Fig. 5.10a versus Fig. 5.10b and Fig. 5.10c

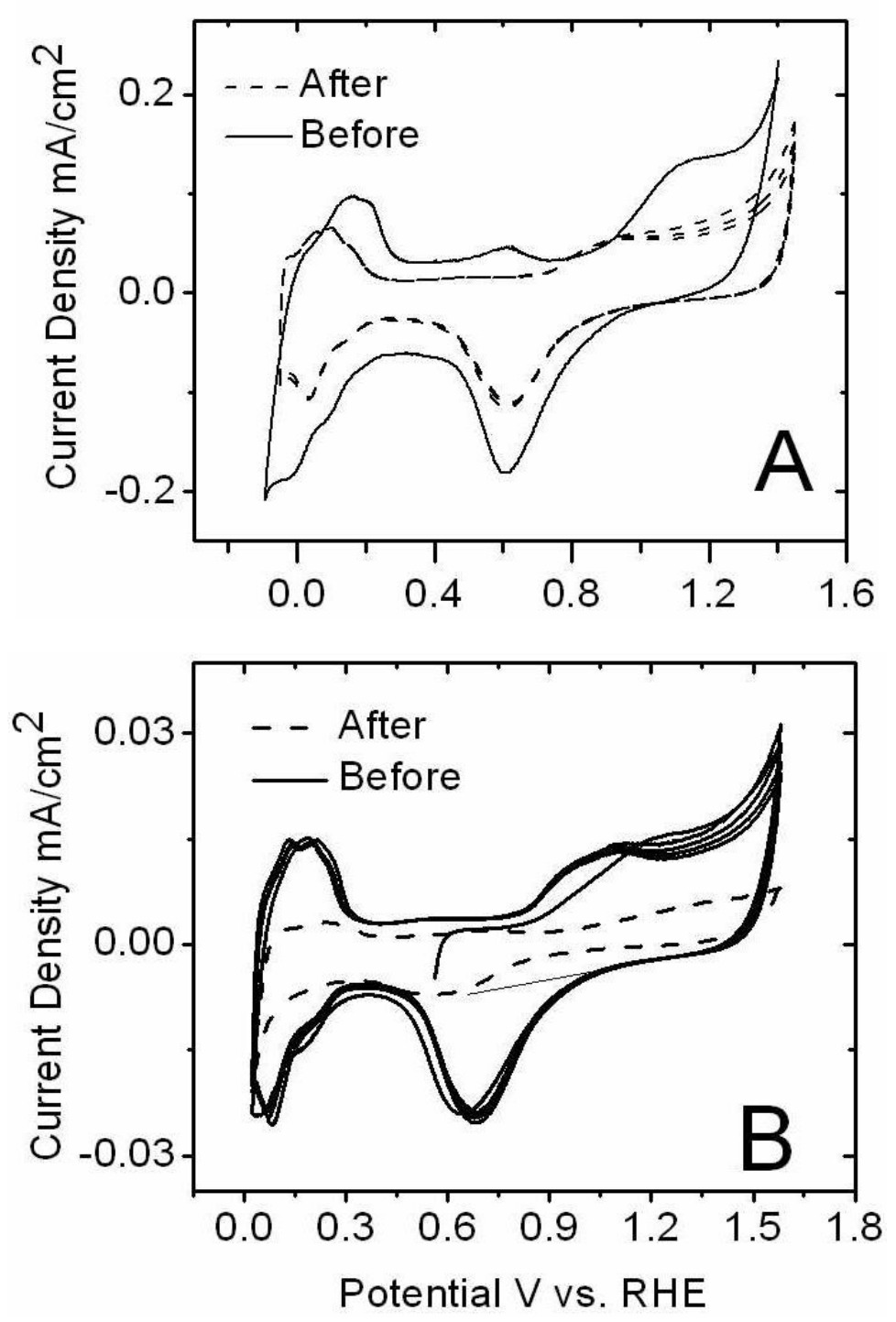


Figure 5.9. Cyclic voltammetric *i-E* curves for (A) Pt/B-UNCD-diamond powder (100 nm) and (B) 20 wt. % Pt/Vulcan in 0.5 M $_{2}SO_{4}$ before (solid line) and after (dashed line) anodic polarization at 1.4 V vs. RHE at 80 $^{\circ}C$.

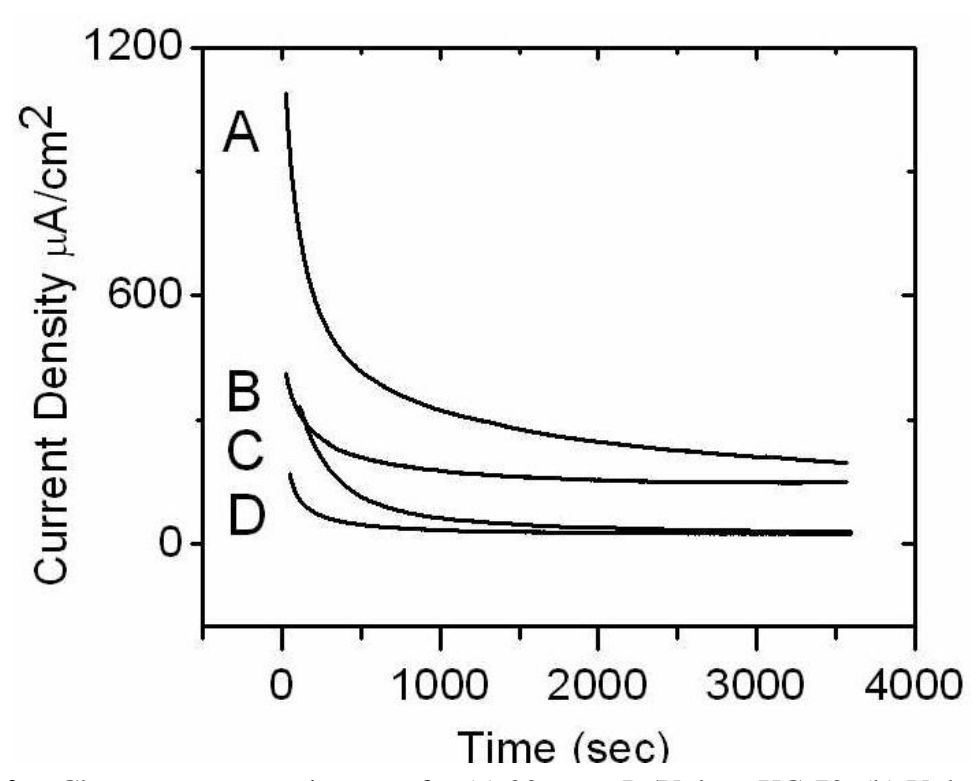


Figure 5.10. Chronoamperometric curve for (a) 20 wt % Pt/Vulcan XC-72, (b) Vulcan XC-72, (c) 20 wt % Pt/B-UNCD-diamond, and (d) B-UNCD, measured at 1.4V vs. RHE 80 $^{\rm o}$ C in N₂ purged 0.5M H₂SO₄.

Table 5.3. Comparison of Pt nanoparticles properties on different support materials before and after anodic polarization at 1.4V vs. RHE.

Diamond Support	100 nm diamond Before Polarization	100 nm diamond After Polarization	20 wt % Pt/Vulcan Before Polarization	20 wt % Pt/Vulcan After Polarization
Pt Particle Size (nm)	4-5	5-7	2-3	4-6
Pt Active Surface Area (cm ²)	~38	~20	75	19
ORR E _{1/2} (V)	0.785	0.740	0.800	0.730

versus Fig. 5.10d). The Pt catalytic effect is less significant for B-UNCD than Vulcan XC-72. The corrosion current is only enhanced by 13% for B-UNCD while 32% for Vulcan XC-72. This suggests that B-UNCD is more stable than

Vulcan XC-72. At this oxidation potential, 11.3% of Vulcan XC-72 for the Pt/Vulcan XC-72 will be lost in approximately 1000 h, while only 2.2% for the case of Pt/B-UNCD-Diamond. It should be mentioned that the B-UNCD powder was acid washed to remove any sp² carbon impurity however, it is not possible to have 100 % pure sp³ bonded diamond. It is likely the amorphous carbon at the grain boundaries in the B-UNCD powder have contributed to the corrosion observed.

Table 5.3 shows the catalytic performance of the platinized powders before and after polarization. The half wave potential shows a decrease after polarization. Half wave potential, defined as the potential at which the measured current reaches the half of the limiting current, was extracted from the voltammogram. As shown in Fig. 5.9, Pt supported on B-UNCD powder and Vulcan XC-72 has similar initial half wave potential. After polarization, Vulcan XC-72 shows a decrease in the activity, evidenced by the lowering of the half wave potential where B-UNCD does not change significantly.

The catalytic activity for ORR was evaluated before and after polarization. The limiting currents for ORR on Pt/B-UNCD-Diamond and Pt Vulcan XC-72 are presented in Fig. 5.11. Since, the Pt surface area decreases after anodic treatment, the limiting currents decrease after polarization for both diamond and Vulcan powder. The major change was observed for Pt/Vulcan powder after polarization. The limiting current decreases ~50% which seems directly related to active surface area of platinum. After 1 h polarization Vulcan supported Pt shows a

decrease in the activity, evidenced by the lowering of the half wave potential. However, B-UNCD exhibits a much slower decrease rate than Vulcan XC-72. This is in agreement with the trend observed for the Pt surface area change.

Pt dissolution and Pt migration and ripening aggregation are two basic reasons for the Pt surface area loss. A simple calculation based on Pt solubility in the 0.5M H₂SO₄ at the specified conditions [46] shows that, only 10% Pt can be dissolved. This suggests that most of the Pt surface area loss is due to the Pt migration and ripening/aggregation, which apparently can be greatly facilitated by carbon corrosion. To understand this phenomenon, the morphology of the Pt before and after the anodic polarization was examined by TEM (Fig 5.2 before Fig.5.12 after). The TEM images for Pt/Vulcan XC-72 before and after anodic polarization can be found in reference 47. The Pt/Vulcan XC-72 before oxidation treatment (at 0.9 V vs. RHE for 168 h at 60 ^oC in 0.5 M H₂SO₄), the Pt nanoparticles show a narrow size distribution with an average size of 2.5 nm. After oxidation treatment, the particle size distribution becomes broader and the average size is around 5-6 nm. We did not observe any corrosion or morphology change in the diamond powders after anodic polarization. Before polarization B-UNCD powder supported Pt particles has larger particle size than Vulcan XC-72 supported Pt (~4nm). After polarization, Pt particle size barely shows any increase in most regions (Figs. (5.12A and 5.12B). However, some aggregation of Pt nanoparticles is observed in some isolated areas on the B-UNCD powder surface as opposed to the uniform aggregation in the case of Vulcan XC-72. The difference in aggregation phenomena in the case of Vulcan XC-72 and B-UNCD is attributed to the higher corrosion resistance of the diamond powder.

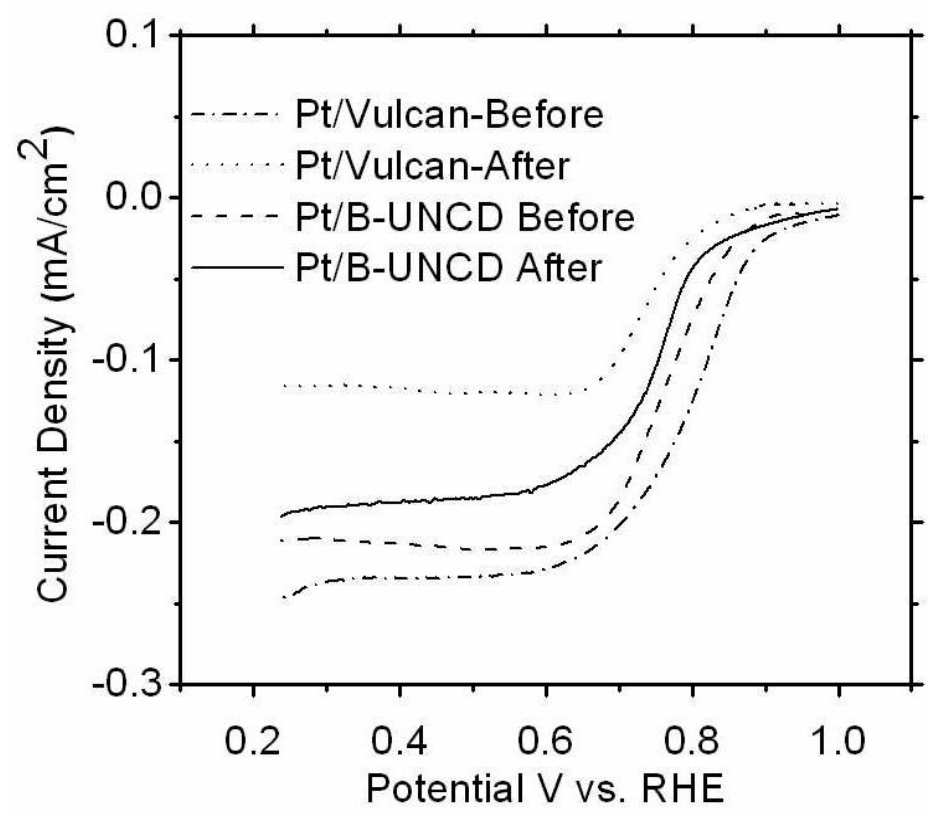


Figure 5.11 Oxygen reduction current densities on 20 wt. % Pt/B-UNCD-diamond powder (100 nm) and 20 wt. % Pt/Vulcan XC-72 before and after anodic polarization at 1.4 V vs. RHE. Operating conditions: sweeping rate 5mV/s, rotating rate 1500 rpm, 80° C in O_2 saturated 0.5M H_2SO_4 .

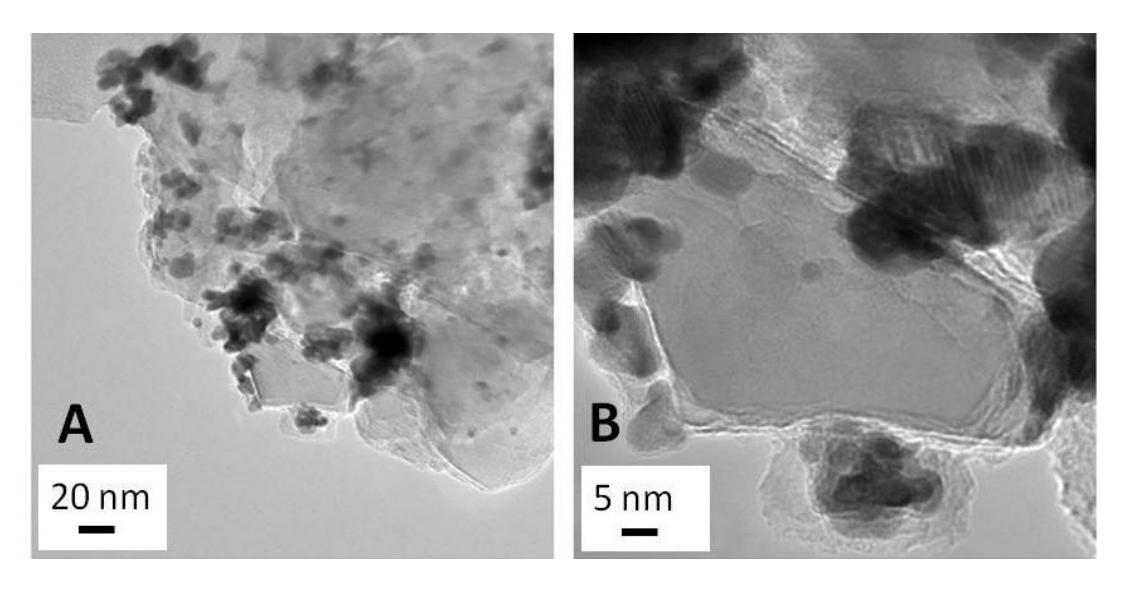


Figure 5.12. (A) TEM micrographs of 100 nm 20 wt % Pt/B-UNCD-diamond after anodic polarization for 1 h at 1.4 V in 0.5 M $_2$ SO₄ at 80 $_2$ C. (B) Higher magnification

5.3 Discussion

The electrochemical behavior of Pt/B-UNCD-diamond powder in acidic solution is almost identical to bulk Pt and Pt/Vulcan. The electrochemically active surface area (ECSA) and catalytic activity of platinum varies with the surface area of the diamond powder support. If we assume, the Pt particles are spherical, the ECSA area can be calculated by equation. 5.6.

$$ECSA = \frac{3 \times \text{Pt loading } \left(\frac{\text{mg}_{\text{Pt}}}{\text{cm}^2}\right)}{\text{Density of Pt } \left(\frac{\text{g}}{\text{cm}^3}\right) \times \text{radii of Pt particles(cm)}}$$
[5.6]

For a 0.14 mg/cm² Pt loading, theoretical ECSA of Pt/Vulcan (2 nm Pt diameter) [40, 41] is 200 cm². The calculated ECSA value is almost 1/3 of Pt/Vulcan active area for 100 nm Pt/UNCD-diamond powder. The experimental results are lower than calculated values. This might be due to several reasons. The most obvious reason for this difference is the Pt particle size. For the 3-6 nm diam. powder with a larger specific surface area, the ECSA and double layer region are higher than 100nm diam. diamond powder. Even though, in the TEM images, we did not observe differences in the particle size of platinum on different diamond powder, the observed differences in the active area of platinum could be related to the difference in the surface area of the diamond powder. Activity of Nafion in the electrolyte, and the support-Pt-Nafion triple region contact is another issue that may cause lower ECSA. We casted Nafion on the platinized powders. This is recommended way to control diffusion of oxygen in the Nafion layer. However this preparation technique might be a limitation for the contact of all supported Pt particles with Nafion to be active for ORR.

The calculated specific and mass activities are lower than the values for 20% Pt/Vulcan electrodes. This can be explained by the lower surface area (170 m²/g) of diamond supports. Beside this, the Pt particle size on Vulcan powder is smaller (~2 nm) [48] than the diamond powder and particle size effect decreases active Pt area and kinetic current on diamond supported Pt particles. Microscopic images show that very small percent of the powders which may interact less with the reactive plasma species were not homogeneously coated. The heterogeneity in the coverage results lower electronically conductive regions on the diamond powder. Poor electronic communication with lower conductive region of the UNCD coated powder and Pt could be another reason for lower catalytic activity of Pt.

The other reason for the surface area difference between the two catalysts may be the Pt dispersion difference which is related to BET surface area of the support material. (Vulcan XC-72: 235 m²/g and B-UNCD powder: 52 m²/g). It is also possible that the slight Pt surface area difference is caused by the different morphologies of the two supports. When the catalyst powders are dried on glassy carbon surface to form the electrode film, their packing are different due to their morphology difference, leading to the slight different surface accessibility of Pt.

Beside this, the interaction between diamond surface and Pt particles may not as strong as Pt-Vulcan interaction. This may be part of the Pt aggregation reason after corrosion. The Pt distribution and attachment on hydrogen terminated (Figure 5.5) and oxygen terminated diamond powder surfaces was studied and we did not observe any difference in distribution and particle size.

In the lower overpotential region, the Tafel slope for the $\rm O_2$ reduction at the B-UNCD diamond was almost the same as at the bulk Pt and Pt/Vulcan. 100mV increase in the electrode

potential, results 6 times increase in i_k value. This result indicates that B-UNCD diamond powder has an excellent support material for Pt. The reason for the excellent result is probably the fine and uniform dispersion of Pt on B-UNCD diamond powder. However, the small i_k at higher overpotential needs to be improved. We believe that this is due to poor electrical conductivity due to nonhomogeneous coating of the powders. We anticipated that if we add an electron-conductive agent such as graphite powder to catalyst support, we may improve the kinetic current and increase the number of particles effective in oxygen reduction. The methods of increasing kinetic current on Pt/B-UNCD-Diamond powder will be discussed in next chapter.

5.4 Conclusions

Results were presented on the preparation and characterization of platinized B UNCD powder as a catalyst for ORR. The results can be summarized as follows:

- 1. The XRD and TEM characterizations reveal a high and homogeneous dispersion of Pt particles for the Pt/B-UNCD-diamond powder can be prepared by the impregnation method.
- 2. HRTEM and EELS measurements show that the Pt nanoparticles attach directly to sp^3 carbon sites with no sp^2 carbon interfacial phase.
- 3. The kinetic parameters for the oxygen reduction reaction at Pt/B-UNCD-diamond powder are similar to those for clean polycrystalline Pt. The voltammetric features are all characteristic of polycrystalline Pt which indicates good electronic contact between the B-UNCD powder and the Pt particles.
- 4. The exchange current density on 3-6 nm Pt-loaded B-UNCD-diamond powder for the ORR in the fuel cell operative potential region (low overpotential region) is ca. 10^{-10} A·cm⁻² in

- 0.1 M HClO₄, which is in the same order of magnitude for Pt/Vulcan and Pt/B-UNCD-diamond
- The mass activity of the conductive diamond powder supported Pt is 0.09 (A/mg_{Pt}) at 0.9 V
 vs. RHE in 0.1 M HClO₄, comparable to reported for carbon-supported Pt.
- 6. The stability of Pt/B-UNCD-diamond and Pt/Vulcan XC-72 under simulated PEMFC conditions was investigated. Chronoamperemetric results show that B-UNCD powder has better corrosion resistance over Vulcan XC-72. The catalytic effect of Pt on B-UNCD powder corrosion is significantly less than that on Vulcan XC-72. The increase of Pt particle size after anodic polarization for Pt/Vulcan XC-72 is much more than that for Pt/B-UNCD-Diamond.
- 7. The electrochemical activity and durability test demonstrates that B-UNCD powder as catalyst support exhibits less Pt surface area loss without sacrificing catalytic activity, suggesting that diamond powder is a promising catalyst support for PEMFC application.
- 8. Further work will focus on to increase the electrical conductivity of diamond powder and catalyst dispersion procedure in order to reduce the particles size and improve the reactivity of this new type of catalyst.

References

- 1. F. T. Bacon, Electrochim. Acta, 14, 569 (1969).
- 2. A. J. Appleby and F. R. Foulkes, Fuel Cell Handbook, p. 762, Van Nostrand Reinhold, New York (1989).
- 3. W. Vielstich, A. Lamm, and H. Gasteiger, Handbook of Fuel Cells: Fundamentals, Technology, Applications, p. 2690, John Wiley & Sons, New York (2003).
- 4. S. Srinivasan, Fuel Cells: From Fundamentals to Applications, p. 692, Springer, Heidelberg (2006).
- 5. E. A. Ticianelli, C. R. Derouin, and S. Srinivasan, J. Electroanal. Chem. Interfacial Electrochem., 251, 275 (1988).
- 6. E. J. Taylor, E. B. Anderson, and N. R. K. Vilambi, J. Electrochem. Soc., 139, L45 (1992).
- 7. G. S. Kumar, M. Raja, and S. Parthasarathy, Electrochim. Acta, 40, 285 (1995).
- 8. Z. Qi and A. Kaufman, J. Power Sources, 113, 37 (2003).
- 9. K. Sasaki, J. X. Wang, M. Balasubramanian, J. McBreen, F. Uribe, and R. R. Adzic, Electrochim. Acta, 49, 3873 (2004).
- 10. M. W. Reed and R. J. Brodd, Carbon, 3, 241 (1965).
- 11. L. M. Roen, C. H. Paik, and T. D. Jarvi, Electrochem. Solid-State Lett., 7, A19 (2004).
- 12. C. H. Paik, T. D. Jarvi, and W. E. O'Grady, Electrochem. Solid-State Lett., 7, A82 (2004)
- 13. E. Antolini, J. Mater. Sci., 38, 2995 (2003).
- 14. A. J. Appleby, Corrosion (Houston), 43, 398 (1987)
- 15. U.S. DOE, http://www1.eere.energy.gov/hydrogenandfuelcells/mypp/, (2007).
- 16. H. Chang, S.H. Joo, C. Pak, J. Mater. Chem. 17, 3078 (2007).
- 17. C. Moreno-Castilla, F.J. Maldonado-Ho' dar, Carbon 43, 455 (2005).
- 18. T. Maiyalagan, B. Viswanathan, U.V. Varadaraju, Electrochem. Commun. 7, 905 (2005).
- 19. N. Sano, S. Ukita, Mater. Chem. Phys. 99, 447 (2006).
- 20. J. Jang, S.K. Ryu, J. Mater. Proc. Technol. 180, 66 (2006).
- 21. C.A. Bessel, K. Laubernds, N.M. Rodriguez, R.T.K. Baker, J. Phys. Chem. B 105, 1115 (2001).

- 22. J. Xu, M.C. Granger, Q. Chen, T.E. Lister, J.W. Strojek, G.M. Swain, Anal. Chem. 69, 591 (1997).
- 23. Q. Chen, M.C. Granger, T.E. Lister, G.M. Swain, J. Electrochem. Soc. 144, 3806 (1997).
- 24. A. Ay, V. M. Swope, and G. M. Swain, J. Electrochem. Soc 155, (10) B1013-B1022 (2008).
- 25. Liang Guo,a Vernon M. Swope, Belabbes Merzougui, Lesia Protsailo, Minhua Shao,b Qin Yuan,a and Greg M. Swain Journal of The Electrochemical Society, 157 (1) A19-A25 (2010).
- 26. A. J. Bard and L. R. Faulkner, Electrochemical Methods, Fundamentals and Applications, John Wiley & Sons, Inc, New York, (2001).
- 27. R. Vijayalakshmi, S. Kapoor, S. K. Kulshreshtha, Solid State Sci. 4, 489 (2002).
- 28. R. Arenal, O. Stephan, P. Bruno, and D. M. Gruen, Applied Physics Letters 94 (2009).
- 29. K. Okada, K. Kimoto, S. Komatsu, and S. Matsumoto, Journal of Applied Physics 93:3120 (2003).
- 30. J. Robertson, Semiconductor Science and Technology 18:S12 (2003).
- 31. L. C. Qin, D. Zhou, A. R. Krauss, and D. M. Gruen, Nanostructured Materials <u>10</u>:649 (1998).
- 32. S. Bhattacharyya, M. Lubbe, P. R. Bressler, D. R. T. Zahn, and F. Richter, Diamond and Related Materials 11:8 (2002).
- 33. M. Petravic, A. Hoffman, G. Comtet, L. Hellner, and G. Dujardin, Fizika A 8:275 (1999).
- 34. G. Comelli, J. Stoehr, C. J. Robinson, and W. Jark, Physical Review B: Condensed Matter and Materials Physics <u>38</u>:7511 (1988).
- 35. A. P. Hitchcock, D. C. Newbury, I. Ishii, J. Stohr, J. A. Horsley, R. D. Redwing, A. L. Johnson, and F. Sette, Journal of Chemical Physics 85:4849 (1986).
- 36. J. M. D. Rodíguez, J. A. H. Melián, and J. P. Peña, J. Chem. Educ., 77, 1195 (2000).
- 37. A. Essalik, K. Amouzegar, and O. Savadogo, J. Appl. Electrochem., 25, 404 (1995).
- 38. N. M. Markovic, I. M. Tidswell, P. N. Ross Langmuir, 10 (1), pp 1–4, (1994).
- 39. A. Schumpe, I. Adler, and W.D. Deckwer, Biotechnology and Bioengineering, 20(1): p. 145-150, (1978).
- 40. J. Schmidt, H. A. Gasteiger, G. D. Stab, P. M. Urban, D. M. KoIb, and R. J. Behm J. Electrochem. Soc., Vol. 145, No. 7, 2354 (1998).

- 41. N. Markovic, H. Gasteiger, and P. N. Ross, J. Electrochem. Soc., 144,1591 (1997).
- 42. F. E. Kadiri, R. Faure, and R. Durand, J. Electroanal. Chem., 177 (1991).
- 43. Arvind Parthasarathy, Supramaniam Srinivasan, A.John Appleby and Charles R. Martin, Journal of Electroanalytical Chemistry, Volume 339, Issues 1-2, 101-121 (1992).
- 44. Perry M. L. Perry, J. Newman, E. Cairns, J. Electrochem. Soc. 145, 5 (1998).
- 45. N. M. Markovic', B. N. Grgur, and P. N. Ross J. Phys. Chem. B, Vol. 101, No. 27, (1997)
- 46. M. Mathias, H. Gasteiger, R. Makharia, S. Kocha, T. Fuller, J. Pisco, Abstr. Pap. Am. Chem. Soc. 228, U653 (2004).
- 47. X. Wang Journal of Power Sources 158, 154–159 (2006).
- 48. H. A. Gasteiger et al. Applied Catalysis B: Environmental 56, 9-35, (2005).
- 49. A. Damjanovic and V. Brusic, Electrochim. Acta, 12,615 (1967).
- 50. A. Damjanovic and M. A. Genshaw, Eletrochim. Acta, 12, 1281 (1970).

Chapter 6

Performance of A Membrane Electrode Assembly Using A Diamond Powder Electrocatalyst Support

6.1 Introduction

Polymer electrolyte membrane fuel cells (PEMFCs) are being developed for transportation as well as for other stationary and portable power applications. The device produces electricity by direct electrochemical conversion of hydrogen and oxygen into water. The membrane electrode assembly (MEA) is the heart of the PEMFC, which consists of an anode and cathode separated by a proton exchange membrane (PEM). The electrodes consist of nanometer-sized electrocatalyst particles, such as Pt, dispersed over a high-surface-area (~100 m²/g) support material. The support material is commonly carbon. Finely dispersed electrocatalyst particles on a stable and conductive support increase the number of electrocatalytically-active sites available for the fuel cell reactions.

Carbon materials are suitable electrocatalyst supports because they are inert in the acidic environment of the PEMFC [1, 2]. They also have good electrical conductivity as a support material. On the other hand, a significant problem is the durability of carbon support material. Operating conditions of PEMFC have an impact on the carbon support stability in fuel cells. A working fuel cell is exposed to a wide range of potentials and high temperatures. Its potential mostly remains at between 0.6 and 1.0 V, at moderate to high relative humidity, with an operating temperature of 60-90 °C. However, during start up and shut down, some part of cathode could experience higher potentials (1.4 V vs. RHE) due to fuel starvation and at these high potentials carbon can easily corrode. The presence of Pt particles on carbon accelerates the carbon corrosion rate [3-5].

Electrochemical corrosion of the carbon supports will cause electrical isolation of the catalyst particles as they will become separated from the support or aggregated on the support surface. Both processes result in a decrease in the electrochemical active surface area of the catalyst and an increase in the hydrophilicity of the surface. The latter decreases the gas permeability to the catalyst surface as the pores fills with water. [3-5]. Therefore, the microstructural, thermal and mechanical stability of these electrode materials are crucial.

To improve the electrochemical activity and stability of the catalyst, new carbon and non-carbon materials have been tested. High surface area ultrananocrystalline diamond (UNCD) powder might be an alternative electrocatalyst support material for PEMFCs and is attractive because of its microstructural stability and corrosion resistance [10, 11, 42]. Ultrananocrystalline diamond (UNCD) is new kind of diamond formed of 3–6 nm crystallites made by detonation techniques and sold in large volumes worldwide for \$2-5/g. [6, 7] It possesses properties suited for an electrocatalyst support. It has high surface area (260 m²/g), superior morphological stability and corrosion resistance, compared to conventional sp² carbon support materials [8, 9]. It is chemically inert allowing for its use at elevated temperatures in oxidizing or reducing media without loss of properties. However, material possesses no inherent electrical conductivity which is a barrier to use these materials as a support material for fuel cells.

Previously, our group reported on the preparation of conductive diamond powder by coating insulating diamond powder (8–12 μ m diameter, 2m²/g) with a boron-doped diamond overlayer using microwave plasma-assisted chemical vapor deposition [10]. In this core-shell approach, the electrical conductivity is controlled by the doped-diamond overlayer (carrier concentration and mobility) rather than by some adventitious nondiamond sp² carbon impurity

phase on the powder surface. The specific surface area and electrical conductivity of the doped diamond powder were $2 \text{ m}^2/\text{g}$ and 0.6 S/cm, respectively. [10].

Recently, high surface area conductive diamond powder preparation (170 m²/g), its characterization and modification with Pt electrocatalyst particles were reported [11]. The electrochemical properties and thermal stability during air oxidation of platinized B-UNCD-diamond powder were evaluated. It was shown that B-UNCD-diamond powder possesses the requisite electrical conductivity (~1 S/cm) and specific surface area (170 m²/g) for a viable electrocatalyst support and, more importantly, the material exhibits excellent carbon oxidation resistance in the presence of Pt. Uniformly distributed Pt particles were formed on the powder using a wet chemical impregnation. The nominal Pt particle size was ~5 nm. The Pt particles bonded directly to the diamond surface with no evidence for any graphitic interfacial layer. [11]

In the present work, this same B-UNCD-diamond powder was employed as an electrocatalyst support material in an MEA for the first time. Several approaches can be used to prepare MEAs [12-20]. The MEAs used in this study were prepared by the decal hot pressing technique [19, 20]. The electrode is a comprised of an electrocatalyst, the support material and a network of Nafion ionomer that holds this supported catalyst powder together and provides a proton conductive path way. An optimum Nafion loading in the electrode is necessary to achieve high power density. Low Nafion content leads to poor contact of the electrolyte with the catalyst and hence poor electrocatalyst performance. On the other hand, high Nafion content can block the catalytic sites and plug the electrode pores, hence reducing gas permeability and increasing mass transfer resistance. There have been many studies concerning the effect of Nafion content on electrode performance [21-23]. However, these studies were performed using carbon black (a

typical sp² carbon support material) and different Nafion loadings were suggested by different researchers. In our study, we calculated the Nafion content in the electrode layer as a percentage of the support and electrocatalyst weights.

For the durability measurement, the changes in the open circuit voltage (OCV) and electrochemically active surface area (ECSA) of a single cell were monitored during accelerated degradation test. As the support material corrodes, the electrocatalyst metal particles lose their contact and they agglomerate to form larger particles which results in an ECSA decrease. The particles can also migrate within the Nafion membrane and block the proton conductivity. Also, as the support material degrades, there will be particle-particle contact lost within the electrode causing increased cell resistance. Therefore, monitoring the OCV and ECSA during accelerated degradation testing give us idea about the stability of electrodes.

The performance of membrane electrode assemblies (MEA) prepared by using the Pt-loaded B-UNCD-diamond powder is described. A 200-h accelerated degradation test was performed in a single cell assembly, and the cell potential and catalyst activity were monitored as a function of time during the imposed test conditions. SEM images were obtained to characterize the MEAs before and after testing and the results compared with Pt-loaded Vulcan XC-72.

6.2 Results

6.2.1 Optimum Nafion Content in the Electrocatalyst Layer

The ionomer loading in the catalyst layer was adjusted while maintaining a Pt loading of 0.5 mg/cm². The normalization area was the geometric area. The effect of the ionomer loading on the cathode performance is illustrated in Figure 6.1. The cyclic voltammetric *i-E* curves revealed that the ECSA increases with the Nafion content (Fig.6.1.A). The best performance was observed for the 60 wt. % level. As the Nafion content increases, more ionomer interacts with

the Pt electrocatalyst particles forming the triple-phase interface (Fig. 6.1B). Increased contact with the ionomer leads to a higher flux of \overline{H}^+ to the catalyst sites for oxygen reduction. The onset potential for oxygen reduction also decreased, ~ 40 mV, with an increase in the ionomer loading.

6.2.2 Durability

Figure 6.2 shows representative cyclic voltammetric i-E curves for Pt/Vulcan and Pt/B-UNCD-diamond MEAs before and after accelerated degradation testing. The voltammetric features of Pt are better defined on diamond than they are on Vulcan, but in general, both Pt-loaded carbons exhibited features characteristics of Pt (e.g., Pt-oxide formation and oxygen evolution at potentials positive of 0.9 V, the reduction of Pt oxide at \sim 1.0 V, the adsorption and desorption of hydrogen between 0.2 and 0.4 V, and the double layer charging region between 0.4 - 0.5 V). For both, the charge under within the voltammetric curves decreased after the degradation test.

The ECSA values for both carbon supports during the testing period are shown in Figure 6.3. For both carbons, more prominently for Vulcan though, the ECSA increases during the 30 h of testing. This is due to cleaning and conditioning of the Pt. After reaching a maximum at approximately the 30-h mark, the ECSA for both carbons monotonically decreased up to the 200-h mark. The decrease for Vulcan, however, was greater than for diamond: 41 vs. 19 % loss relative to the maximum. After the 200-h degradation test, the ECSA decreased from 111 to 64 cm² for Pt/Vulcan, and from 67 to 53 cm² for Pt/B-UNCD-diamond. The Pt/B-UNCD-diamond powder exhibited better stability than the Pt/Vulcan under these testing conditions.

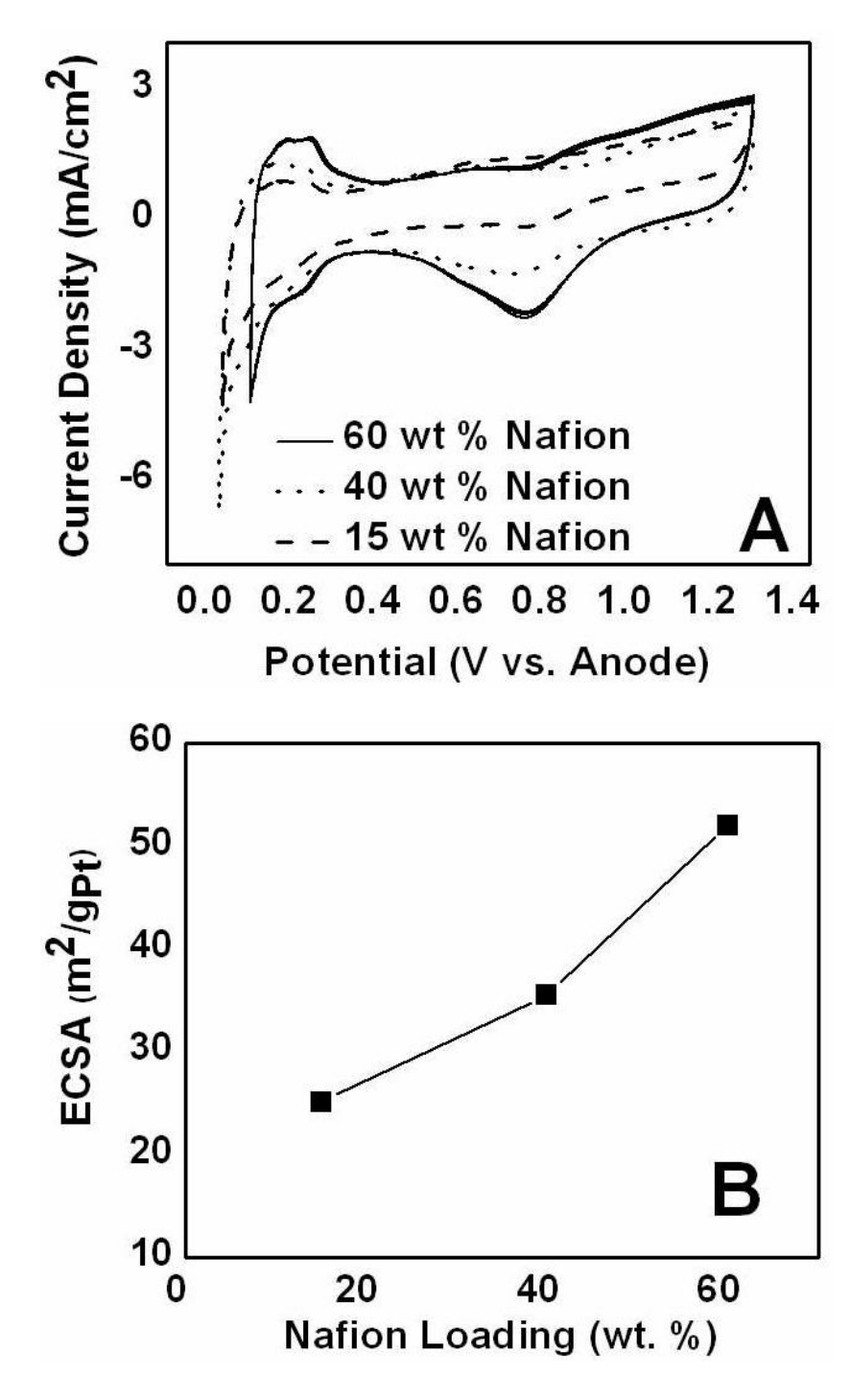


Figure 6.1 (A) Cyclic voltammetric i-E curves for Pt/B-UNCD-diamond MEAs at room temperature with 0.5 mg Pt/cm 2 in the catalyst layer. Scan rate=5 mV/sec. (B) Electrochemically active surface area (ECSA) of Pt/B-UNCD-diamond MEAs versus various Nafion content in the catalyst layer. The anode served as both the counter and reference electrode in the cyclic voltammetry measurements. the anode is essensially at the potential of the RHE.

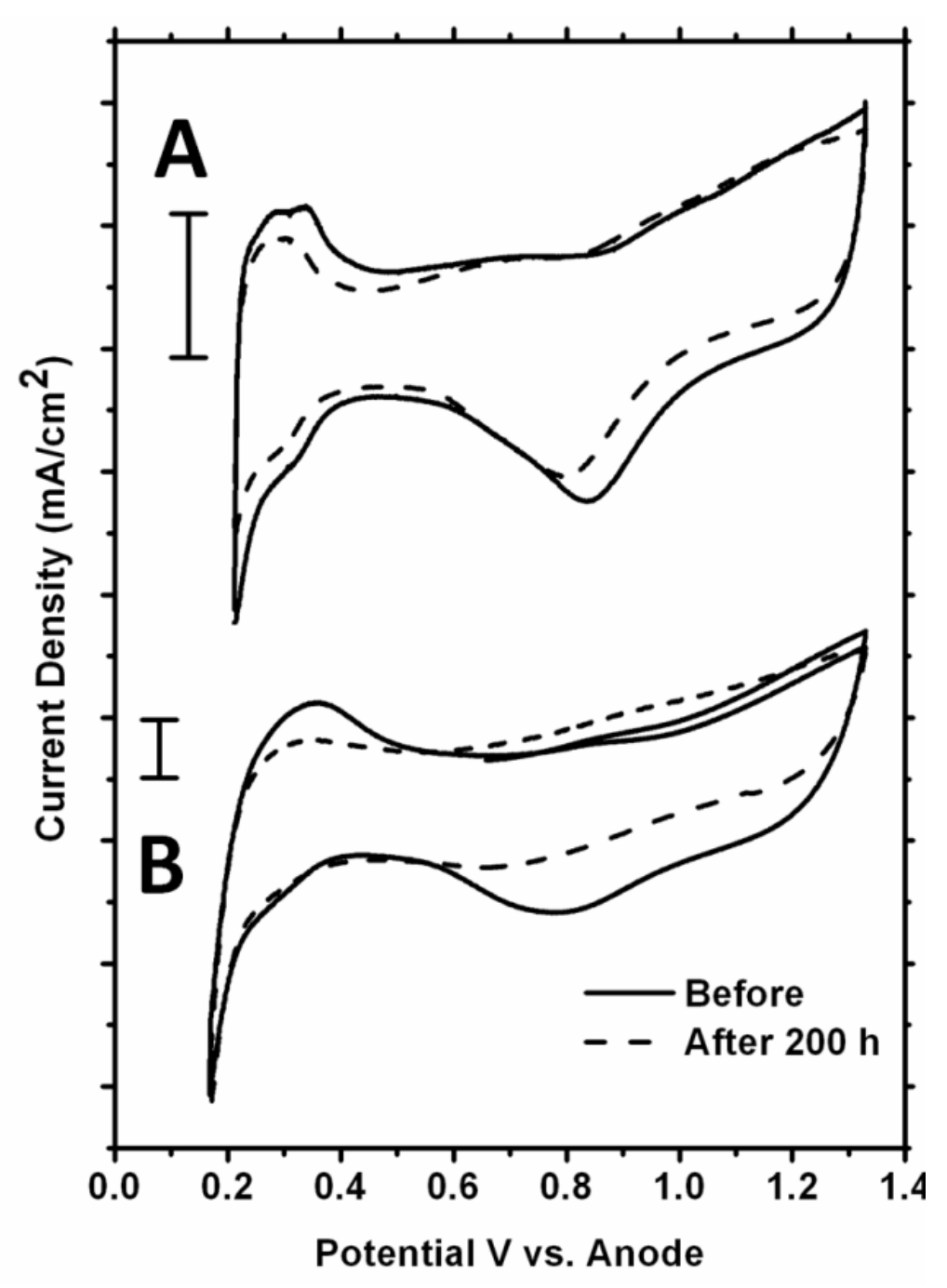


Figure 6.2 Cyclic voltammetric *i-E* curves for (A) Pt/B-UNCD-diamond and (B) Pt/Vulcan MEAs before and after a 200-h accelerated degradation test at room temperature. Scan rate 5 mV/sec. Scale bars show 1 mA/cm 2 for each voltammogram.

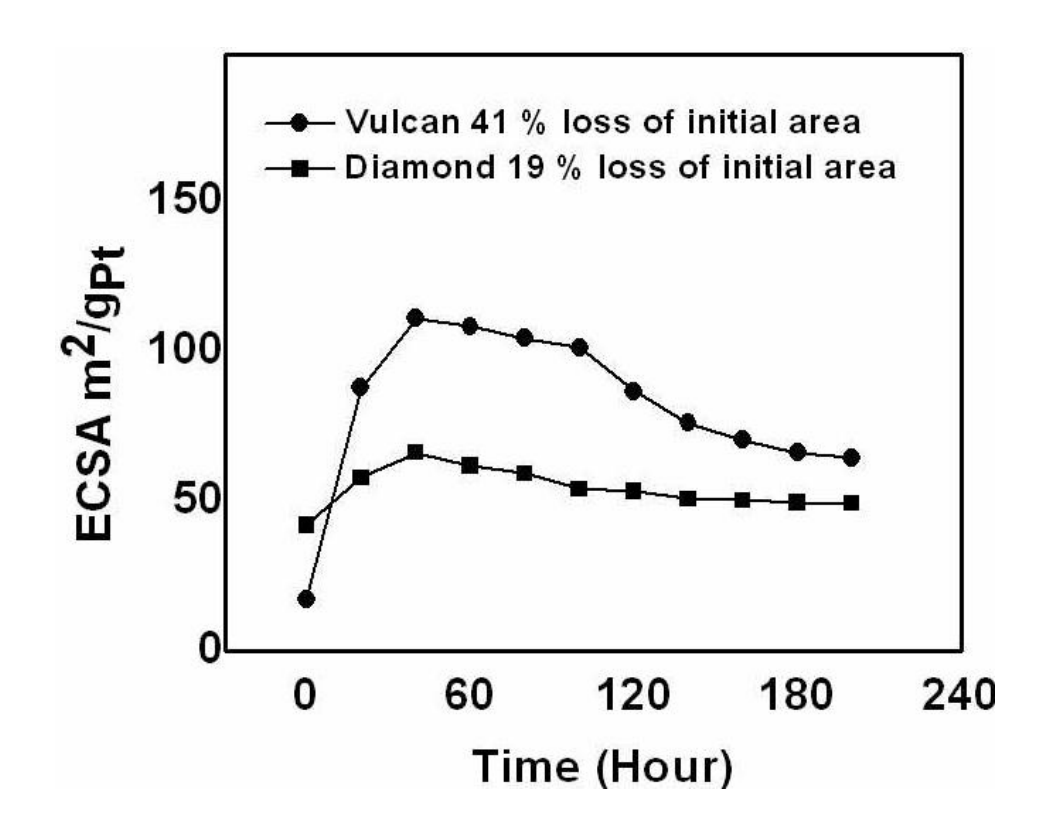


Figure 6.3. Comparison of the ECSA for Pt/Vulcan and Pt/B-UNCD-diamond MEAs during a 200-h degradation test at room temperature.

Figure 6.4 shows the dependence of the OCV for both support materials as a function of the accelerated degradation time. Very similar OCVs were observed for both MEAs especially after the 30-h mark. Prior to this, there were some differences in the OCV. Initially, the OCV for the Pt/Vulcan MEA was more positive than the value for Pt/B-UNCD-diamond the MEA by 100 mV. The OCV for both materials increased during the first 10-20 h before reaching a similar value of 0.95 V. At the 30-h mark, the OCVs were 1.05 and 0.99 V for Pt/Vulcan and Pt/B-UNCD-diamond respectively. After the OCV reached the maximum, a decrease was seen for Vulcan and over the subsequent 150-h to 0.89 V. For Pt/B-UNCD-diamond, the voltage decreased from 0.99 to 0.95 V between 30 and 50 h. After this, a slow voltage decrease to 0.92 V was observed. The OCV decay rates were calculated to be 45 and 20 μV/h for the Pt/Vulcan and Pt/B-UNCD-diamond MEAs, respectively.

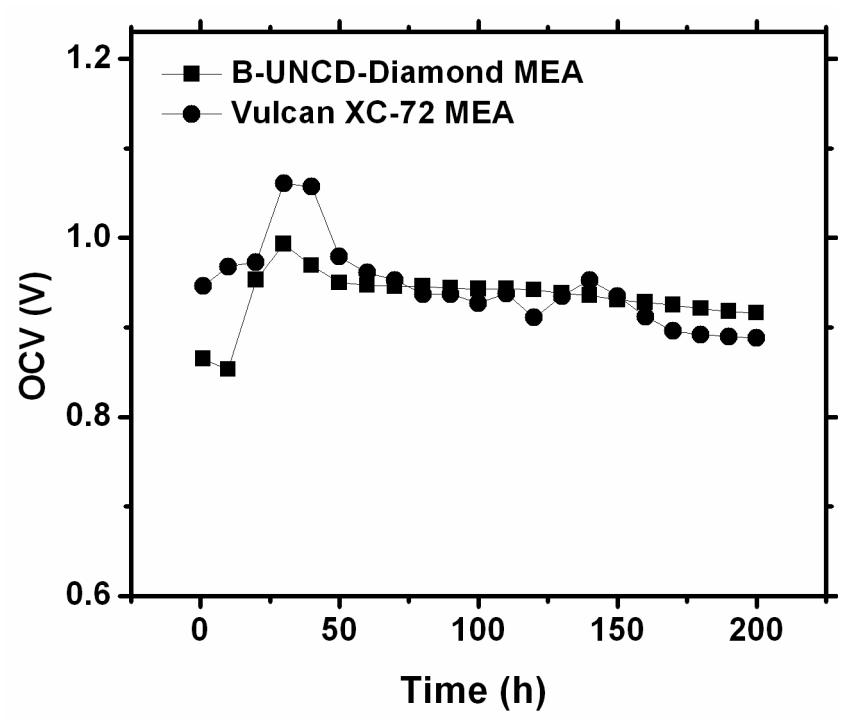


Figure 6.4. Open circuit voltage (OCV) of the cell as a function of time during the MEA accelerated degradation test. The cell was operated at room temperature using an H_2/O_2 flow rates of 2/9.

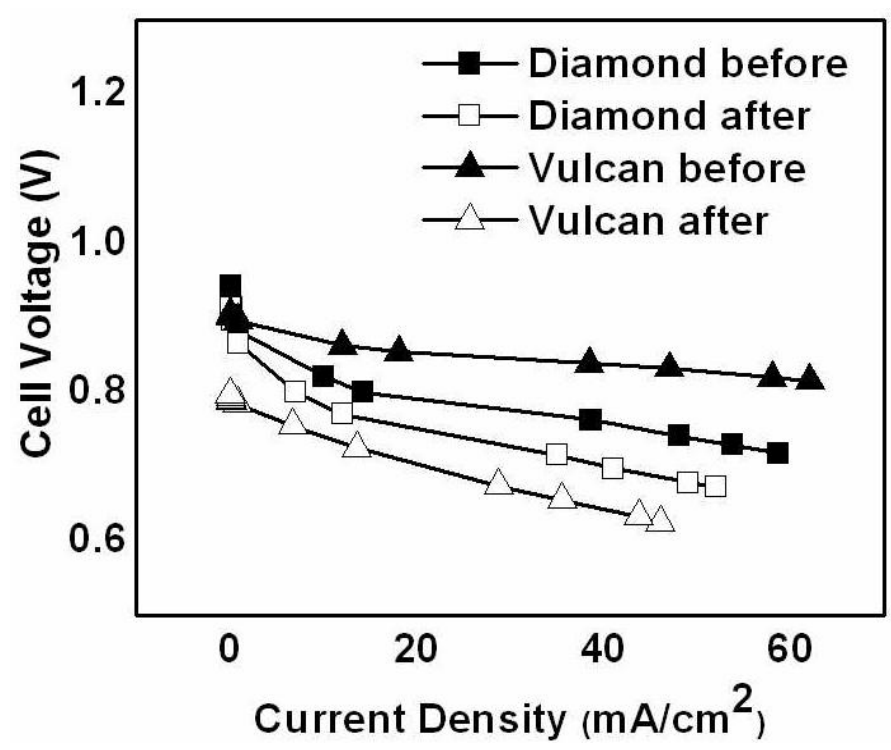


Figure 6.5. Current-voltage plots for Pt/B-UNCD-diamond and Pt/Vulcan MEAs before and after a 200-h degradation test. The current was normalized to the geometric area of the electrode.

Figure 6.5 shows current-voltage (i-V) plots for the Pt/Vulcan and Pt/B-UNCD-diamond MEAs before and after a 200-h degradation test. The initial cell potential for both MEAs was less than the theoretical value of 1.23 V. This is due to activation loss or activation overpotential for oxygen reduction at the cathode []. A rapid initial voltage decrease (~40 mV) is seen for both MEAs due to the slow reactions taking place on the surface activation. The voltage decreases less rapidly and more linearly after activation potential. This is caused by electron flow resistance or resistance of various interconnections. Based on the slope changes, the Pt/B-UNCD-diamond MEA has an ohmic resistance determined in the linear region. This is due to the incomplete B-UNCD coverage on the diamond powder, as well as poor particle-particle contact due to the irregular shape of the diameter substrate particles. The resistance increases by 4x after testing while the ohmic resistance of Pt/B-UNCD-diamond remained virtually unchanged. At 0.715 V, the current densities of the B-UNCD-diamond supported MEA was 59 mA/cm² while, the value for the Vulcan MEA was 62 mA/cm² at 0.815 V. After 200 h accelerated degradation test, the current density was significantly decreased to 16 mA/cm² at 0.715 mV for the Vulcansupported MEA. The current density at the same potential for the B-UNCD-diamond MEA was 36 mA/cm². After 200h, the activation potential loss or over potential for ORR significantly increased (250 mV) for Vulcan MEA. The resistance changed in the performance curve for B-UNCD-diamond MEA, however there was no significant lost of activity for B-UNCD-diamond MEA. It should be noted that all the polarization curves obtained in this study were comparable to each other, being obtained under strict comparable experimental conditions. However, in comparing these results with literature data, the geometry of the fuel cell used for the electrochemical characterization, temperature and humidification conditions in which the fuel

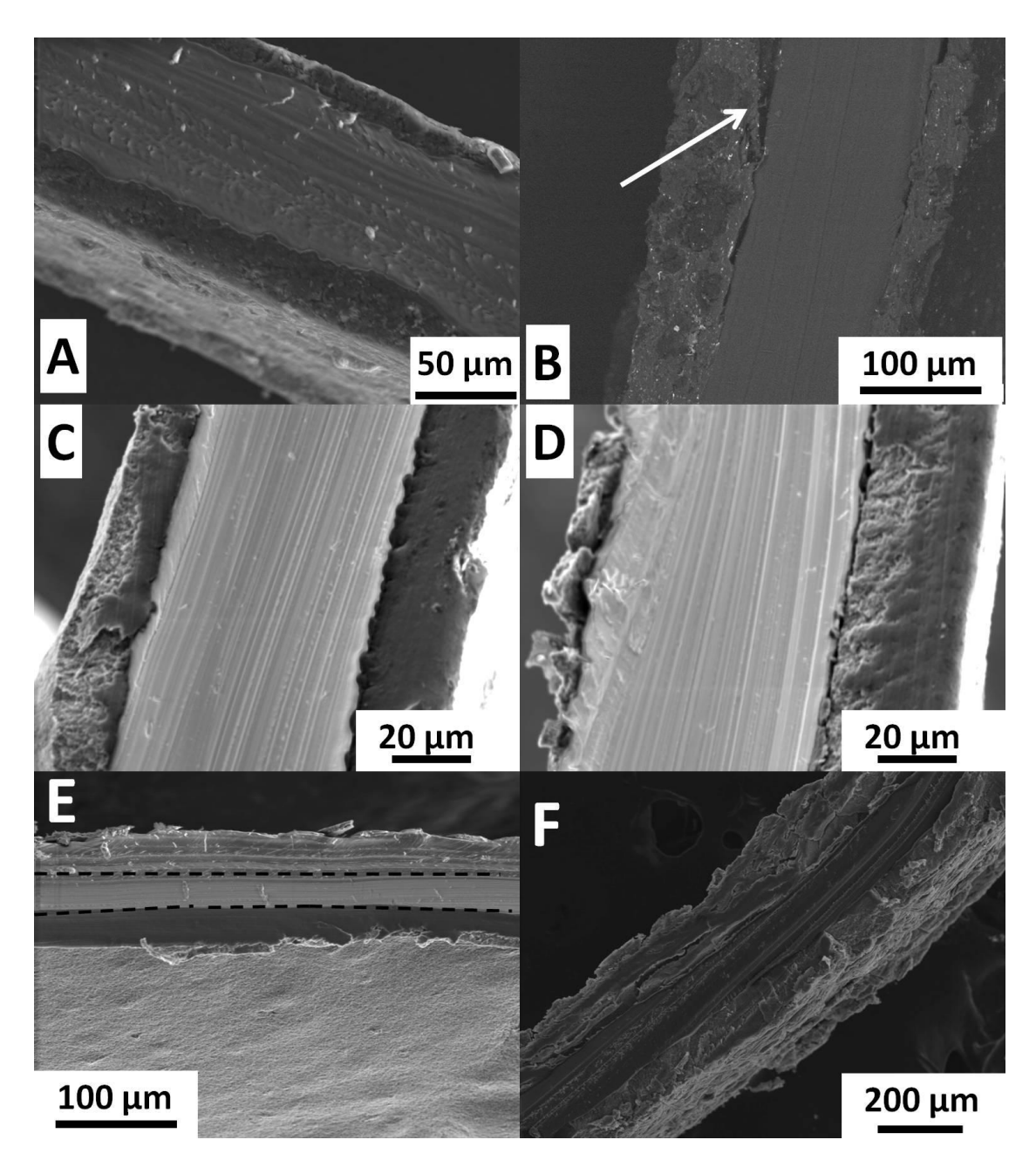


Figure 6.6. SEM cross-section images of Pt/B-UNCD-diamond and Pt/Vulcan MEAs before and after a 200-h degradation test. (A) B-UNCD-diamond before, (B) B-UNCD-diamond after, (C) Vulcan before, (D) Vulcan after. (E) Vulcan-before (electrode surface), (F) Vulcan-after (larger area).

cell tests were carried out should be considered since all these factors significantly affect the performance of the fuel cell.

6.2.3. Morphology of MEA Before and After Durability Test

SEM images of the Pt/Vulcan and Pt/B-UNCD-diamond MEAs obtained before and after testing are shown in Figure 6.6. Before accelerated degradation testing, smooth electrode layers interfacing with the Nafion membrane were seen for both Vulcan and B-UNCD-diamond MEAs. (Figure 6.6.A and 6.6.E). There were no loose points at the contact of the electrode layers from the Nafion membrane. After the 200-h accelerated degradation test, for the Pt/B-UNCD-diamond MEA no change in the thickness of the membrane or the electrode layers was detected. There was only some separation of the cathode from membrane as seen in the Fig. 6.6B. For the Pt/Vulcan MEA, many cracks at the anode side, and severe corrosion at the cathode side were seen. The thickness of the cathode was significantly decreased compare to the fresh MEA consequence of the carbon corrosion. At some parts, electrode lost its solid texture, and laminated and loose carbon layers were formed at the cathode. With the correlation of electrochemical performance results, these areas have large influence on the resistance of the MEA which are observed in the performance plots.

6.3 Discussion

Improving the stability of the electrodes (electrocatalyst+support) during fuel cell operation is a critical issue to address. All results indicate that the B-UNCD-diamond powder is a more stable electrocatalyst support than is Vulcan XC-72. Optimal MEA preparation is critical for maximum fuel cell performance. To determine the optimum Nafion loading, several electrodes with different Nafion content were prepared and tested. For Vulcan powder (220 m²/g surface area), the Nafion-to-carbon weight ratio is suggested to the 40 % [26]. For B-UNCD-

diamond powder (170 m²/g surface area) the highest ECSA was observed with 60 wt. % Nafion binder ratio as it is shown in Figure 6.1. The difference in the ionomer ratio might be due to hard diamond structure and irregular shape of diamond powder. The interaction between diamond surface and Nafion polymer is not well studied at this point, and there might be a limitation in the interaction between diamond and Nafion due to surface chemistry.

ECSA is one of the most important criteria for fuel cell performance and durability. A larger ECSA means more catalytic sites for electrode reactions, better distribution of catalyst particles, and good electrocatalyst-support material interaction. The fuel cell voltage and current density mostly depend on the electrochemically-active platinum surface area in the cathode. It has been reported that the ECSA loss in PEMFCs is largely due to the support degradation and reduced contact of the electrocatalyst with the support material [30, 31]. The degradation in ECSA can be also related to several factors, such as Pt particle size changes (Pt sintering), Pt poisoning due to some impurities such as CO, the oxidation of carbon support, and Pt dissolution [32-38].

The voltammetric features for Pt are better defined on diamond than they are on Vulcan. This might be due to the surface impurity of the Pt particles. As the carbon corrosion takes place in the electrode, CO may be adsorbed on Pt and poison available Pt particles. Aside from this, B-UNCD-diamond powder may have influence on the hydrogen adsorption and desorption of Pt. Since the catalysts are attached to the support, the support material can affect the catalytic activity of the Pt. B-UNCD-diamond might modify the electronic structure of the catalyst particles and this modification could affect the reaction kinetics. Another effect of support material can be structural. The support material might also modify the shape of the catalyst particles. Those effects could change the activity of catalytic sites on the metal surface and

modify the number of active sites present [50]. Besides these, B-UNCD-diamond may bring own catalytic effect to the reactions [51] which is another important research subject for B-UNCD-diamond powders in the field of the energy devices and catalysts.

Another important property of the B-UNCD-diamond powder that needs to be discussed is its surface structure. Diamond powder has smooth crystalline surface without any porosity. Vulcan is a porous carbon which may create a difficulty in fuel and product diffusion whereas B-UNCD-diamond powder's three dimensional solid non-porous morphology may enhance the fuel diffusion.

For the first 30 hours, the ECSA increased for both MEAs. Similar results were also observed in other MEAs cyclic voltammetry studies [39]. This result can be attributed to an increase in the active area of the electrode caused by an efficient removal of adsorbed impurities during anodic polarization, as suggested by Bett et al. [40]. Alternatively, there may have been an increase in the hydrophilicity of the electrode due to the oxidation of the carbon support, which may cause an increase in the wettability and hence the ECSA area of the electrode.

Very comparable OCV and performance results were observed for B-UNCD-diamond MEA to Vulcan MEA. The results show that diamond support well behaved as electronic path continuity. However, the OCV of B-UNCD-diamond MEA is slightly less than Vulcan MEAs. This might be due to Pt particle size on the diamond powder (~5 nm) which is larger than Vulcan (2 nm) supported Pt particles (particle size effect) [46-49].

After 200-h test, we assume that catalyst support degradation is an apparent reason for the loss of Pt surface area over time. This process has been observed in our study by SEM images and there are several groups found similar results for Vulcan XC-72 support material [31]. It has been know that B-UNCD-diamond powder exhibits excellent carbon corrosion resistance in the

presence of Pt at high temperatures for a long period of time [11. 41, 42]. For B-UNCD-diamond MEAs, after degradation test very stable and solid electrodes were observed in the SEM results, however, there are some lost in the ECSA, and in the OCV and the ohmic resistance increase as a function of testing time. Here, we hypothesis several reasons for this lost:

- 1. The high potential cycling could severely oxidize Pt and cause catalyst dissolution. Ostwald ripening of platinum particles on the carbon support, Pt dissolution at these testing conditions and diffusion of this dissolved Pt species in the ionomer phase to the membrane might be most important reason for the ECSA decrease for B-UNCD-diamond MEAs. These platinum particles have no electrical contact with diamond support material and lost their electrochemical activity.
- 2. The water management is a problem during our test conditions due to room temperature study. The contact lost of the electrodes from the membrane might be a result of this problem. The membrane hydrophilic property and hydrophobic property of the diamond support causes a water accumulation at the boundary and this water opens up the contact layer as it is observed in SEM images. When these parts lost their contact from the membrane, they are not only become electrochemically inactive, they also increase ohmic resistance of the cell.
- 3. It is known that pure diamond powder is very stable and resistance to corrosion under these experimental conditions [11, 41, 42]. However, during preparation B-UNCD-diamond powder, there is a probability to observe other carbon structure in the diamond growth [42, 45]. Some graphite platelet structure were observed after boron doped diamond layer coating (Figure 6.7), which might be remain after acid washing procedure. These structures might be corroding during accelerated degradation test, and their corrosion results in an increase ohmic resistance.

4. The other components in the fuel cell such as Nafion in the catalyst layer and carbon paper might be damaged due to accelerated degradation test. Their degradation may incarese the ohmic resistance within the cell.

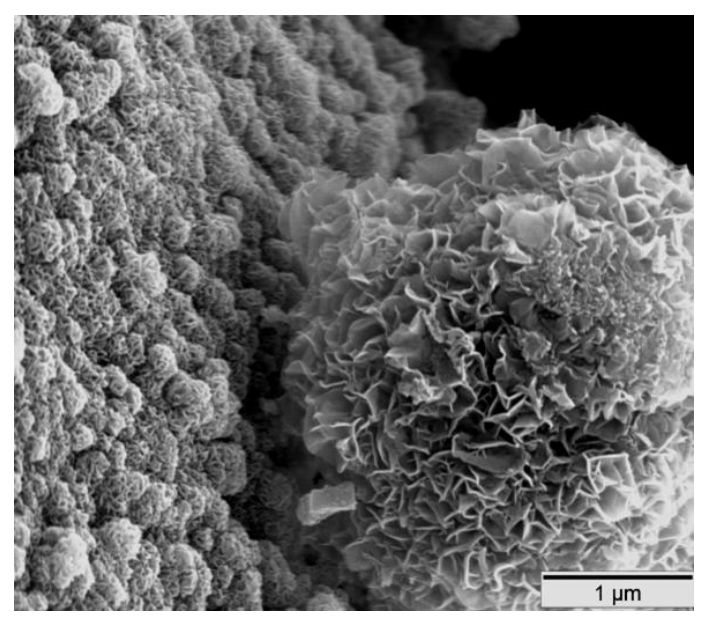


Figure 6.7. SEM images of graphite nanoplatelets formed on some powder surfaces during B-UNCD growth. In addition to B-UNCD, this carbon forms during the overcoating process.

For both diamond and Vulcan MEA case, we could not generate high current densities due to limitations in our fuel cell test station. One of the limitations is the humidification problem. The reactant gases were purged through water at room temperature. This bubbling was not enough for fully humidification of the gases. Beside

this temperature is another factor that limits our current density. As the temperature increase, the catalytic activity of the Pt particles increases. High temperature needs to be balanced with correct humidification ratio to increase the performance of the fuel cells.

6.4 Conclusion

For the first time, application of high surface area conductive diamond powder as a Pt support material for PEMFC was reported. MEAs by Vulcan XC-72 and B-UNCD-diamond support material were prepared by hot decay technique and tested as 1cm² single fuel cell at room temperature. Their stability was tested for 200-h by measuring OCV and ECSA. B-UNCD diamond powder shows significantly better stability compared to commercial Vulcan XC-72 support material. The performance of MEAs that were tested in our laboratories were not optimized yet due to some limitations in humidification system and water removal weakness, however the results were comparable with commercial Vulcan MEA, which is a sign of good electrical contact of B-UNCD-diamond powder support at the triple region. There is still some room to increase conductivity of support material by mixing graphite powder which will be a future study for this project. From the results obtained in this study it can be concluded that B-UNCD-diamond powder can be a good candidate for PEMFC catalyst support. However, this study is performed at room temperature the conclusion drawn here may not be fully applied to high temperature conditions. We are now in the process to evaluate the B-UNCD-diamond powder durability at high temperatures with better humidification methods.

References

- 1. C.H. Hamann, A Hamnett, and W. Vielstich, "Electrochemistry", 1st ed. WieleyVCH, Weinheim, 1998.
- 2. E. Yeager, "Dioxygen electrocatalysis: mechanisms in relation to catalyst structure", J. of Mole. Catal., 38, p5-25, 1986.
- 3. Roen, L. M.; Paik, C. H.; Jarvi, T. D. Electrochem. Solid-State Lett., 7, A19, 2004.
- 4. Yu, P. T.; Gu, W.; Makharia, R.; Wagner, F. T.; Gasteiger, H. A.ECS Trans., 3, 797, 2007.
- 5. Kinoshita, K. Carbon: Electrochemical and Physicochemical Properties; Wiley: New York, 1988.
- 6. P. de Carli and J. Jamieson, Formation of diamond by explosive shock, Science 133, 1821 (1961); P. S. de Carli, US Patent 3, 238,019, 1966.
- 7. K. V. Volkov, V. V. Danilenko, and V. I. Elin, Diamond synthesis from the carbon of detonation products, Fiz. Goren. Vzriva 26, 123–125 (1990) (in Russian).
- 8. J. Xu, M.C. Granger, Q. Chen, T.E. Lister, J.W. Strojek, G.M. Swain, Anal. Chem. 69, 591, 1997.
- 9. Q. Chen, M.C. Granger, T.E. Lister, G.M. Swain, J. Electrochem. Soc. 144, 3806, 1997.
- 10. A. E. Fischer and G. M. Swain, J. Electrochem. Soc., 152, B369, 2005.
- 11. Liang Guo, Vernon M. Swope, Belabbes Merzougui, Lesia Protsailo, Minhua Shao, Qin Yuan,a and Greg M. Swain, Journal of The Electrochemical Society, 157 (1) A19-A25, 2010.
- 12. E. Ticianelli, C. Derouin, S. Srinivasan and A. Redondo, J. Electrochem. Soc. 135, pp. 2209–2214, 1998.
- 13. S. Srinivasan, A. Ferreira, R. Mosdale, S. Mukerjee, J. Kim, S. Hirano, S. Lee, F. Buchi, A. Appleby, in: Proceedings of the Fuel Cell, pp. 424–427, 1994.
- 14. E. Taylor, E. Anderson and N. Vilambi, J. Electrochem. Soc. 139, pp. L45–L46, 1992.
- 15. S. Foster, P. Mitchell, R. Mortimer, in: Proceedings of the Fuel Cell, pp. 442–443, 1994.
- 16. P. Fedkiw and W. Her, J. Electrochem. Soc. 136, pp. 899–900, 1989.
- 17. E. Gulzow, M. Schulze, N. Wagner, T. Kaz, R. Reissner, G. Steinhilber and A. Schneider, J. Power Sources 86, pp. 352–362, 2000.
- 18. T. Matsubayashi, A. Hamada, S. Taniguchi, Y. Miyake, T. Saito, in: Proceedings of the Fuel Cell, pp. 581-584, 1994.
- 19. S. Gottesfeld and M. Wilson, J. Electrochem. Soc. 139, pp. L28–30, 1992.

- 20. S. Gottesfeld and M. Wilson, J. Appl. Electrochem. 22, pp. 1–7, 1992.
- 21. S.J. Lee, S. Mukerjee, J. McBreen, Y.W. Rho, Y.T. Kho, T.H. Lee, Electrochim. Acta 43, 3693, 1998.
- 22. E. Antolini, L. Giorgi, A. Pozio, E. Passalacqua, J. Power Sources 77, 136, 1999.
- 23. E. Passalacqua, F. Lufrano, G. Squadrito, A. Patti, L. Giorgi, Electrochim. Acta 46, 799, 2001.
- 24. Fuel Cell Systems Explained, Second Edition James Larminie and Andrew Dicks, John Wiley & Sons Ltd, 2003
- 25. Schwartz, R. and Robbins, H. J. Electrochem. Soc., 123, 1903, 1976.
- 26. H.A. Gasteiger et at. / Applied Catalysis B: Environmental 56, 9-35, 2005.
- 27. Bevers, D., Wagner, N. and Von Bradke, M., Int. J. Hydrogen Energy, Vol. 23, No. I, pp. 57-63, 1998.
- 28. DOE Cell Component accelerated Stress Test Protocols for PEMFCs March 2007
- 29. Y. Y. Shao, G. P. Yin, and Y. Z. Gao, Chin. J. Inorg. Chem., 21, 1060, 2005.
- 30. Bhaskar Sompalli, Brian A. Litteer, Wenbin Gu, and Hubert A. Gasteiger J. Electrochem. Soc. 154, B1349, 2007.
- 31. P. J. Ferreira, G. J. la O', Y. Shao-Horn, D. Morgan, R. Makharia, S. Kocha, and H. A. Gasteiger J. Electrochem. Soc. 152 A2256, 2005.
- 32. D. A. Landsman and F. J. Luczak, in Handbook of Fuel Cells-Fundamentals, Technology and Applications, W. Vielstich, A. Lamm, and H. Gasteiger, Editors, Vol. 4, pp. 811-831, John Wiley & Sons, Chichester, U.K, 2003.
- 33. J. Aragane, T. Murahashi, and T. Odaka, J. Electrochem. Soc. 135, 844, 1988.
- 34. K. F. Blurton, H. R. Kunz, and D. R. Rutt, Electrochim. Acta 23, 183, 1978.
- 35. G. A. Gruver, R. F. Pascoe, and H. R. Kunz, J. Electrochem. Soc. 127, 1219, 1980.
- 36. J. A. S. Bett, K. Kinoshita, and P. Stonehart, J. Catal. 41, 124, 1976.
- 37. A. Honji, T. Mori, K. Tamura, and Y. Hishinuma, J. Electrochem. Soc. 135, 355, 1988.
- 38. J. A. Bett, K. Kinoshita, and P. Stonehart, J. Catal. 35, 307, 1974.
- 39. M. Cai et al. / Journal of Power Sources 160, 977–986, 2006.
- 40. J. Bett, K. Kinoshita, K. Routsis, P. Stonehart, J. Catal. 29, 160–168, 1973.

- 41. A. E. Fischer and G. M. Swain, J. Electrochem. Soc., 152, B369, 2005.
- 42. Ay, A.; Swope, V. M.; Swain, G. M. J. Electrochem. Soc., 155, B1013, 2008.
- 43. Inaba M, Kinumoto T, Kiriake M, Umebayashi R, Tasaka A, Ogumi Z. Electrochim Acta; 51(26): 5746–53, 2006.
- 44. Sethuraman VA, Weidner JW, Haug AT, Protsailo LV. J Electrochem Soc; 155(2):B119–24, 2008.
- 45. Doo Young Kim, Belabbes Merzougui and Greg M. Swain, *Chem. Mater.*, 21 (13), pp 2705–2713, 2009.
- 46. K. Kinoshita, J. Electrochem. Soc. 137, 845, 1990.
- 47. M. Watanabe, H. Sei, P. Stonehart, J. Electroanal. Chem. 261, 375, 1989.
- 48. K. Yahikozawa, Y. Fujii, Y. Matsuda, K. Nishimura, Y. Takasu, Electrochim. Acta 36, 973, 1991.
- 49. A. Kabbabi, F. Gloaguen, F. Andolfatto, R. Durand, J. Electroanal. Chem. 373, 251, 1994.
- 50. R.L. Augustine, Heterogeneous Catalysis for the Synthetic Chemists, Marcel Dekker, New York, 1996.
- 51. Katherine B. Holt, Christoph Ziegler, Daren J. Caruana, Jianbing Zang, Enrique J. Milla´n-Barrios, Jingping Hu and John S. Foord., Phys. Chem. Chem. Phys., 10, 303–310, 2008.

Chapter 7

Conclusion and Future Research Directions

7.1 Conclusion

Microstructural degradation and corrosion reactions of the sp²-bonded carbon electrocatalyst support of PEMFC under high potentials (1.2 to 1.5 V vs. SHE) during start-up and shut-down, as well as idle operation, is a problem that directly affects PEMFC efficiency. Degradation of carbon support materials in PEMFC will cause electrical isolation of the catalyst particles as they are separated from the support. As they lost their contact they would aggregated which result in a decrease in the electrochemical active surface area. Carbon support corrosion will also increase the hydrophilicity of the surface which can result in a decrease in gas permeability as the pores become more likely to be filled with liquid water. On this basis, an important issue of the research in the field of the fuel cells is addressed on the development of new carbon and non-carbon supports material, which has high corrosion resistance. UNCD diamond powder possesses properties suited for an electrocatalyst support for fuel cells. It has high surface area (260 m²/g), superior morphological stability and corrosion resistance compared to conventional sp² carbon support material. It is chemically inert allowing for its use at elevated temperatures in oxidizing or reducing media without loss of properties. However, it is electrically insulator and electrical conductivity is a barrier to use these materials as a support material for fuel cells.

The research presented in this dissertation focused on the development of a new, dimensionally-stable electrocatalyst support material based on UNCD powder. The objectives of this research were:

- Development of new synthetic technique to produce high surface area conductive diamond powder in a homogeneous, effective and economic way.
- Characterization of B-UNCD-diamond powder in terms of electrical conductivity, stability, structural property and surface chemistry.
- Establishing a technique to modified conductive diamond powder with nanometer size Pt electrocatalyst particles uniformly.
- Understanding the activity of Platinized B-UNCD toward oxygen reduction reaction.
- Fabrication of Pt/UNCD-diamond supported electrode and MEAs to evaluate performance and stability as a promising support to replace a commercial carbon support material.

The accomplishments can be summarized as follows:

- The insulating 500, 100 and 3-6 nm diam. diamond powders were coated with a thin layer of boron doped ultrananocrystalline diamond via CVD. It has been proved that the relatively high electrical conductivity after acid washing result from the doped diamond overlayer and not from any adventitious nondiamond carbon impurity phase. SEM images and Raman spectroscopy yielded further evidence in support of an ultrananocrystalline diamond overlayer. The surface area of the coated powders decreased approximately 30% due to particle-particle fusion during growth. Importantly, it was found that the doped diamond powder electrodes are dimensionally stable and corrosion-resistant during anodic polarization at 1.4 V vs. Ag/AgCl (1 h) in 0.5 M H₂SO₄ at 80 °C.
- Impregnation method was performed for platinum deposition on B-UNCD powder surface. The average size of Pt was 4 nm with a narrow size distribution. HRTEM and EELS measurements showed that the Pt nanoparticles attach directly on sp³ carbon sites

with no sp² carbon interfacial phase. The kinetic parameters for the oxygen-reduction reaction at Pt/B-UNCD-diamond powder are similar to those for clean polycrystalline Pt. The voltammetric features are all characteristic of polycrystalline Pt which indicates good electronic contact with B-UNCD powder and Pt particles. Electrochemical polarization results proved that B-UNCD powder has better corrosion resistance over commercial support material Vulcan XC-72. The catalytic effect of Pt on B-UNCD powder corrosion is significantly less than that on Vulcan XC-72. The increase of Pt particle size after anodic polarization for Pt/Vulcan XC-72 is much more than that for Pt/B-UNCD-diamond.

• For the first time the conductive diamond powder served as a support material in PEMFC. MEAs prepared by Vulcan XC-72 and B-UNCD-diamond support material were tested as single fuel cell and their stability was evaluated for 200-h by measuring OCP and ECSA. B-UNCD diamond powder shows significantly better stability compared to commercial sp² bonded Vulcan XC-72 support material. The performance of B-UNCD-diamond MEAs was comparable with commercial Vulcan MEA, which is a sign of good electrical contact of B-UNCD-diamond powder support at the triple region.

7.2 Future Research Directions

For the future study, the following works can be recommended for better understanding of B-UNCD powders performance as a fuel cell catalyst support material.

7.2.1 Preparation of B-UNCD-Diamond Powder

By CVD technique, relatively high surface area (170 m²/g) and electrically conducting (1 S/cm) diamond powder can be formed by overcoating inexpensive diamond with a layer of

boron-doped ultra-nanocrystalline diamond. In this coreshell approach, one must empirically determine the growth conditions needed to achieve maximum homogeneity in the overlayer while avoiding significant particle—particle fusion, which reduces the specific surface area. Our procedure for producing the electrically conducting diamond powder is not optimal yet. New reactor designs are required for more rapid, efficient, and homogeneous diamond coatings over individual seed particles. For instance, designs where the powders are suspended in or repeatedly get transported through the plasma would be ideal for achieving a more homogeneous coating.

7.2.2 Electroactivity of Pt/B-UNCD-Diamond Powder towards ORR

The platinization of B-UNCD-diamond powder was performed by impregnation method. These powders' structural properties, electrochemical activities and stabilities were characterized by several techniques. The voltammetric features are all characteristic of polycrystalline Pt which indicates good electronic contact with B-UNCD powder and Pt particles. The electrochemical characterization shows smaller ECSA for Pt/B-UNCD diamond powders compared to theoretical active surface area. As it is discussed, this might be due to nonhomogeneity in the Pt particle size and apparently due to larger Pt particles. Further work needs to be focused on to increase the electrical conductivity of diamond powder and catalyst dispersion procedure in order to reduce the particles size and improve the reactivity of this new type of diamond supported catalyst. By increasing the solvent volume for impregnation we may achieve to deposit smaller particles with better distribution. Heat treatment after solvent evaporation may also effect on the particle size. This experimental step also needs to be considered for smaller and more uniform Pt particle distribution. Composite electrodes made by mixing conducting diamond powder with flatter, more compressible powder such as hydrogenated graphite may help to reduce the electrode resistance while still maintaining a

significant portion of the corrosion resistance. Preliminary study shows that as the graphite weight ratio increase the conductivity of the composite electrode increase (Chapter 5.3). The corrosion resistance of these powders needs to be evaluated with and without Pt particles for further applications.

7.2.3 B-UNCD-Diamond Support for PEMFC

For the first time, B-UNCD-diamond material used as a support material for PEMFC and B-UNCD-diamond MEAs were tested and compared with commercial Vulcan XC-72 MEAs. Future work with B-UNCD-diamond powder MEA preparation and characterization should include following strategies to improve the performance of the MEAs.

- As it is mentioned above, preparation of the composite electrodes with B-UNCDdiamond and graphite may help us to increase the electrical conductivity and minimize the resistance in MEAs.
- The water management is a problem during our test conditions due to room temperature study. We believe that, the contact lost of the electrodes from the membrane is a result of water content at the cathode layer. We need to reconsider membrane thickness, gas diffusion, bipolar plates to keep the fuel cell operating efficiently.
- The most important limitation is the humidification problem in the fuel cell. We purged reactant gases through water at room temperature. This bubbling was not enough for fully humidification of the gases. We are in the process to improve the humidity of the gases by heating the water bathes for gas purging.
- Temperature is another factor that limits our current density. As the temperature increase, the catalytic activity of the Pt particles increases. We need to balance high temperature with correct humidification ratio to increase the performance of the fuel cells.

Impedance spectroscopy is a powerful characterization for electrical behavior of interfaces. The electrode performance in fuel cell is influenced many parameters such as Pt activity, water management, gas diffusion, gas ratio, gas purity, bipolar plates, membrane conductivity etc. Impedance spectroscopy is a very useful technique to study the different processes take place in the fuel cell. It also allows us to evaluate these parameters in a separate way to determine the influence of each on a fuel cell performance. For our study, to analyze ohmic resistance in the fuel cell, impedance spectroscopy should be performed. This characterization may give us better idea for the source of the ohmic resistance, capacitance and gas diffusion limitation and help us for our future development of the fuel cell materials.

7.2.4 Application of B-UNCD-Diamond Powder in the Next Generation Energy Devices

Ultra-nanocrystalline diamond powder has many different properties that pushed researchers in new directions, and its behavior in combination with other nanostructures will result in new classes of materials. A key characteristic of all UNCD is their purity. They have volume fractions of grain boundaries that amount to 10% of total growth by volume and consist of carbon in several different bonding states including sp² (graphitic). By tuning the growth process to change the grain size and to introduce select impurities (dopants like boron, nitrogen, etc.) to control the UNCD's electrical, thermal and morholohical properties we can have a wide variety of application area of these conductive high surface area B-UNCD powders.

The following works are recommended for B-UNCD-diamond powder in the next generation energy and power devices.

7.2.4.1 Hydrogen Storage

Hydrogen economy and fuel cell technology depends on the development of safe, reliable, cost-effective, and practical ways of storing hydrogen. By hydrogen spillover mechanism carbon materials can uptake hydrogen. Metalic nanoparticles should be deposited on carbon surface to facilitate hydrogen spillover on carbon materials. Therefore, the investigation of hydrogen storage for metal decorated carbon materials, especially B-UNCD powder must be an intriguing research subject. B-UNCD-diamond powder is chemically and thermally inert and might be good candidate for this research.

7.2.4.2 Lithium Batteries

In lithium batteries, the cycling behavior of the anode determines the cell life completely. Therefore, the anode materials are more important than the cathode materials in Li batteries. Carbon materials have been used either as the anode itself or as a conductive enhancer for the active materials mainly due to their high electrical conductivity and good corrosion resistance in many electrolytes. B-UNCD-diamond powder deposited with metal or metal oxide nanoparticles can be a solution to enhance charge discharge performance and cycling life for Li batteries.

7.2.4.3 Supercapacitors:

The double-layer capacitors and the redox capacitors are two types of the super capacitors. The double-layer capacitors stores charges within the interfacial double-layer of high specific area electrode in an aqueous or an organic electrolyte which is called the electrochemical double-layer capacitor (EDLC). Activated carbons with very high surface area of 1000~2000 m²/g have been widely used for the electrodes. In the redox capacitors, Faradaic redox reactions take place at the electrode surface consisting of electroactive materials. This is called as

pseudocapacitor which has been developed with transition metal oxide and conducting polymer. Since pseudocapacitor has a higher specific capacitance than EDLC. The electrode materials of pseudocapacitors are electroactive materials with redox state and structure such as transition-metal oxides (oxides of Ru, Co, Ir, Ni, Mg, In, Sn, Fe, etc). However, the high cost of ruthenium and iridium precursors has limited their practical usage. To reduce the cost of the material, the researchers have focused on developing of ruthenium oxides/carbon composites. Carbon nanotube, carbon black, activated carbon, and mesoporous carbon have been studied. Metal oxide/B-UNCD-diamond nanocomposites fabricated by the present method may be a good research subject for this application.